Università degli Studi di Torino
**Scuola di Dottorato**

---


# Chaotic dynamics in complex and active fluids

**Leonardo Puggioni**

Università degli Studi di Torino
**Scuola di Dottorato**

**Dottorato in Fisica**

# Chaotic dynamics in complex and active fluids

**Leonardo Puggioni**

**Tutor: Stefano Musacchio**

# Contents

# Introduction

This thesis is based on the work carried out during the three years of the doctoral cycle at Università di Torino, under the supervision of professor Stefano Musacchio. It is focused on the theoretical study, by means of extensive direct numerical simulations, of two different fluid systems, both of them characterized by a complex and chaotic behaviour at low Reynolds number. The two system are diluted rigid polymer solutions, described by the Doi-Edwards model, and dense bacterial suspensions, modelled with the Toner-Tu-Swift-Hohenberg (TTSH) equation. The first one is characterized by a chaotic flow similar to the elastic turbulence observed in flexible polymers, while the second one exhibits a regime called active turbulence, with peculiar patterns.

The structure of the thesis is the following:

- A short introduction to microhydrodynamics (Chapter 1), involving common concepts to the two system.

- The first part, composed by six chapters, regarding the dilute solutions of rigid rodlike polymers. Chapters 2, 3 and 4 constitute a summary of the current knowledge about this topic, in particular Chapter 2 describes the peculiar features of polymer solutions, Chapter 3 is centered on the rheological model we considered, and Chapter 4 describes the Kolmogorov flow, which is the particular configuration we adopted in our simulations. Chapters 5, 6 and 7 contain instead our original results. Chapter 5 involves our numerical investigation of the chaotic flow generated by the Doi-Edwards model at low Reynolds number, Chapter 6 includes our attempt to

study the linear stability of the Kolmogorov flow with rodlike polymers, and Chapter 7 describes how the turbulent (high-Reynolds) Kolmogorov flow is affected by polymers.

- The second part, composed by four chapters, on bacterial suspensions. Chapter 8 is a very short introduction to the active matter topic, and to active fluid models in particular. Chapter 9 is a summary of the previous literature about the TTSH model, with the derivation and a description of its phenomenology. Our original results are in Chapters 10 and 11. In particular Chapter 10 contains our investigation of the regime of flocking turbulence, while Chapter 11 describes how confinement induces the transition from flocking turbulence to an ordered state constituted by a giant vortex.
- The appendices, with the description of our numerical methods (Appendix A) and a short introduction to Brownian motion (Appendix B), which can help in the comprehension of the derivations of the models.

## List of publications

Part of the original work contained in this thesis has been published in the following journal articles:

1. Puggioni, Leonardo, Guido Boffetta, and Stefano Musacchio. "Enhancement of drag and mixing in a dilute solution of rodlike polymers at low Reynolds numbers." *Physical Review Fluids* 7.8 (2022): 083301.
2. L. Puggioni, G. Boffetta, and S. Musacchio. "Giant vortex dynamics in confined bacterial turbulence." *Physical Review E* 106.5 (2022): 055103.

In particular, Chapter 5 is based on publication 1, and most of the Chapter 11 on publication 2. A further article, containing Chapter 10 and the remaining of Chapter 11, has been just submitted. Chapters 6 and 7 are, for now, unpublished.

# Notations

## Geometric quantities

- $\boldsymbol{x}$: position
- $t$: time
- $r$: distance
- $r_a$: ellipsoid aspect ratio
- $a_0 = (r_a^2 - 1)/(r_a^2 + 1)$: Jeffery geometrical factor
- $\boldsymbol{n}$: ellipsoid director
- $\mathbf{I}$: identity tensor
- $\boldsymbol{k}$: wavevector
- $\Psi$: probability density function

## General hydrodynamics quantities.

- $\rho$: density field
- $\boldsymbol{u}$: fluid velocity field/coarse-grained bacterial velocity field
- $p$: pressure field
- $\nu$: kinematic viscosity
- $\mu$: dynamic viscosity
- $\boldsymbol{\omega} = \boldsymbol{\nabla} \times \boldsymbol{u}$: vorticity field

- $\boldsymbol{\kappa}$: velocity gradient tensor ($\kappa_{ij} = \partial_j u_i$)
- $\boldsymbol{\Sigma}$: strain-rate tensor ($\Sigma_{ij} = \frac{1}{2}(\kappa_{ij} + \kappa_{ji})$)
- $\boldsymbol{\Omega}$: rotation-rate tensor ($\Sigma_{ij} = \frac{1}{2}(\kappa_{ij} - \kappa_{ji})$)
- $\boldsymbol{\sigma}$: stress tensor/non-Newtonian stress tensor
- $\mathbf{F}, \boldsymbol{f}$: external forcing
- $\boldsymbol{R}$: polymer configuration tensor ($R_{ij} = \langle n_i n_j \rangle$)
- $\eta$: polymer feedback coefficient
- $Re$: Reynolds number
- $E(k)$: energy spectrum
- $k_B$: Boltzmann constant
- $T$: (absolute) temperature
- $D$: generic diffusion constant

## Kolmogorov flow quantities

- $K$: forcing wavenumber
- $F$: forcing amplitude
- $U$: mean flow amplitude
- $U_0 = F/(\nu K^2)$: laminar mean flow amplitude
- $\Pi_\nu$: $xy$ component of the Newtonian stress tensor
- $\Pi_r$: $xy$ component of the Reynolds stress tensor
- $\Pi_p$: $xy$ component of the polymer stress tensor
- $S$: Reynolds stress mean amplitude
- $\Sigma$: polymer stress mean amplitude
- $f = F/(KU^2)$: friction coefficient

- $s = S/U^2$: Reynolds stress coefficient
- $\sigma = \Sigma/U^2$: polymer stress coefficient
- $\varepsilon_I = \langle \boldsymbol{f} \cdot \boldsymbol{u} \rangle = FU/2$: mean energy input
- $\varepsilon_0 = FU_0/2$: laminar mean energy input
- $\varepsilon_\nu = \langle \nu |\boldsymbol{\nabla u}|^2 \rangle$: mean Newtonian dissipation rate
- $\varepsilon_p = \langle \sigma_{ij} \partial_j u_i \rangle$: mean polymer dissipation rate

## Bacterial turbulence quantities

- $\lambda_0$: self-advection coefficient
- $\alpha, \beta$: linear and cubic Landau forcing coefficients
- $\Gamma_0, \Gamma_2$: Swift-Hohenberg operator coefficients
- $\Lambda = 2\pi\sqrt{(2\Gamma_2)/\Gamma_0}$: vortex length scale
- $U = \sqrt{-\alpha/\beta}$: flocking velocity scale
- $R$: confinement radius

# Chapter 1

# Microhydrodynamics: a short summary

Both our numerical studies of rigid polymers solutions and bacterial suspensions rely on continuum models that, partially or totally, are obtained starting from a microscopical description. For this reason, it is better to start this dissertation with a brief introduction to microhydrodynamics.

The dynamics of a Newtonian, incompressible fluid, is described by the Navier-Stokes equation (NSE), [1] supplied with the null divergence condition:

$$\partial_t \boldsymbol{u} + \boldsymbol{u} \cdot \boldsymbol{\nabla} \boldsymbol{u} = -\boldsymbol{\nabla} p + \nu \nabla^2 \boldsymbol{u} + \boldsymbol{f}, \qquad \boldsymbol{\nabla} \cdot \boldsymbol{u} = 0. \tag{1.1}$$

Here, $\boldsymbol{u}$ is the velocity field, $p$ the (kinematic) pressure, $\nu$ the (kinematic) viscosity and $f$ a general external forcing, which can include a great variety of phenomena (mechanical forcing, buoyancy, non-inertial reference frame and other). Since we are considering an incompressible fluid with uniform density $\rho$, the latter does not appear in the equation.

The NSE corresponds to the momentum conservation equation for a fluid, and it can derived both with a microscopical approach and a macroscopic one. [2]

In the NSE different terms are therefore present, whose importance depends on the particular typology of flow we are considering. A common method adopted in fluid mechanics in order to understand which terms can be neglected, is to non-dimensionalise the NSE and obtain one (or more) non-dimensional quantity, whose value is an indication of relative importance of the various terms.

In our general case, a flow is characterized by length $L$ and velocity $U$ scales, that we can use to redefine spatial and temporal coordinates, and the velocity field:

$$\boldsymbol{x} = L\boldsymbol{x}'; \qquad t = (L/U)t'; \qquad \boldsymbol{u} = U\boldsymbol{u}'. \tag{1.2}$$

Substituting these quantities in the equation 1.1, we get:

$$\frac{UL}{\nu}\left(\partial_{t'} + \boldsymbol{u}' \cdot \boldsymbol{\nabla}'\right)\boldsymbol{u}' = -\boldsymbol{\nabla}' p' + \nabla'^2 \boldsymbol{u}' + \boldsymbol{f}'. \tag{1.3}$$

Neglecting for now the pressure (which in incompressible flow it is a function of velocity field) and the external forcing, we can observe that the ratio $UL/\nu$, called **Reynolds number** (from Osborne Reynolds), describes the the relative importance between the advection nonlinear term and the viscous linear one. Since we are interested in microscopic flows, we have $L \to 0$ by definition, and we can expect that also $U$ is very small. Therefore, in microscopic flows the left side of the equation 1.3 is basically zero, and the velocity field obeys to the **Stokes equation** [3] (SE) (now in the dimensional form):

$$\boldsymbol{\nabla} p = \nu \nabla^2 \boldsymbol{u} + \boldsymbol{f}, \qquad \boldsymbol{\nabla} \cdot \boldsymbol{u} = 0. \tag{1.4}$$

Differently from the NSE, the SE is a linear and time independent equation: it is therefore symmetric under time reversal. This symmetry, physically interpretable as absence of inertia, set a strong constraint on microswimming strategies, [4] as we will see in section 1.3.

## 1.1 Multipole expansion

We are interested in obtaining the velocity field $\boldsymbol{u}$ in presence of an immersed body, such as a rod-like polymer or a swimming bacterium. Linearity of equation 1.4 allows us to employ the same techniques adopted for similar equations in other branches of physics. More in particular, we can describe our velocity field in terms of a multipole expansion, similarly to the one adopted in electrostatics to describe the potential, since linearity of the equation implies that solutions obey to superposition principle. [3] This is a technique especially suitable if we are interested in the far-field flow caused by the body.

The starting point is to consider the equation 1.4 in an unbound domain, with a point-like forcing $\boldsymbol{f}(\boldsymbol{x}) = \delta(\boldsymbol{x}-\boldsymbol{x}')\boldsymbol{F}$, where $\delta(\boldsymbol{x})$ is the Dirac delta. The disturbance flow due to the forcing is obtained as:

$$\boldsymbol{u}(\boldsymbol{x}) = \int_V \boldsymbol{H}\left(\boldsymbol{x}-\boldsymbol{x}'\right)\cdot\boldsymbol{f}\left(\boldsymbol{x}'\right)d^3x'. \tag{1.5}$$

By definition $\boldsymbol{H}\left(\boldsymbol{r}\right)$ is therefore the Green's function of the Stokes equation, and it is called **Oseen tensor** (from Carl Wilhelm Oseen):

$$\boldsymbol{H}(\boldsymbol{r}) = \frac{1}{8\pi\nu}\left(\frac{\mathbf{I}}{r}+\frac{\boldsymbol{r}\boldsymbol{r}}{r^3}\right), \tag{1.6}$$

so the fundamental solution of SE is:

$$\boldsymbol{u}\left(\boldsymbol{x}\right) = \boldsymbol{H}\left(\boldsymbol{x}-\boldsymbol{x}'\right)\cdot\boldsymbol{F}. \tag{1.7}$$

The solution 1.7 is usually denoted as **Stokeslet**, although this term is sometimes used as synonymous of the Oseen tensor.

The Stokeslet is therefore the fundamental solution of the Stokes equation, other singular solutions can be obtained differentiating it. One order of differentiation gives us the *dipole* solution, while another one order the *quadrupole* solution. They constitute the terms of order one and two in the multipole expansion of the disturbance flow induced by an object immersed in the fluid (while the order zero term is obviously the Stokeslet). [5]

In particular, as we will see in 1.3, the dipole solution, corresponding to the situation with two point-like forcing, assumes great importance for us. It is useful to decompose it in its symmetric and antisymmetric parts.

In particular, the symmetric one is called **stresslet**:

$$u_i^{(S)}(\boldsymbol{x}) = \frac{1}{8\pi\nu}\left(\frac{x_i\delta_{jk}}{r^3} - \frac{x_i x_j x_k}{r^5}\right) S_{jk}; \tag{1.8}$$

while the antisymmetric one is called **rotlet**:

$$u_i^{(R)}(\boldsymbol{x}) = \frac{1}{8\pi\nu}\frac{\varepsilon_{ijk}L_j x_k}{r^3}; \tag{1.9}$$

where $S_{ij}$ and $L_i$ are the symmetric and the antisymmetric components of the force moment: stress and torque. The graphical representation of these velocity fields is shown in figure 1.1.

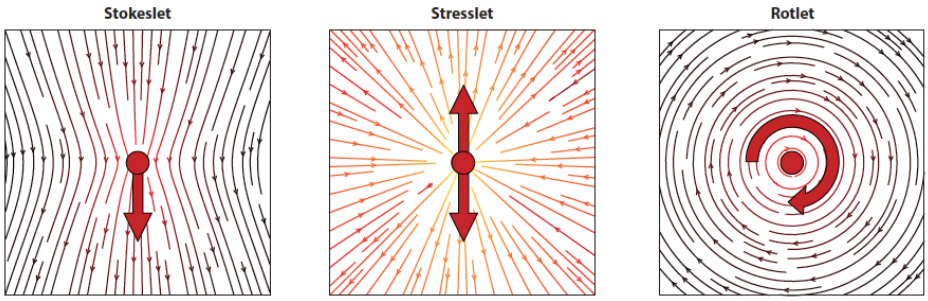


**Figure 1.1:** Elementary solutions, of order 0 and 1, of the Stokes equation. *Image took from* [5].

We can note that the singular solution of order $n$ decays with distance $r$ as $1/r^{n+1}$: for this reason high-order solutions are usually negligible.

## 1.2 Solid body motion and Jeffery equation

Multipole expansion with superposition of singular flows (stokeslets, stresslets etc.) is not the only strategy to deal with the Stokes equation, in particular if we are considering a solid body immersed in the fluid. One starting assumption is, since we are considering a vanishing Reynolds number, to neglect the inertia of the object. This is a reasonable assumption in microfluidics, [6] which allows us also to make an

important assumption on the flow: if we consider a sufficient small spatial scale, every flow can be approximated with its Taylor series, and so we can consider a linear velocity field without loss of generality:

$$\boldsymbol{u} = \boldsymbol{U}^{\infty} + \boldsymbol{\kappa} \cdot \boldsymbol{x}; \tag{1.10}$$

where $\boldsymbol{U}^{\infty}$ is a constant mean flow and $\boldsymbol{\kappa}$ is the rank-2 velocity gradient tensor: $\kappa_{ij} = \partial_j u_i$, which can be decomposed into its symmetric (strain-rate tensor) and antisymmetric (rotation-rate tensor) part:

$$\Sigma_{ij} = \frac{1}{2}\left(\kappa_{ij} + \kappa_{ji}\right), \tag{1.11}$$

$$\Omega_{ij} = \frac{1}{2}\left(\kappa_{ij} - \kappa_{ji}\right). \tag{1.12}$$

Since the equation (1.4) is linear, we expect a linear relationship between forces and torques acting on the body, and the resulting velocity and vorticity fields. The simplest case, a sphere with no-slip surface, was considered by Stokes himself. [7] It can be shown that the viscous drag force $\mathbf{F}$ exerted by the fluid on a spherical particle, with radius $r$, moving with velocity $\boldsymbol{u}$ with respect to the fluid is: [8]

$$\mathbf{F} = 6\pi\mu r\boldsymbol{u}. \tag{1.13}$$

The quantity $\zeta = 6\pi\mu r$ is called friction coefficient, inverting the relationship we have the mobility coefficient $\zeta^{-1}$. In the case of anisotropic shape, we have a more complex connection, but still linear (where $\mathbf{N}$ is the torque): [3]

$$\begin{pmatrix} \mathbf{F} \\ \mathbf{N} \end{pmatrix} = \begin{pmatrix} \mathbf{A} & \mathbf{B} \\ \mathbf{B}^T & \mathbf{C} \end{pmatrix} \cdot \begin{pmatrix} \boldsymbol{u} \\ \boldsymbol{\Omega} \end{pmatrix}, \tag{1.14}$$

or its inverse:

$$\begin{pmatrix} \boldsymbol{u} \\ \boldsymbol{\Omega} \end{pmatrix} = \begin{pmatrix} \mathbf{a} & \mathbf{b} \\ \mathbf{b}^T & \mathbf{c} \end{pmatrix} \cdot \begin{pmatrix} \mathbf{F} \\ \mathbf{N} \end{pmatrix}, \tag{1.15}$$

where the quantities $\mathbf{A}$, $\mathbf{B}$, $\mathbf{C}$... are second-order tensors. The exact computation of these quantities is possible only for a regular and symmetric shape.

For this reason, both for rigid elongated polymers and bacilliform bacteria it is convenient to consider an axis-symmetric ellipsoidal shape. In

this case, if we define a versor $\boldsymbol{n}$ which denotes the orientation the ellipsoid axis, it was demonstrated in 1922 by George Jeffery [9] that, under a linear flow, its dynamics is described by the following equation (assuming also buoyancy neutrality):

$$\dot{\boldsymbol{n}} = \boldsymbol{\Omega} \cdot \boldsymbol{n} + a_0 \left[ \boldsymbol{\Sigma} \cdot \boldsymbol{n} - \boldsymbol{n} \left( \boldsymbol{n} \cdot \boldsymbol{\Sigma} \cdot \boldsymbol{n} \right) \right]; \tag{1.16}$$

where $a_0$ is a geometrical factor dependent on the ellipsoid aspect ratio $r_a$:

$$a_0 = \frac{r_a^2 - 1}{r_a^2 + 1}. \tag{1.17}$$

Jeffery equation is currently adopted as the standard description of non-inertial anisotropic particles in fluid flows. [6] The last term in the equation 1.16 assures non-extensibility, maintaining $\|\boldsymbol{n}\|^2 = 1$:

$$\frac{1}{2}\partial_t \left( \boldsymbol{n} \cdot \boldsymbol{n} \right) = \boldsymbol{n} \cdot \boldsymbol{\Omega} \cdot \boldsymbol{n} + a_0 \left[ \boldsymbol{n} \cdot \boldsymbol{\Sigma} \cdot \boldsymbol{n} - \boldsymbol{n} \cdot \boldsymbol{n} \left( \boldsymbol{n} \cdot \boldsymbol{\Sigma} \cdot \boldsymbol{n} \right) \right]. \tag{1.18}$$

Since $\boldsymbol{n} \cdot \boldsymbol{\Omega} \cdot \boldsymbol{n} = n_i n_j \Omega_{ij} = 0$, being the product of a symmetric tensor with an antisymmetric tensor, we have:

$$\frac{1}{2}\partial_t \left( \boldsymbol{n} \cdot \boldsymbol{n} \right) = a_0 \left( 1 - \boldsymbol{n} \cdot \boldsymbol{n} \right) \left( \boldsymbol{n} \cdot \boldsymbol{\Sigma} \cdot \boldsymbol{n} \right), \tag{1.19}$$

which implies that, if $\boldsymbol{n} \cdot \boldsymbol{n} = \|\boldsymbol{n}\|^2 = 1$ at $t = 0$, we will have $\|\boldsymbol{n}\|^2 = 1 \quad \forall t > 0$.

## 1.3 Swimming at low-Reynolds

We can define a swimmer as a body which deforms its surface in order to obtain a net displacement, without relying on external factors. While some microorganisms deform all their body in order to sustain movement (for example amoebae), in many others, like rod-shaped bacteria, spermatozoa or micro-algae, the deformation occurs only in specific motile appendages like cilia or flagella. [10]

Swimming in a low-Reynolds regime is characterized by some peculiar properties. Absence of inertia implies a balance of forces and torques, between the viscous and the external ones. Usually microorganisms are force- and torque-free swimmers (in the sense that they are not subjected

to external forces or torques), although there are exceptions (for example nonneutrally buoyant cells for the case of non-zero force, or gravitactic/magnetotactic organisms subjected to an external torque). [5]

Other important properties derive from the temporal symmetry of equation (1.4). One is rate independence: the distance travelled by the swimmer deforming its surface does not depend on the rate at which the deformation occurs, but only on its geometry. Strictly related is the so-called scallop theorem (enunciated by Purcell in 1977 [11]): if the swimmer modifies its surface in a time-symmetric sequence of deformations, it can not achieve a net displacement. The theorem takes its name from the typical behaviour of a scallop (see figure 1.2), which opens and closes periodically its shell (a real scallop can actually swim since its dimensions and its rate of deformation are such as to obtain an high Reynolds-number flow). The microorganism therefore must deform its body in a non-reciprocal way, which requires at least two degrees of freedom (while a scallop has only one), in the case of bacteria this is usually achieved with rotating helical flagella. [4] Since the time reversibility is not assured in a non-Newtonian fluid, in this case a net displacement with a reciprocal deformation can be actually obtained. [12]

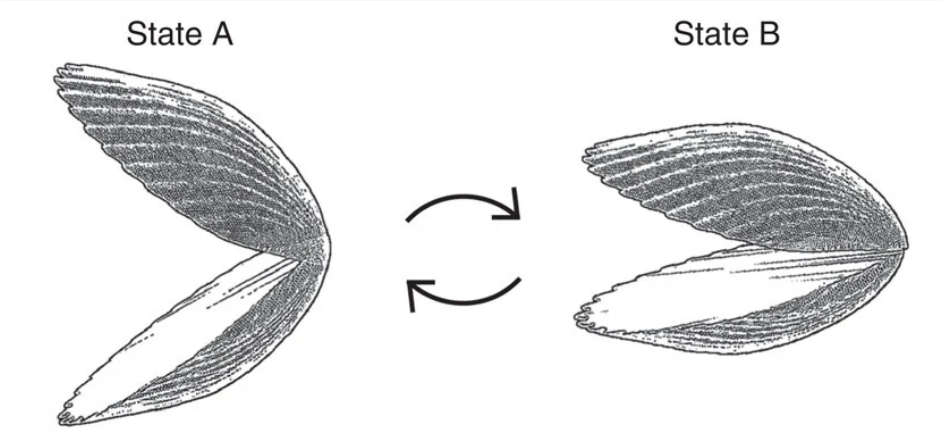


**Figure 1.2:** Reciprocal deformation of a scallop. *Image adapted from* [12].

The precise way a microswimmer deforms its body to obtain a net motion, and the detailed velocity field around its surface, is a current

research field, but is far beyond the scope of this chapter. We are interested in the far-field disturbance flow generated by the swimmer, which at this level of approximation can be expressed in terms of the multipole expansion. Since microswimmers are usually force- and torque-free, the lowest order singularity is the stresslet, associated to a symmetric force dipole, which, if the swimmer is axisymmetric with director $\boldsymbol{n}$, can be expressed as $\boldsymbol{S} = \sigma_0 \boldsymbol{nn}$. The sign of the coefficient $\sigma_0$ depends on the propulsion, in particular on the relative point of application of the net thrust exerted by flagella on the fluid and the viscous drag exerted by the fluid on the cell body: extensile swimmers, denoted **pushers**, have $\sigma_0 < 0$, while contractile ones have $\sigma_0 > 0$ and they are denoted **pullers**. Examples of pusher are bacteria and spermatozoa (which have flagella on the back of their body), while microalgae have typically their flagella on the front of their body, and therefore they are pullers. While experimental studies with *Escherichia coli* have shown that the force dipole is a good approximation for the flow generated by bacteria, [13] measurements on *Chlamydomonas reinhardtii* pointed out that the time averaged flow is better described by a three off-centered point forces, [14] two on the flagella and one on the body (see figure 1.3).


**Figure 1.3:** Difference between the disturbance flow generated by a bacteria (*Escherichia coli*) and by an alga (*Chlamydomonas reinhardtii*). *Image took from* [5].

We therefore expect a microswimmer suspension to have a modified rheology from the fluid without swimmers, due to the averaged disturbance flow. If the concentration is not too high (otherwise more complex behaviours happen) we expect an enhanced effective viscosity in the case of pullers, and a reduced effective viscosity for pusher, due to the fact that the disturbance flow in the former case opposes to external shear, while in the latter case the the external shear is reinforced. This prediction has been experimental verified, also comparing with the passive case of dead

cells, [15] both for bacteria [16] and algae. [17]

Finally, it is worth to mention that bacteria, especially in the presence of chemical gradients, exhibit a particular form of random motion called run-and-tumble behaviour: they swim straightly for a certain amount of time (which can vary from one to hundreds of seconds, depending both on environmental conditions and strain of bacteria), and then they abruptly change direction. [18] This is a separated, although somewhat similar, phenomenon with respect to the Brownian motion due to thermal noise of the fluid. [5]

# Part I

# Dilute solutions of rigid polymers

# Chapter 2

# General properties of polymer solutions

Polymer solutions are an example of complex fluid, which is a generic class of systems with different behaviours. In particular, complex fluids are usually characterized by a non-Newtonian rheology, which means that the stress tensor is not simply a linear function of the shear rate as in a Newtonian fluid, where (in the incompressible case) $\boldsymbol{\sigma} = \mu \left[ \boldsymbol{\nabla u} + (\boldsymbol{\nabla u})^T \right]$. Clearly, the non-Newtonian behaviour can take many different forms, which can be grouped in some categories: [19]

- viscoelasticity: the stress tensor depends both on the shear rate and on the deformation (the fluid has a memory);
- shear thinning/thickening: the viscosity depends on the shear rate, *i.e.* the stress tensor is a nonlinear function of the shear rate;
- normal stress effects: in shear flows, in addiction to shear stresses, there also an extra tension along the streamlines; [20]
- extensional thinning/thickening: in extensional flows the viscosity depends on the flow strength, or it is different from the Newtonian prevision with respect to shear viscosity ($\mu_E = 3\mu$).

Obviously these phenomena can be further divided into various subcategories (for example, we can have linear o nonlinear viscoelasticity)

and combinations. These peculiar rheological properties bring to peculiar fluid mechanics phenomenon, that we can not observe in Newtonian fluids.

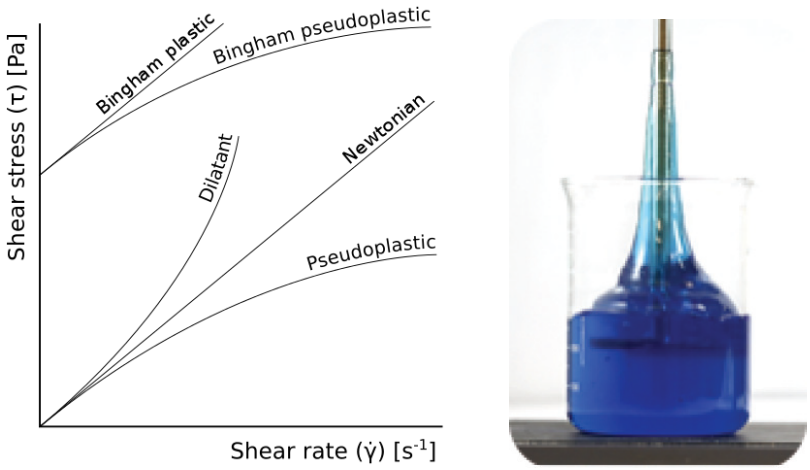


**Figure 2.1:** Left: example of possible functions of the shear stress in terms of the shear rate. Right: Weissenberg effect, the fluid climbs a rotating rod inside it, contrary to the way a Newtonian fluid would do. This phenomenon is due to normal stress effects. [19]

Among all the complex fluids we can list (blood, milk, mucus, mayonnaise, ink, gels and colloids, and many others), dilute polymer solutions are of interest in the fluid mechanics community since even minute concentrations of polymers can dramatically change the properties of turbulent flows, or alter the stability of laminar flows. In the rheological context we have two fundamental (idealised) paradigms: flexible and rigid polymers. In the first one, polymer molecules are described as elastic strings which interact with the fluid being stretched by the flow, and therefore storing and releasing elastic energy. In the second one, the molecules are modelled as small, thin and non-deformable rods, which are in rotational equilibrium with the fluid velocity field, affecting the flow trough skin friction effects. [21] Real polymers partly have both the properties, but usually one of them is prevalent on the other. Typically, in literature, "polymers" without other specifications means "elastic polymers", [22] but many of these peculiar phenomenon can be obtained also with rigid polymers.

To perform numerical simulations of polymer solutions, several rheological models have been proposed. The simplest ones are the Oldroyd-B model (and the strictly related FENE-P model, taking in account the finite extensibility of molecules) for flexible polymers, [23] and the Doi-Edwards [24] model for rigid rod-like polymers. The stress tensor is very different between the two cases, but the general approach is the same: the polymer configuration is described by a rank-2 tensor $\boldsymbol{R}$, which is advected by the velocity field $\boldsymbol{u}$ and convected by its gradient $\boldsymbol{\nabla u}$. The velocity fluid field is in turn influenced by the polymer configuration, since in the Navier-Stokes equation there is a non-Newtonian stress tensor depending on $\boldsymbol{R}$. To be more explicit, here it is the Oldroyd-B model for dilute flexible polymers solutions:

$$\partial_t \boldsymbol{u} + (\boldsymbol{u} \cdot \boldsymbol{\nabla})\, \boldsymbol{u} = -\boldsymbol{\nabla} p + \nu \nabla^2 \boldsymbol{u} + \frac{2\eta\nu}{\tau} \boldsymbol{\nabla} \cdot \boldsymbol{R} + \boldsymbol{f}, \tag{2.1a}$$

$$\partial_t \boldsymbol{R} + (\boldsymbol{u} \cdot \boldsymbol{\nabla})\, \boldsymbol{R} = (\boldsymbol{\nabla u})^T \cdot \boldsymbol{R} + \boldsymbol{R} \cdot (\boldsymbol{\nabla u}) - 2\frac{\boldsymbol{R} - \mathbf{I}}{\tau}, \tag{2.1b}$$

where $\eta$ is a parameter proportional to polymer concentration and $\tau$ is the polymer relaxation time. In this case, the non-Newtonian stress is elastic and linear, in the Doi-Edwards model is instead viscous (proportional to $\boldsymbol{\nabla u}$) and quadratic in $\boldsymbol{R}$. Another difference is in the equation describing the evolution of $\boldsymbol{R}$: in the flexible case, we have a relaxational term, while for rigid polymers we have a term ensuring the conservation of the trace of $\boldsymbol{R}$ (due to inextensibility of rigid polymers)..

Using these simple rheological models, it is possible to reproduce non-trivial phenomena observed in experiments. In particular, the most significant ones are the polymer drag reduction at high-Reynolds number, [25] and the elastic turbulence at low-Reynolds, [26], along other related phenomena like viscoelastic instabilities, elasto-inertial turbulence and modified heat transfer in natural convection. [22]

## 2.1 Polymer drag reduction

An important feature of high-Reynolds flows is that a large amount of kinetic energy is dissipated by an hydrodynamic drag due to turbulence,

much larger than the amount that would be dissipated if the flow was laminar. This behaviour can be parametrized by the drag coefficient, or friction factor, which, in the case of a pipe with diameter $R$, across a length $L$ with a pressure drop $\Delta p$, having fluid density $\rho$ and mean velocity $U$, is defined as: [27]

$$f = \frac{\Delta p}{\rho U^2} \frac{R}{L}, \tag{2.2}$$

which is proportional to $1/Re$ in laminar flows, while it reaches an asymptotic constant value for $Re \to \infty$ in turbulent flows. Reducing the turbulent drag, in order to obtain the same flow with a reduced forcing, is therefore of great practical importance in many industrial processes.

In order to reduce the drag, many strategies can be employed, one is to add polymer molecules in the fluid: it was indeed discovered, already in 1949, [28] that even a minute amount of flexible polymers can strongly reduce the turbulent drag. The most famous practical application of polymer drag reduction is in the Trans-Alaska Pipeline system and in other petroleum pipelines, where this phenomenon helps to reduce the energy consumption of oil transport. [29]

Even now we do not have a complete theory explaining flexible polymer drag reduction, [30] since the mechanism by which the viscoelasticity affects a turbulent flow, if generating a large effective extensional viscosity (Lumley's theory [31]), or creating an elastic stress comparable to the Reynolds one (De Gennes' theory [32]), is not clear. This scenario is further complicated by the fact that also solutions of polymers having a negligible flexibility give rise to drag reduction, [21] although usually an higher concentration is needed, [33] but both the theories of Lumley and De Gennes cannot be applied in the case of rigid polymers.

Drag reductions by flexible and rigid polymers show some similarities, but also differences. Considering wall-bounded flows, the effect of polymers increases with the concentration, but it exists an asymptotic state, called maximum drag reduction (MDR), that cannot be exceeded. [22] In the MDR we have a logarithmic relationship between the normalized distance from the wall $y^+$ and the normalized mean velocity $V^+(y^+)$, [34]

similar (but obviously with different coefficients) to von-Karman log-law in Newtonian turbulent flows:

$$V^+\left(y^+\right) = \frac{1}{\kappa_{\mathrm{V}}} \ln y^+ + B_{\mathrm{V}}. \tag{2.3}$$

This asymptotic law appears to be universal between flexible and rigid polymer solutions, but the crossover at increasing concentration, between the von-Karman law and the MDR law appears to be very dependent on the typology of the solution. [21, 35] In particular, for flexible polymers, at large values of $Re$ the mean velocity profile follows the MDR until a certain crossover point, beyond which it becomes parallel to von-Karman law, and increasing the concentration corresponds to push the crossover point towards larger values of $y^+$. Instead, for rigid polymers, the velocity profile is a sort of "interpolation" between the two logarithmic laws, saturating to the MDR only at large concentrations (fig. 2.2).

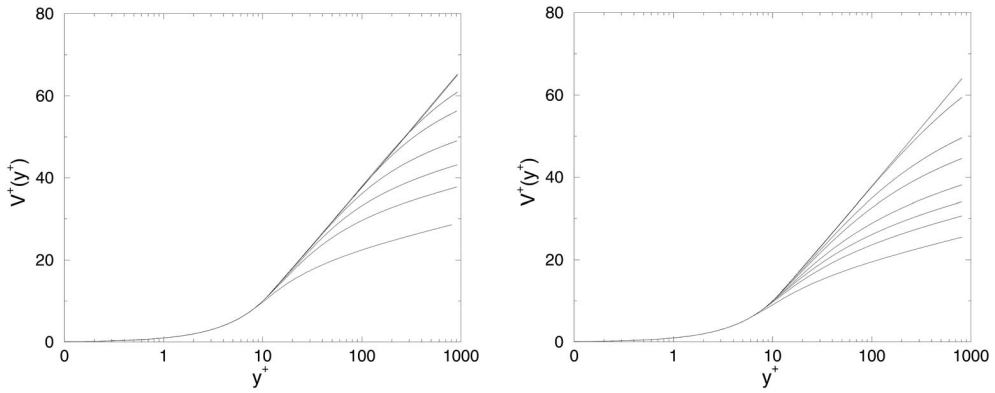


**Figure 2.2:** Mean velocity profiles of turbulent channel flows with different concentrations of polymer additives, in normalized units, compared with the asymptotic MDR curve, in the case of flexible (left) and rigid (right) polymers. [21] We can observe that in the first case, the curves follow the MDR asymptote until a certain crossover point, before to assume a "von-Karman-like" profile, while in the second one the curves never follow the MDR and the von-Karman laws, assuming an intermediate profile.

Another important difference between the two categories of additives is at moderate Reynolds number (but not so moderate to have laminar flow): rod-like polymers cause a drag enhancement, while for flexible polymers the drag remains the same of the Newtonian case. [36] In channel flows, a phenomenological theory explaining the common MDR asymp-

tote for flexible and rigid polymers was proposed, in terms of an effective viscosity, dependent on the distance from the walls. [37–39] The theory has been verified with direct numerical simulations of the FENE-P and Doi-Edwards model, [40, 41] and it explains also the different behaviour at moderate Reynolds: rodlike polymers generate an effective uniform viscosity (larger than the Newtonian one), while flexible ones, being coiled for moderate shear, do not alter significantly the rheology of the fluid. [36] But this remains a phenomenological theory limited to wall-bounded flows, and the relationship between drag reduction by flexible and rigid polymers remains an active research area, both experimentally and numerically. [30, 33, 42–45] Moreover, while the effect of flexible polymers on turbulence has been numerically investigated also in other typologies of flows, for example in a shear flow without walls, [46] in homogenous isotropic turbulence [47–49] or in natural convection, [50, 51] a comparable study of the effect of rigid polymers in turbulent flows is still missing.

## 2.2 Elastic turbulence

The elastic turbulence can be considered as the diametrically opposite phenomenon to drag reduction. Although the fact the viscoelastic stresses can trigger instabilities in laminar flows was already known, [52–54] in 2000-2001 a new phenomenon was discovered in flexible polymer solutions: a chaotic flow at low Reynolds numbers, showing several similarities with inertial turbulence at high Reynolds. [55–57] In particular it was observed a large increase in the hydrodynamic drag, a broad range of active spatial (and temporal) scales (corresponding to a power-law energy spectrum) and a massive increase of mixing rate, compared to a similar Newtonian flow at the same Reynolds number. [26] For this reason, this regime was called "elastic turbulence", although we can observe also several important differences with the "real" fluid turbulence, for example the absence of the energy cascade. More in general, in this regime inertial effects are (usually) negligible.

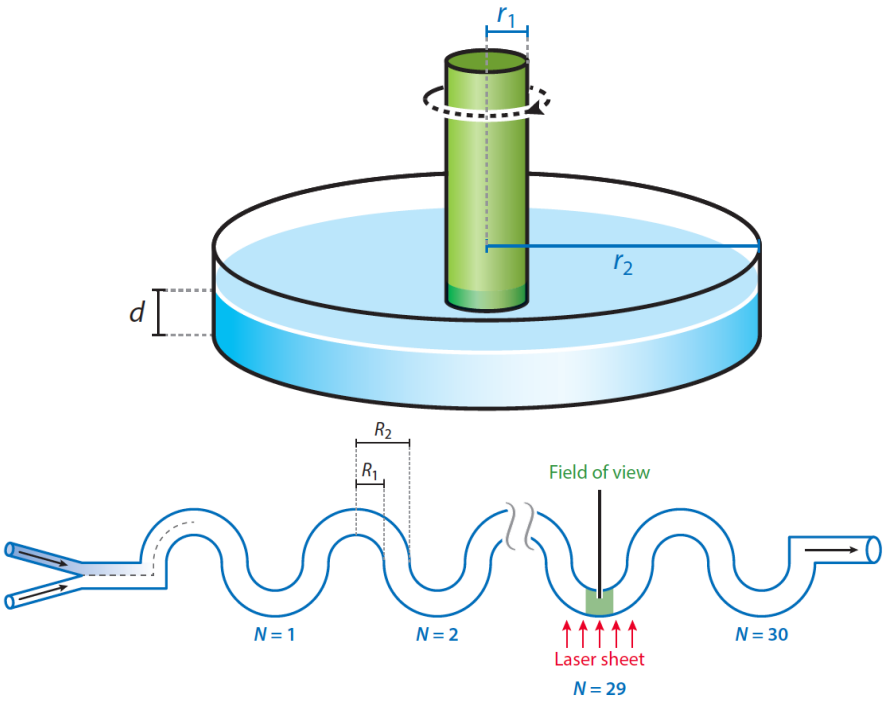


**Figure 2.3:** Sketches of the experimental apparatus used to firstly observe elastic turbulence: Taylor-Coutte [55] (top) and curvilinear channel [56] (bottom).

After the original experimental observations in Taylor-Couette [55] (fluid confined between two parallel rotating disks) and curvilinear channel [56] configurations (fig. 2.3), numerical simulations of the Oldroyd-B and FENE-P models in unbounded domains, [58, 59] wall bounded channel flows with a periodic array of obstacles, [60] or in Taylor-Coutte flows [61,62] predicted the emergence of a chaotic flows, which can be reproduced also with a low-dimensional shell model. [63] Some theoretical predictions have been also formulated starting from the Oldroyd-B model and assuming an uniaxial stress tensor $\sigma_{ij} = B_i B_j$: in this case, the set of hydrodynamical equations assumes a form similar to the one of the magnetohydrodynamics (MHD) approximation in plasma physics, with $B_i$ having a role similar to the one of the magnetic field. [64] Predictions of this theory and results from numerical simulations are usually compatible with the elastic turbulence observed in experiments, although in some cases there are quantitative discrepancies (for example, in the relative

weight of elastic and viscous stresses), which have been attributed to inaccurate approximations, over-simplified models or the effect of walls. [26]

The similarity with MHD equations predicts also the existence of elastic waves, analogous to the Alfvén waves in plasmas. [65] Their existence in the transition to elastic turbulence was later supported by numerical simulations of the Oldroyd-B model in a boundaries-free domain, [66] and it was finally confirmed in a recent experiment with a channel flow. [67]

Another regime was discovered in 2013, the elasto-inertial turbulence. [68] In this case, the inertial effects are important, and the flow remains qualitatively distinct from both the elastic turbulence and the drag reduction. The relationship of this phenomenon with the other two regimes is still an open question. [69]

Although all the experiments about elastic turbulence (until now) involve flexible polymers, and also the proposed theoretical explanations rely on the elasticity of polymers, recent two-dimensional numerical simulations, in periodic domains, of rod-like polymers with the Doi-Edwards model, predicted the emergence of a chaotic flow. [70, 71] This regime appears to be qualitatively similar the one simulated with the Oldroyd-B model, but with some quantitative differences: for example, while for the flexible polymers we have a power-law spectrum with an exponent comprised between $-3$ and $-4$, in the case of rigid polymers an exponent between $-4$ and $-5$ is predicted. A further investigation of this regime, both in two- and three- dimensional domains will be the subject of chapter 5.

# Chapter 3

# The Doi-Edwards model

The model which describes the behaviour of a dilute solution of rod-like polymers is the one developed by M. Doi and S.F. Edwards, [24] partially based also on results about rheological behaviour of suspensions of ellipsoidal particles by H. Brenner [72] and by E. J. Linch and L. G. Leal. [73, 74]

This model considers the case of non-deformable and extremely thin molecules, which therefore can only rotate and translate. The suspension is assumed to be dilute (average distance between polymers much larger than the length of a single polymer), hence every rod can rotate freely without interference by other polymers, and uniform: the rods are homogeneously distributed in the solvent fluid.

### 3.0.1 Rotational motion

The idea from Doi and Edwards was to consider macromolecules as an ensemble of Brownian beads, subjected to bounds, following previous works by Kirkwood. [75] In particular, for rigid elongated polymers they considered the "shish-kebab" model, which means that the elongated rod, with length $L$ and diameter $b$, is approximated as an ensemble of $N = L/b$ aligned spherical beads (see Fig. 3.1). This fact implies that, if the center of the rod is located at position $\boldsymbol{x}$, the $a$-th bead (with $-N/2 < a < N/2$) it will be located at $\boldsymbol{x}_a = \boldsymbol{x} + ab\boldsymbol{n}$, where $\boldsymbol{n}$ is the unit vector denoting the rod orientation. Similarly, if $\mathbf{v}$ is the center of mass velocity, and $\mathbf{w}$

the polymer angular velocity, the bead will move as:

$$\mathbf{v}_a = \mathbf{v} + \mathbf{w} \times ab\boldsymbol{n}. \tag{3.1}$$

If the rod is very thin (we will consider the case with aspect ratio $r_a \to \infty$), we can neglect the rotation around $\boldsymbol{n}$, and so, if we suppose that it is subjected to an external torque $\mathbf{N}$, both $\mathbf{N}$ and $\mathbf{w}$ are perpendicular to $\boldsymbol{n}$. With small $\mathbf{N}$, we can assume linearity and parallelism between $\mathbf{w}$ and $\mathbf{N}$:

$$\mathbf{w} = \frac{1}{\zeta_r}\mathbf{N}, \tag{3.2}$$

where $\zeta_r$ is the rotational friction coefficient.

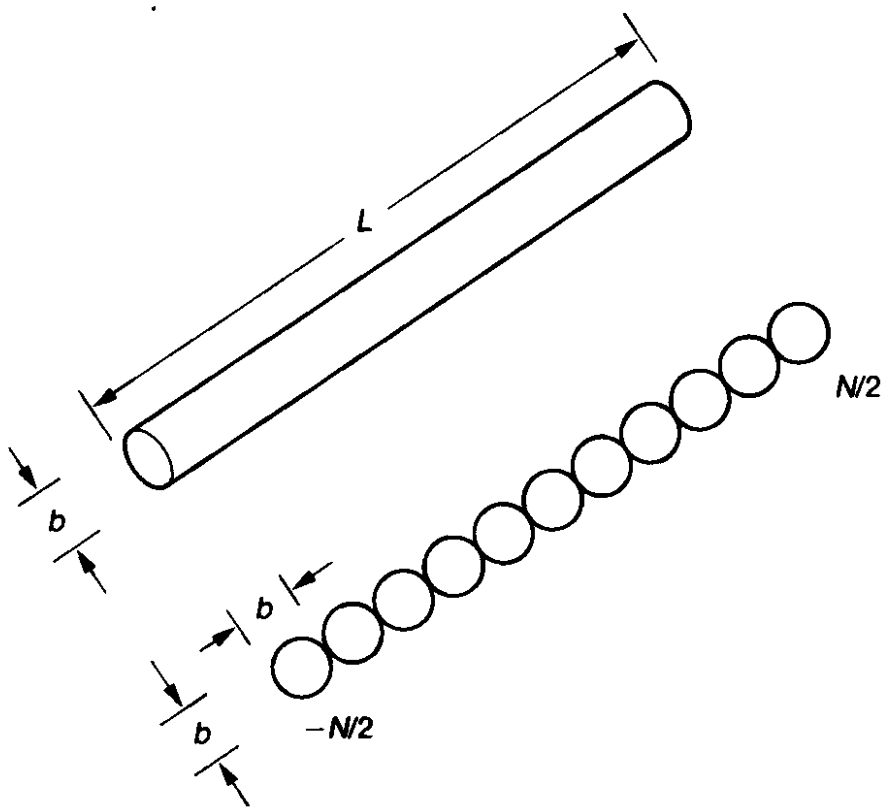


**Figure 3.1:** "Shish kebab" model for elongated rigid polymers. [24]

The coefficient $\zeta_r$ can be computed using the shish kebab model. The idea is to express the velocity of every bead in terms of the mobility tensor, which takes in account the hydrodynamic interactions between

the beads, and therefore to sum on over them, in order to obtain the total force and torque acting on the rod. It can be shown that we have:

$$\zeta_r = \frac{\pi \mu L^3}{3 \ln (L/2b)}. \tag{3.3}$$

We can express the external torque in terms of a potential $U$: defining the rotational operator $\mathcal{R}$ as:

$$\mathcal{R} = \boldsymbol{n} \times \frac{\partial}{\partial \boldsymbol{n}}, \tag{3.4}$$

we have $\mathbf{N} = -\mathcal{R}U$.

In our case, we can assume that the only potential to which the rods are subjected, is the thermodynamic one due to Brownian motion $U = k_B T \ln \Psi$, where $\Psi(\boldsymbol{x}, \boldsymbol{n}, t)$ is the probability density function of the rods (see also Appendix B).

Now, we have to take in account the effect of the velocity field of the solvent fluid. Since we are in the Stokes regime, and since the fact that a very thin rods can be seen as an extremely elongated prolate ellipsoid, the orientation will obey to the Jeffery equation (with $a_0 = 1$):

$$\dot{\boldsymbol{n}} = \boldsymbol{\kappa} \cdot \boldsymbol{n} - (\boldsymbol{n}\boldsymbol{n} : \boldsymbol{\kappa})\, \boldsymbol{n}. \tag{3.5}$$

The angular velocity due to the flow is therefore $\mathbf{w}_0 = \boldsymbol{n} \times \dot{\boldsymbol{n}} = \boldsymbol{n} \times (\boldsymbol{\kappa} \cdot \boldsymbol{n})$. Putting together hydrodynamics and Brownian contributions, we have:

$$\mathbf{w} = -\frac{1}{\zeta_r} \mathcal{R} \left( k_B T \ln \Psi \right) + \boldsymbol{n} \times (\boldsymbol{\kappa} \cdot \boldsymbol{n}). \tag{3.6}$$

The Smoluchowski equation for the rotational motion will therefore have the form:

$$\frac{\partial \Psi}{\partial t} = -\mathcal{R} (\mathbf{w} \Psi) = \mathcal{R} \left( D_r \mathcal{R} \Psi - \boldsymbol{n} \times (\boldsymbol{\kappa} \cdot \boldsymbol{n}) \Psi \right), \tag{3.7}$$

where $D_r = k_B T / \zeta_r$ is the rotational diffusion constant.

### 3.0.2 Translational motion

Now we consider the translational motion. If the rod is moving with velocity $\mathbf{v}$, it will be subjected an hydrodynamic drag $\mathbf{F}$, dependent on

$\mathbf{v}$. But, since the rod is anisotropic, the relationship between $\mathbf{F}$ and $\mathbf{v}$ is a function of the angle between $\boldsymbol{n}$ and $\mathbf{v}$, since the fluid will exert more resistance if the rod is transverse with respect the motion. It is therefore convenient to decompose the velocity in the components parallel and perpendicular to $\boldsymbol{n}$, $\mathbf{v} = \mathbf{v}_\parallel + \mathbf{v}_\perp$, in order to express the drag as:

$$\mathbf{F} = \zeta_\parallel \mathbf{v}_\parallel + \zeta_\perp \mathbf{v}_\perp. \tag{3.8}$$

$\zeta_\parallel$ and $\zeta_\perp$ can be obtained applying the Kirkwood theory at the shish-kebab model similarly to $\zeta_r$, and their value is:

$$\zeta_\parallel = \frac{2\pi\mu L}{\ln(L/b)}, \qquad \zeta_\perp = 2\zeta_\parallel. \tag{3.9}$$

Since we can formulate the velocities as $\mathbf{v}_\parallel = (\mathbf{v}\cdot\boldsymbol{n})\,\boldsymbol{n}$ and $\mathbf{v}_\perp = \mathbf{v} - \mathbf{v}_\parallel$, we can obtain an expression of drag in terms of the orientation versor $\boldsymbol{n}$:

$$\mathbf{F} = \zeta_\parallel \boldsymbol{nn}\cdot\mathbf{v} + \zeta_\perp(\mathbf{I} - \boldsymbol{nn}). \tag{3.10}$$

This last relationship can be inverted in order to express $\mathbf{v}$ in terms of $\mathbf{F}$:

$$\mathbf{v} = \left[\frac{1}{\zeta_\parallel}\boldsymbol{nn} + \frac{1}{\zeta_\perp}(\mathbf{I} - \boldsymbol{nn})\right]\cdot\mathbf{F}, \tag{3.11}$$

and, finally, we can also add the motion due to the fluid flow:

$$\mathbf{v} = \left[\frac{1}{\zeta_\parallel}\boldsymbol{nn} + \frac{1}{\zeta_\perp}(\mathbf{I} - \boldsymbol{nn})\right]\cdot\mathbf{F} + \boldsymbol{\kappa}\cdot\boldsymbol{x}. \tag{3.12}$$

If we assume that the only forcing to which the rod is subjected is the one due the Brownian motion, we can express $\mathbf{v}$ in terms of the thermodynamic potential $\Psi$:

$$\mathbf{v} = \left[\frac{1}{\zeta_\parallel}\boldsymbol{nn} + \frac{1}{\zeta_\perp}(\mathbf{I} - \boldsymbol{nn})\right]\cdot\frac{\partial}{\partial\boldsymbol{r}}(k_B T\ln\Psi) + \boldsymbol{\kappa}\cdot\boldsymbol{x}. \tag{3.13}$$

Defining the translation diffusion constants $D_\parallel = k_B T/\zeta_\parallel$ and $D_\perp = k_B T/\zeta_\perp$, we finally obtain the complete Smoluchowski equation for rotational and translational motion:

$$\begin{aligned}\frac{\partial\Psi}{\partial t} &= -\frac{\partial}{\partial\boldsymbol{x}}\cdot(\mathbf{v}\Psi) - \mathcal{R}(\mathbf{w}\Psi) = \\ &= \frac{\partial}{\partial\boldsymbol{x}}\cdot\left[D_\parallel\boldsymbol{nn} + D_\perp(\mathbf{I} - \boldsymbol{nn})\right]\cdot\frac{\partial\Psi}{\partial\boldsymbol{x}} - \frac{\partial}{\partial\boldsymbol{x}}\cdot\left[(\boldsymbol{\kappa}\cdot\boldsymbol{x})\,\Psi\right] \\ &\quad + \mathcal{R}\left(D_r\mathcal{R}\Psi - \boldsymbol{n}\times(\boldsymbol{\kappa}\cdot\boldsymbol{n})\,\Psi\right).\end{aligned} \tag{3.14}$$

### 3.0.3 Stress tensor

It can be demonstrated that, in a system with holonomic constraints (like the rigidity of the rods), the additional stress tensor $\sigma_{ij}^{(P)}$ due to the presence of polymers can be decomposed in a term proportional to the velocity gradient tensor $\boldsymbol{\kappa}$, called **viscous**, and a term non (explicitly) dependent on $\boldsymbol{\kappa}$, called **elastic**.

$$\sigma_{ij}^{(P)} = \sigma_{ij}^{(E)} + \sigma_{ij}^{(V)}, \qquad \sigma_{ij}^{(V)} = A_{ijkl}\kappa_{kl}. \tag{3.15}$$

Phenomenologically, the viscous stress vanishes instantaneously when the external flow is stopped, and it is related to the energy dissipation, while the elastic stress vanishes only when the system reaches the equilibrium, and it is related to the change in free energy caused by a virtual deformation.

In particular, if $\delta\mathcal{A}$ is the variation in the free energy density $\mathcal{A}$ due to a displacement from $r_i$ to $r_i + \delta\varepsilon_{ij}r_j$, we have $\delta\mathcal{A} = \sigma_{ij}^{(E)}\delta\varepsilon_{ij}$. Since in our system the only potential between polymers is the thermodynamic one, the free energy density is (where $\rho_P$ is the number of rods in unit volume):

$$\mathcal{A} = \rho_P k_B T \int_V d\boldsymbol{n}\Psi \ln\Psi, \tag{3.16}$$

and therefore

$$\delta\mathcal{A} = \rho_P k_B T \int_V d\boldsymbol{n}\left(\delta\Psi \ln\Psi + \delta\Psi\right). \tag{3.17}$$

In order to calculate $\delta\Psi$, we can use the Smoluchowski equation (3.14), which, for an instantaneous deformation is dominated by the velocity gradient $\kappa_{ij} = \delta\varepsilon_{ij}/\delta t$:

$$\frac{\partial\Psi}{\partial t} \simeq -\mathcal{R}\cdot\left(\boldsymbol{n}\times\left(\boldsymbol{\kappa}\cdot\boldsymbol{n}\right)\Psi\right), \quad \Longrightarrow \quad \delta\Psi \simeq -\mathcal{R}\cdot\left(\boldsymbol{n}\times\left(\delta\boldsymbol{\varepsilon}\cdot\boldsymbol{n}\right)\Psi\right). \tag{3.18}$$

Inserting $\delta\Psi$ into $\delta\mathcal{A}$, and integrating by parts:

$$\delta\mathcal{A} = \rho_p k_B T \int d\boldsymbol{n}\left(\boldsymbol{n}\times\left(\delta\boldsymbol{\epsilon}\cdot\boldsymbol{n}\right)\Psi\right)\cdot\mathcal{R}\Psi = \rho_p k_B T \int d\boldsymbol{n}\Psi\mathcal{R}\cdot\left(\boldsymbol{n}\times\left(\delta\boldsymbol{\epsilon}\cdot\boldsymbol{n}\right)\right). \tag{3.19}$$

Since $\mathcal{R}_i n_j = \epsilon_{ijk} n_k$, where $\epsilon_{ijk}$ is the Levi Civita tensor, we have (in three dimensions):

$$\mathcal{R} \cdot (\boldsymbol{n} \times (\delta\boldsymbol{\epsilon} \cdot \boldsymbol{n})) = -3\delta\varepsilon_{ij} \left( n_i n_j - \frac{1}{3}\delta_{ij} \right), \tag{3.20}$$

and therefore:

$$\delta\mathcal{A} = 3\rho_p k_B T \delta\varepsilon_{ij} \int d\boldsymbol{n} \Psi \left( n_i n_j - \frac{1}{3}\delta_{ij} \right) = 3\rho_p k_B T \delta\varepsilon_{ij} \langle n_i n_j - \frac{1}{3}\delta_{ij} \rangle. \tag{3.21}$$

Hence we have the elastic component of the stress, due to the Brownian motion of the rods:

$$\sigma_{ij}^{(E)} = 3\rho_p k_B T \delta \langle n_i n_j - \frac{1}{3}\delta_{ij} \rangle = 3\rho_p k_B T \left( R_{ij} - \frac{1}{3}\delta_{ij} \right), \tag{3.22}$$

where the quantity $\boldsymbol{R} = \langle \boldsymbol{nn} \rangle = \int d\boldsymbol{n} \Psi (\boldsymbol{nn})$ is the polymer configuration tensor, corresponding (or its traceless version $\boldsymbol{R} - (1/3)\mathbf{I}$) to the nematic order parameter of liquid crystal theory. The elastic stress therefore opposes the deviation with respect to the state of thermodynamic equilibrium, with all the rods randomly oriented.

Instead, if $W$ is the hydrodynamic energy dissipation due to the friction of the rods with the surrounding fluid, it is related to the viscous stress by the relationship $W = k_{ij}\sigma_{ij}^{(V)}$. Using the shish-kebab model, the work done by the frictional force on the $a$-th bead is $\mathbf{F}_a \cdot \mathbf{v}_a$. Since the rod rotates with angular velocity $\mathbf{w} = \boldsymbol{n} \times (\boldsymbol{\kappa} \cdot \boldsymbol{n})$, the velocity of the $a$-th bead relative to the fluid is:

$$\mathbf{v}_a = ab\,(\mathbf{w} \times \boldsymbol{n} - \boldsymbol{\kappa} \cdot \boldsymbol{n}) = ab\,([\boldsymbol{n} \times (\boldsymbol{\kappa} \cdot \boldsymbol{n})] \times \boldsymbol{n} - \boldsymbol{\kappa} \cdot \boldsymbol{n}) = -ab\boldsymbol{n}\,(\boldsymbol{\kappa} : \boldsymbol{nn})\,. \tag{3.23}$$

Since the frictional force acting on the $a$-th bead is $\mathbf{F}_a = \zeta_0 \mathbf{v}_a$ (not considering the hydrodynamic interaction between beads), the energy dissipated by unit of space and time is:

$$W = \rho_p \sum_a \langle \mathbf{F} \cdot \mathbf{v}_a \rangle = \rho_p \sum_{a=-N/2}^{N/2} a^2 b^2 \langle (\boldsymbol{\kappa} : \boldsymbol{nn})^2 \rangle = \rho_p \zeta_{\mathrm{str}} \langle (\boldsymbol{\kappa} : \boldsymbol{nn})^2 \rangle. \tag{3.24}$$

If we take in account the hydrodynamic interaction, we have $\zeta_{\text{str}} = \zeta_r/2$. The viscous stress is therefore:

$$\sigma_{ij}^{(V)} = \frac{1}{2}\rho_p \zeta_r \kappa_{kl} \langle n_i n_j n_k n_l \rangle. \tag{3.25}$$

### 3.0.4 Closure approximation and field equations

We are now interested in obtain closed equations viable to be simulated, in order to effectively investigate the phenomenology described by the Doi-Edwards model. From the Smoluchowski equation for the rotational motion, we can obtain the evolution of the configuration tensor $R_{ij}$:

$$\frac{\mathrm{D}R_{ij}}{\mathrm{D}t} = \int n_i n_j \frac{\mathrm{D}\Psi}{\mathrm{D}t} d\boldsymbol{n}, \tag{3.26}$$

where the partial derivative $\partial_t$ is replaced by the material derivative $\mathrm{D}_t = \partial_t + \mathbf{u} \cdot \nabla$ in order to take in account the transport by the fluid flow. Hence we have (it is important to notice that the non-Browian part of the evolution can be obtained directly from the Jeffery equation):

$$\frac{\partial R_{ij}}{\partial t} + u_k \partial_k R_{ij} = \kappa_{ik} R_{kj} + R_{ik} \kappa_{jk} - 2\kappa_{kl} \langle n_i n_j n_k n_l \rangle - 2D_r \left(3R_{ij} - \delta_{ij}\right). \tag{3.27}$$

We can observe a problem: in order to compute the temporal evolution of the second order moment $\langle n_i n_j \rangle = R_{ij}$ we need to know the fourth order moment $\langle u_i u_j u_k u_l \rangle$. But to compute the evolution of the fourth order momentum we need to know the sixth order momentum, and so on. This infinite hierarchy of equations is denoted closure problem, and it is quite common in statistical physics. We therefore want to express $\langle n_i n_j n_l n_k \rangle$ in terms of $R_{ij}$, both in the equation for the evolution of $R_{ij}$ and in the viscous stress tensor.

Such a relationship is defined closure approximation, and it must satisfy two fundamental properties: to alter the predictions of the model as little as possible, and to be feasible to be numerically implemented. Probably the most simple one is the one proposed by Doi and Edwards themselves [24]:

$$\langle n_i n_j n_k n_l \rangle \kappa_{kl} \simeq A \langle n_i n_j \rangle \langle n_k n_l \rangle \kappa_{kl} + B \langle n_i n_k \rangle \langle n_j n_l \rangle \left(\kappa_{kl} + \kappa_{lk}\right), \tag{3.28}$$

that we want to be exact for the traces:

$$\langle n_i n_i n_k n_l \rangle \kappa_{kl} = A \langle n_i n_i \rangle \langle n_k n_l \rangle \kappa_{kl} + B \langle n_i n_k \rangle \langle n_i n_l \rangle \left( \kappa_{kl} + \kappa_{lk} \right). \quad (3.29)$$

This implies $A = 1$ and $B = 0$, and therefore the Doi-Edwards closure is:

$$\langle n_i n_j n_k n_l \rangle \kappa_{kl} \simeq \langle n_i n_j \rangle \langle n_k n_l \rangle \kappa_{kl} = R_{ij} \left( \partial_l u_k \right) R_{kl}. \quad (3.30)$$

This is a very simple closure, which has the important advantage of preserving the symmetry ($R_{ij} = R_{ji}$) and trace ($R_{ii} = 1$) of the configuration tensor. A certain number of more complicated closures have been proposed through the years. [76–79] As an example, the hybrid closure by Advani and Tucker [76] consists in:

$$\langle n_i n_j n_k n_l \rangle = f R_{ij} R_{kl} + (1 - f) A_{ijkl}, \quad (3.31)$$

with $f = 1 - 27 \det \left( R_{ij} \right)$ and

$$A_{ijkl} = -\frac{1}{35} \left( \delta_{ij}\delta_{kl} + \delta_{ik}\delta_{jl} + \delta_{il}\delta_{jk} \right) + \frac{1}{7} \left( R_{ij}\delta_{kl} + R_{ik}\delta_{jl} + R_{il}\delta_{jk} + R_{kl}\delta_{ij} + R_{jl}\delta_{ik} + R_{jk}\delta_{il} \right). \quad (3.32)$$

We shall adopt the Doi-Edwards closure. In literature it is common to neglect the elastic component of the stress, and to express the product between friction factor and polymer density in terms of a normalized single feedback coefficient $\eta$. [21, 41, 70] With this assumption, we finally have the equations describing the dynamics of a dilute solution of rod-like polymers, according the Doi-Edwards model:

$$\left( \partial_t + u_k \partial_k \right) u_i = -\partial_i p + \nu \partial^2 u_i + \partial_k \sigma_{ik} + f_i, \quad (3.33a)$$

$$\left( \partial_t + u_k \partial_k \right) R_{ij} = \left( \partial_k u_i \right) R_{kj} + R_{ik} \left( \partial_k u_j \right) - 2 R_{ij} \left( R_{kl} \partial_l u_k \right) - 2 D_r \left( 3 R_{ij} - \delta_{ij} \right), \quad (3.33b)$$

$$\partial_i u_i = 0, \qquad \sigma_{ij} = 6 \nu \eta R_{ij} \left( R_{kl} \partial_l u_k \right). \quad (3.33c)$$

According [24], the equations (3.33) are valid also in the semi-diluted regime, but with a different dependence of coefficients on shape and density.

## 3.1 Hinch and Leal rheological theory

The rheological theory of Hinch and Leal [73, 74] is strictly related to the one of Doi and Edwards. Contrarily to the latter, in this theory rigid polymers are not approximated as a sequence of small beads (an approach adopted by Doi and Edwards also for other typologies of polymers), but with axis-symmetric ellipsoids (spheroids), taking advantage of the fact that for such a regular shape it is possible to obtain many exact results. In particular is based on the calculation of the resistance and mobility functions and their consequences on the rheology of the solvent, an approach which started from the PhD thesis of Albert Einstein, who, in the meantime he upset the foundations of physics, also found the time to compute the effective viscosity of a suspension of spherical particles at first order in the sphere volume fraction $c$: [80]

$$\mu_{eff} \simeq \mu_0 \left(1 + \frac{5}{2}c\right). \tag{3.34}$$

After Einstein, other important scholars carried on these studies, in particular Jeffery, Giesekus, Bretherton and Batchelor, right up to the theory of Hinch and Leal. Also in this case the dynamics of the system is described by the configuration tensor $R_{ij}$, on which an additional stress $\sigma_{ij}$ depends. The equation for $R_{ij}$ is identical to the one establishes by Doi and Edwards, but it is generalized to the case of generic aspect ratio $r_a$ (the velocity gradient tensor $\boldsymbol{\kappa}$ is therefore decomposed into its symmetric $\boldsymbol{\Sigma}$ and anti-symmetric $\boldsymbol{\Omega}$ parts):

$$\begin{aligned} \frac{D}{Dt}\langle \boldsymbol{nn} \rangle &= \boldsymbol{\Omega} \cdot \langle \boldsymbol{nn} \rangle + \langle \boldsymbol{nn} \rangle \cdot \boldsymbol{\Omega}^T \\ +a_0 \left( \boldsymbol{\Sigma} \cdot \langle \boldsymbol{nn} \rangle + \langle \boldsymbol{nn} \rangle \cdot \boldsymbol{\Sigma}^T - \langle \boldsymbol{nnnn} \rangle : \boldsymbol{\Sigma} \right) &- 2D_r \left( 3\langle \boldsymbol{nn} \rangle - \mathbf{I} \right), \end{aligned} \tag{3.35}$$

where $a_0 = (r_a^2 - 1)/(r_a^2 + 1)$ is the Jeffery geometrical factor. The bulk stress $\boldsymbol{\sigma}$ instead has a more generic form (obtained originally by Giesekus [81]):

$$\boldsymbol{\sigma} = 2\mu c \left[ 2A\langle \boldsymbol{nnnn} \rangle : \boldsymbol{\Sigma} + 2B \left( \langle \boldsymbol{nn} \rangle \cdot \boldsymbol{\Sigma} + \boldsymbol{\Sigma} \cdot \langle \boldsymbol{nn} \rangle \right) + C\boldsymbol{\Sigma} + FD_r \langle \boldsymbol{nn} \rangle \right]. \tag{3.36}$$

Here, $A, B, C$ and $F$ are geometrical factors depending on aspect ratio $r_a$. For elongated rods, in the limit $r_a \to \infty$ we have:

$$A = \frac{r^2}{4\left(\ln\left(2r\right)\right) - 3/2}, \quad B = \frac{3\left(2r\right) - 1/2}{r^2}, \quad C = 2, \quad F = \frac{3r^2}{\ln\left(2r\right) - 1/2}. \tag{3.37}$$

The fact that $B \to 0$, differently from $A$ and $F$, is compatible with the Doi and Edwards model. Instead $C \neq 0$ implies also a change in the effective Newtonian viscosity, an effect not considered in [24]. Apparently there is a difference also in the form of the Brownian stress, but $\nabla \cdot \langle \boldsymbol{nn} \rangle = \nabla \cdot (\langle \boldsymbol{nn} \rangle - \mathbf{I})$.

If $r_a = 1$ (spherical particles) we have $A = B = F = 0$ and $C = 5/2$, thus recovering the Einstein relationship. A suspension of spherical particles is therefore still a Newtonian fluid, with a viscosity modified with respect the bare solvent one.

Finally, for discoidal particles ($r_a \to 0$) we have all the coefficients different from 0, and in particular $A/B \to 5/2$. Therefore, a dilute suspension of rigid disks would have a dynamic similar to the one described in (3.33), with a change of sign in the terms depending on $\kappa_{ij}$ in the equation for $R_{ij}$ and a non-Newtonian viscous stress with an additional term:

$$\sigma_{ij} = 6\nu\eta \left[ R_{ij} \left( R_{kl} \partial_l u_k \right) + \frac{2}{5} \left( R_{ik} \partial_k u_j + R_{kj} \partial_k u_i \right) \right]. \tag{3.38}$$

A similar theory was proposed also by Brenner [72], with a more complicated dependency of the coefficients on the aspect ratio. While for asymptotic $r_a$ the coefficients of the two theories are equivalent, there are differences for finite $r_a$.

# Chapter 4

# Kolmogorov flow

This chapter is not explicitly related to polymer solutions, but it describes the configuration we selected to investigate them.

The particular configuration we decided to use is the so-called Kolmogorov flow. [82] It was conceived by A. N. Kolmogorov, who described it, along other problems in mathematical physics, in a seminar in 1958-59, and it was published by V. I. Arnold and L. D. Meshalkin in 1960. [83]

Kolmogorov was interested in the transition from laminar to turbulent flow, due to increasing of Reynolds number. For this reason, he proposed an ideal setting, characterized by:

- periodic boundary conditions and absence of solid bodies;
- sinusoidal (or cosinusoidal) forcing: $\boldsymbol{f} = F\left(\sin(Kz), 0, 0\right)$.

Periodic boundary conditions are usually employed in the study of fundamental properties of turbulence, in order to disregard effects due to interaction with walls. The sinusoidal forcing induces a simple laminar solution:

$$\boldsymbol{u} = U_0\left(\sin(Kz), 0, 0\right), \qquad \text{with} \quad U_0 = F/\left(\nu K^2\right), \tag{4.1}$$

which permits to perform analytic studies about the flow.

The Kolmogorov flow is clearly an ideal setting (although it is possible to experimentally realize a sinusoidal forcing using electromagnetic fields [84, 85]), useful if we are interested in bulk properties of shear flows: it

can be considered a channel flow without boundaries, [86] that, due to this feature, can represent also a good approximation of some geophysical flows. [87, 88]

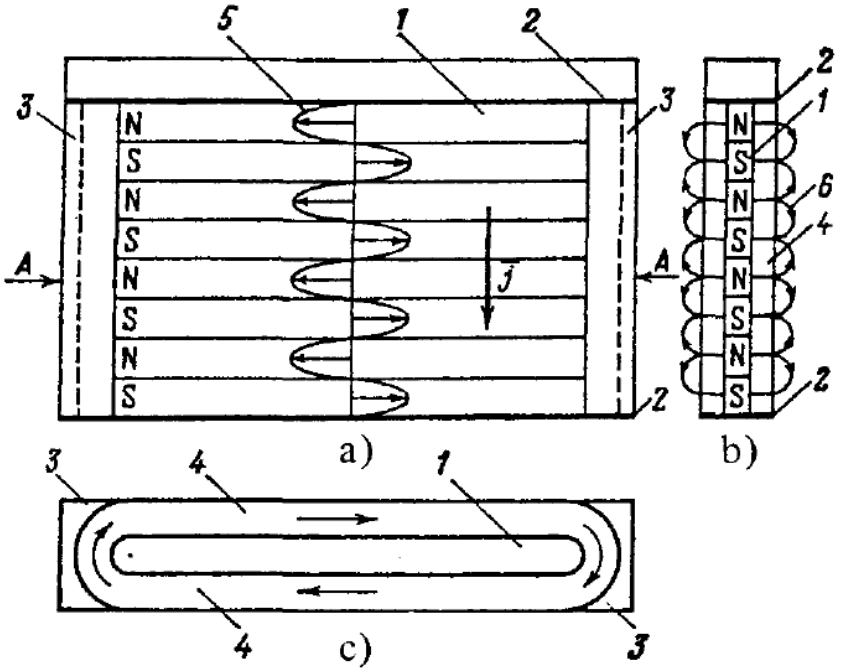


**Figure 4.1:** Sketch of an experimental magnetohydrodynamic realization of the Kolmogorov flow, using a solution of copper sulphate as fluid. [84]

Linear stability of 4.1 was already investigated in 1961 [89]: the laminar flow becomes unstable to transverse large-scale (*i.e.* larger than forcing scale $1/K$) perturbations if Reynolds number (defined using $U_0$ as velocity scale and $1/K$ as spatial scale) exceeds the threshold $\boxed{Re_c = \sqrt{2}}$.

After the first paper regarding linear stability, [89] a large number of studies has followed: from analytical and numerical investigation on the states resulting from the instability, [90–92] to numerical simulation of the fully turbulent state at high Reynolds, [86, 93], but also various generalizations: compressible flows, [94] Rossby waves presence, [87] stratified flows, [95] confinement, [96] advection of passive particles [97] or microswimmers, [98, 99] and non-Newtonian fluids, such as viscoelastic polymer solutions (with linear and non-linear stability analysis, [100, 101] and observations of elastic turbulence, [58] elastic waves [66] and polymer

drag reduction [46]) and dusty flows. [102, 103]

Stability analyses are usually performed in two-dimensions, due to Squire's theorem which states that for parallel flows the most unstable perturbations are two-dimensional, [104] while other studies can be performed both in two or three dimension, since dimensionality of the system can strongly affect the flow dynamics (especially in fully developed turbulence, where 2D and 3D flows are qualitatively different [105]). In two dimensions (2D), our convention is to define $x$ as the mean flow direction and $y$ as the mean gradient direction, while in three-dimension (3D) $x$ is the mean flow direction, $y$ the "neutral" one (no dependence on $y$ in the laminar solution) and $z$ the mean gradient one.

One of the most interesting features of the Kolmogorov flow is that the sinusoidal profile of velocity field is maintained also in the turbulent regime, [86] or in other chaotic flows. [58] If we denote with overbar the averaging along time, mean flow and neutral directions ($x$ and $y$) in the Newtonian turbulent regime we will have (using a cosinusoidal forcing):

$$\overline{\boldsymbol{u}\left(\boldsymbol{x},t\right)} = \left[U\cos\left(Kz\right),0,0\right]. \tag{4.2}$$

Even more interesting is the fact that also the $x-z$ component of the second order moment of the velocity is monochromatic:

$$\overline{u_x u_z\left(\boldsymbol{x},t\right)} = S\sin\left(Kz\right), \tag{4.3}$$

which means that, if we consider the (stationary) momentum budget (obtained averaging Eq. 1.1 along $t, x$ and $y$):

$$\partial_z \Pi_r = \partial_z \Pi_\nu + f_x, \tag{4.4}$$

where viscous and Reynolds stress are defined as:

$$\Pi_\nu = \nu\partial_z\overline{u_x}, \qquad \Pi_r = \overline{u_x u_z}, \tag{4.5}$$

the momentum budget equation will become an algebraic relationship between coefficients:

$$SK + \nu K^2 U = F. \tag{4.6}$$

This relationship is sometimes non-dimensionalised by defining the friction factor $f = F/(KU^2)$ and the Reynolds stress coefficient $s = S/U^2$:

$$f = \frac{1}{Re} + s. \tag{4.7}$$

In the laminar flow, being $u_z = 0$, we have $s = 0$ and therefore $f = 1/Re$, while in 3D fully developed turbulent flows [86] it has been numerically shown that asymptotically ($Re \gtrsim 160$) we have:

$$f = f_0 + \frac{b}{Re} \qquad \Longrightarrow \qquad s = f_0 + \frac{b-1}{Re}, \tag{4.8}$$

with $f_0 \simeq 0.124$ and $b \simeq 5.75$ (see Fig. 4.2).

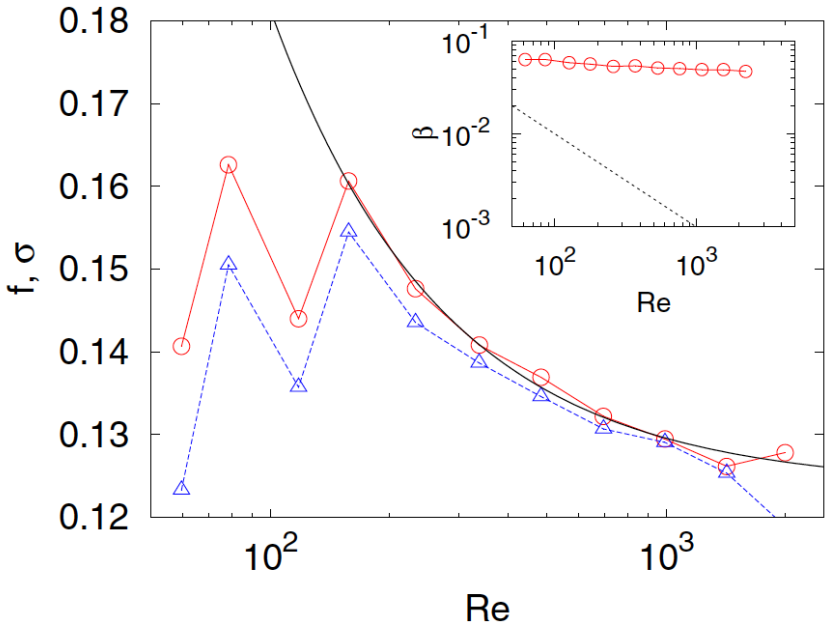


**Figure 4.2:** Asymptotic scaling, as a function of Reynolds number $Re$ of non-dimensional coefficients $f = FL/U^2$ and $s = S/U^2$ (here denoted as $\sigma$) in the turbulent Kolmogorov flow, as shown in [86]. The dissipation factor $\beta = \epsilon L/U_{rms}$ as a function of $Re$ is shown in the inset, compared to the laminar value $\beta_{lam} = 1/Re$.

In non-Newtonian fluids the relationship 4.4 will be enriched by supplementary terms related to non-Newtonian stresses, but the monochromatic behaviour will be still present. [58, 70, 102]

# Chapter 5

# Chaotic flows at low-Reynolds number

## 5.1 Introduction

As it has been described in chapter 2, recent two-dimensional numerical simulations have shown that rigid rod-like polymers originate, at low Reynolds number, a chaotic regime similar to elastic turbulence, [70] including the enhancement of mixing. [71]

While in turbulent flows at high-Reynolds numbers the dimensionality of the system has dramatic consequences on the dynamics, such as the reversal of the turbulent cascade of kinetic energy, [106,107] the behaviour of chaotic flows at low Reynolds is expected to be qualitatively similar in 2D and 3D. This feature implies the possibility to use 2D studies for the modelling of 3D applications, since it offers us considerable advantages, such as the reduction of the computational cost and the simplification of experimental setups. Nonetheless, quantitative discrepancies between 2D and 3D results can be observed, due to the change of dimensionality. An example of this discrepancy has been recently noted in numerical studies of Rayleigh-Taylor convection in porous media, with a faster growth of the mixing layer in two dimensions, related to density plumes more elongated and thinner in 2D than in the 3D case [108, 109]. In order to evaluate the validity of 2D studies of low Reynolds flows, the comparison of 3D and

2D studies is therefore crucial.

The purpose of our study is therefore the extension to three dimensional (3D) flows of the investigation of the chaotic regime in viscous solutions of rod-like polymers. In particular, here we present the results of numerical simulations in 3D of the rheological model considered in [70,71] together with two-dimensional (2D) simulations performed with identical parameters for comparison. We find that the qualitative phenomenology of 2D and 3D systems is similar, in particular increasing the concentration of polymers we find an enhancement of the flow resistance, which can be quantified by the friction factor, as well as an increased mixing efficiency. The latter property is investigated by measuring the decay rate of the variance of a scalar field passively transported by the flow. Nonetheless, between 3D and 2D simulations quantitative differences are revealed by an accurate comparison. In particular the effects of polymers in 2D is observed to be stronger than in 3D. An interpretation of this dimensional effect, in terms of the rotational degrees of freedom of polymers, is offered. We also discuss the possibility of a mapping between the 2D and 3D results obtained by rescaling the concentration of polymers.

## 5.2 Model and simulations

In order to describe a dilute solution of rigid rod-like polymers, we considered the Doi-Edwards model [24] (described in chapter 3):

$$\partial_t u_i + u_k \partial_k u_i = -\partial_i p + \nu \partial^2 u_i + \partial_k \sigma_{ik} + f_i, \tag{5.1a}$$

$$\partial_t R_{ij} + u_k \partial_k R_{ij} = (\partial_k u_i) R_{kj} + R_{ik}(\partial_k u_j) - 2R_{ij}(\partial_l u_k) R_{kl}, \tag{5.1b}$$

where $\boldsymbol{u}(\boldsymbol{x}, t)$ is the velocity field, $\boldsymbol{R}(\boldsymbol{x}, t)$ the polymer configuration tensor, $p(\boldsymbol{x}, t)$ the kinematic pressure, $\nu$ the kinematic viscosity, $\boldsymbol{f}(\boldsymbol{x}, t)$ the external forcing, and $\sigma_{ij} = 6\nu\eta R_{ij}(\partial_l u_k) R_{kl}$ the polymer stress tensor. We recall that equation (5.1b) should also contain a term related to the orientational diffusion of polymers [24]. However, if the characteristic Brownian rotational time $t_B$ is much larger than the dynamical rotational time $t_L$, determined by the velocity gradients, we can disregard the ef-

fects of Brownian rotations of the rods. [110] The dynamical time can be estimated as $t_L \approx (L^2/\nu)Re^{-1}$, where $L$ is the characteristic scale of the flow and $Re$ is the Reynolds number, while, for an elongated particle of length $\ell$ and aspect ratio $r_a$ in a solvent with density $\rho$ at temperature $T$, the Brownian time is given by $t_B = (\pi\rho\nu\ell^3) / (3k_BT (\ln (r_a) - 0.8))$ where $k_B$ is the Boltzmann constant [24]. If we consider an experiment in a microchannel of width $L \approx 1\ mm$ at $Re \approx 1$, with rigid fibers of length $\ell = 5\ \mu m$ and aspect ratio $r = 10$ in water at $T = 300\ K$, the dynamical time $t_L \approx 1\ s$ is much smaller than the Brownian time $t_B \approx 20\ s$. Having these applications in mind, in the following we disregard the Brownian term.

We considered here a 3D viscous shear flow sustained by the Kolmogorov body force (described in chapter 4) $\boldsymbol{f}(\boldsymbol{x}) = (F\cos(Kz), 0, 0)$, where $F$ is the amplitude and $K$ is the wavenumber of the force. In absence of polymers ($\eta = 0$) this force generates a stationary laminar solution $\boldsymbol{u}(\boldsymbol{x}) = (U_0\cos(Kz), 0, 0)$ with $U_0 = F/(K^2\nu)$, which is linearly stable if the Reynolds number $Re = U_0/(\nu K)$ is smaller than the critical value $Re_c = \sqrt{2}$ [89]. The laminar solution of (5.1a) with $\eta > 0$ is the same Kolmogorov flow $(U_0\cos(Kz), 0, 0)$ with amplitude $U_0 = F/(K^2\nu)$ independent on the polymer concentration (at variance with viscoelastic models in which the presence of polymers affects the amplitude of the laminar flow [46]). In this case from the (5.1b) we have, for the conformation tensor, $R_{i3} = R_{3i} = 0$ and $\partial_x R_{ij} = 0$, i.e. polymers oriented in the $x - y$ plane and their orientation can be a function only of the $y$ and $z$ coordinates.

### 5.2.1 Numerical simulations

We integrated (5.1) on a triply periodic domain of size $L = 2\pi$, by using a pseudo-spectral code which discretizes the velocity and conformation tensor fields on a regular grid of $N^3 = 256^3$ gridpoints. Since (5.1) contains terms which are cubic in the fields, a 1/2 dealiasing is required at each time step [111]. Time integration is performed with a fourth-order Runge-Kutta scheme [112] with implicit integration of the

linear dissipative terms, and the time step is fixed by the resolution of the rotational dynamics of the conformation tensor. Numerical methods are described in a more detailed way in Appendix A.

In all our ensemble of simulations the viscosity is set to $\nu = 1$ and the flow is sustained by the Kolmogorov force $\boldsymbol{f}(\boldsymbol{x}) = (F\cos(Kz), 0, 0)$, with forcing wavenumber $K = 4$ and forcing amplitude $F = \nu^2 K^3$, which implies that, in absence of polymers ($\eta = 0$), the laminar flow is linearly stable with Reynolds number $Re = U_0/(\nu K) = 1$. The feedback coefficient is varied from $\eta = 5$ to $\eta = 8$. Experimentally this corresponds, for the case of an aqueous solution of xanthan gum, to concentrations in the range of $73 - 102$ wppm. [36] We considered values of $\eta$ small enough to be in the dilute regime, but also large enough to ensure that the system is far from the transition from the laminar to the chaotic flow observed in [70].

We added a diffusive term $\kappa\partial^2 R_{ij}$ with $\kappa = 4 \times 10^{-3}$ to eq. (5.1b) in order to prevent the emergence of numerical instabilities [113]. All the quantities are made dimensionless by using the forcing wavenumber $K$, the amplitude of the laminar velocity $U_0$ and the laminar time-scale $T_0 = 1/(KU_0)$. In order to have a quantitative comparison between the 2D and the 3D versions of the model, we also performed additional numerical simulations of (5.1) in a two dimensional periodic domain with the same parameters of the 3D runs.

The velocity field at time $t = 0$ is initialized to the fixed-point laminar solution, while the components of the tensor $R$ are initially distributed randomly with isotropic distribution. The time evolution of the kinetic energy $E = \frac{1}{2}\langle|\boldsymbol{u}|^2\rangle$ is shown in Figure 5.1 for two simulations with $\eta = 6$ and $\eta = 8$ (here and in the following $\langle\cdot\rangle$ denotes the average over the whole volume). Injecting the polymers the velocity field is strongly affected, with the energy almost reduced to zero. Energy further increases back almost to the laminar value (at $t \simeq 200T_0$ in Fig. 5.1) where the instabilities due to polymers develop, with the system eventually reaching a statistically stationary chaotic state (at $t \geq 500T_0$). In this regime the energy is considerably smaller than the one of the laminar flow $E_0 =$

$\frac{1}{2}U_0^2$, and it displays rapid oscillations whose frequency increases with the polymer concentration, while the average value of $E$ decreases at increasing $\eta$.

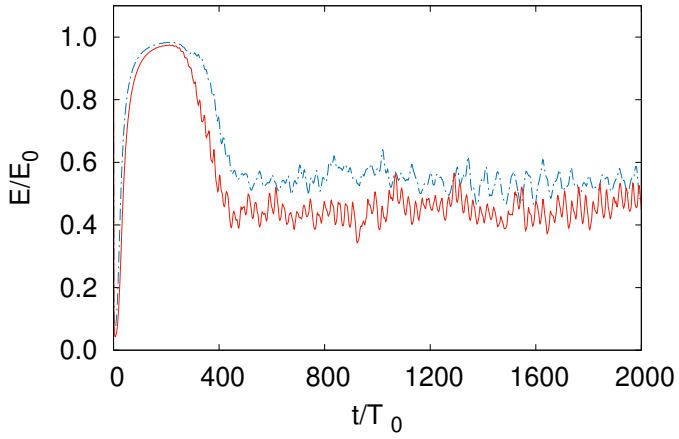


**Figure 5.1:** Kinetic energy $E$, normalized with the laminar energy $E_0$, for two simulations in 3D with $\eta = 6$ (blue dashed line) and $\eta = 8$ (red solid line). In both cases the initial condition is the laminar fixed point with $E(0) = E_0$.

For each value of the parameters, a set of three independent simulations, with different realizations of the initial random configuration of the conformation tensor, is performed. While the properties of the initial transient are strongly depending on the realization, the subsequent chaotic regime displays statistically equivalent properties between different realizations, and they are averaged to increase the statistical accuracy of the results. All the results we presented are obtained in this statistically stationary regime.

Figure 5.2 shows three sections of the velocity components $u_x$,$u_y$ and $u_z$ in the plane $x-z$ at fixed $y$ from a simulation with $\eta = 7$ in the stationary chaotic flow. The structure of the Kolmogorov flow remains visible in the $u_x$ field, with superimposed irregular fluctuations at small scales which are clearly more evident in the $u_y$ and $u_z$ fields, where the mean flow is absent. We remark that the fluctuations in the $u_x$ field qualitatively resemble the elastic waves observed in viscoelastic flows. [66, 67]

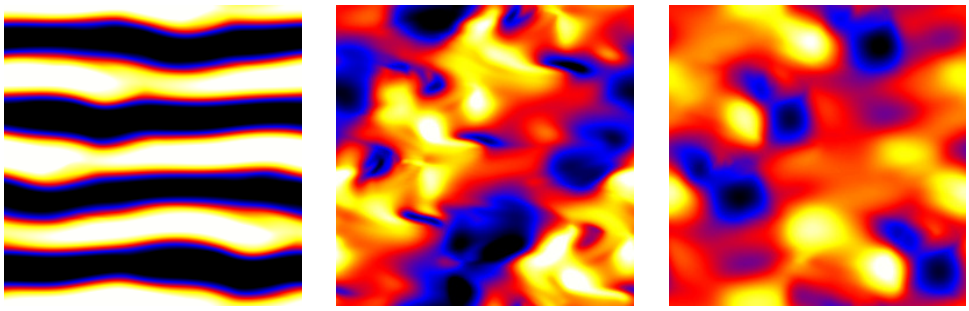

**Figure 5.2:** Vertical sections in the $x-z$ plane of the velocity components $u_x$, $u_y$, $u_z$ (from left to right) in the 3D chaotic regime for $\eta = 7$. The color scale ranges from $-3u_i'$ (black) to $3u_i'$ (white), where $u_i'$ are the rms values of the velocity fluctuations.

## 5.3 Results

### 5.3.1 Statistics of the velocity

As we already described in Chapter 4, the most relevant feature of the Kolmogorov flow is that, also in the chaotic and in the turbulent regimes, it maintains a monochromatic mean flow $\langle u_x \rangle = U\cos(Kz)$. This property is confirmed even in the presence of rigid polymers, as shown in Fig. 5.3, where the average velocity profile, from the simulations at different concentrations, is plotted. We note that the amplitude of the mean flow is significantly reduced with respect to the laminar solution, consistently with the energy trends shown in Fig. 5.1, as a consequence of the chaotic motion induced by polymers.

This property therefore allows us to decompose the velocity field in a mean (monochromatic) component and fluctuations as

$$\boldsymbol{u}\left(\boldsymbol{x}\right) = U\left(\cos\left(Kz\right), 0, 0\right) + \boldsymbol{u}'(\boldsymbol{x}) \tag{5.2}$$

Table 5.1 reports the values of the (root-mean-square) rms velocity fluctuations, together with the amplitude of the mean flow and other relevant quantities we will consider.

Figure 5.4 confirms that the amplitude of the mean flow is significantly reduced with respect to the laminar case and that this effect becomes more relevant at increasing values of the concentration parameter $\eta$. The rms values of velocity fluctuations appear, on the contrary, to do

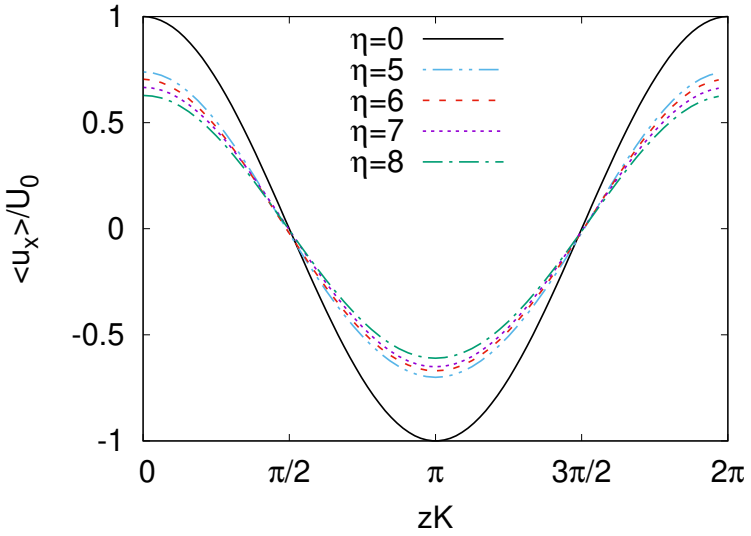


**Figure 5.3:** Profiles of the mean velocity $\langle u_x(z) \rangle$ averaged over $x$, $y$ and time, in 3D simulations with different values of $\eta$. The solid black line corresponds to the laminar solution of the Newtonian fluid at $\eta = 0$.

| $\eta$ | U | S | $\Sigma$ | $u'_x$ | $u'_y$ | $u'_z$ | $\varepsilon_I$ | $\varepsilon_\nu$ | $\varepsilon_p$ |
|---|---|---|---|---|---|---|---|---|---|
| 5 | 2.87 | 0.10 | 4.40 | 0.64 | 0.12 | 0.40 | 91.9 | 74.8 | 17.1 |
| 6 | 2.74 | 0.10 | 5.02 | 0.63 | 0.13 | 0.39 | 87.2 | 68.6 | 18.6 |
| 7 | 2.63 | 0.10 | 5.57 | 0.64 | 0.16 | 0.39 | 83.2 | 63.6 | 19.6 |
| 8 | 2.48 | 0.09 | 6.08 | 0.69 | 0.18 | 0.40 | 78.8 | 58.3 | 20.6 |

**Table 5.1:** Parameters of the 3D simulations. $U$ is the amplitude of the mean longitudinal velocity, $S$ the amplitude of the mean Reynolds stress and $\Sigma$ that of the mean polymer stress. $u'_x$, $u'_y$ and $u'_z$ are the rms values of the three components of velocity fluctuations. $\varepsilon_I$ is the mean energy input, $\varepsilon_\nu$ the viscous energy dissipation and $\varepsilon_p$ the mean polymer dissipation.

not have a relevant dependence on $\eta$. We observe also that fluctuations along streamwise direction $u'_x$ are the strongest, followed by those in the $z$ direction, while fluctuations in the spanwise direction $u'_y$ are significantly smaller. These results suggest that, even in the chaotic regime, the dynamics of the flow remains approximately two-dimensional.

### 5.3.2 Drag and momentum budget

The momentum budget can give us a better comprehension of the effect of the polymers on the flow. By averaging the first component of

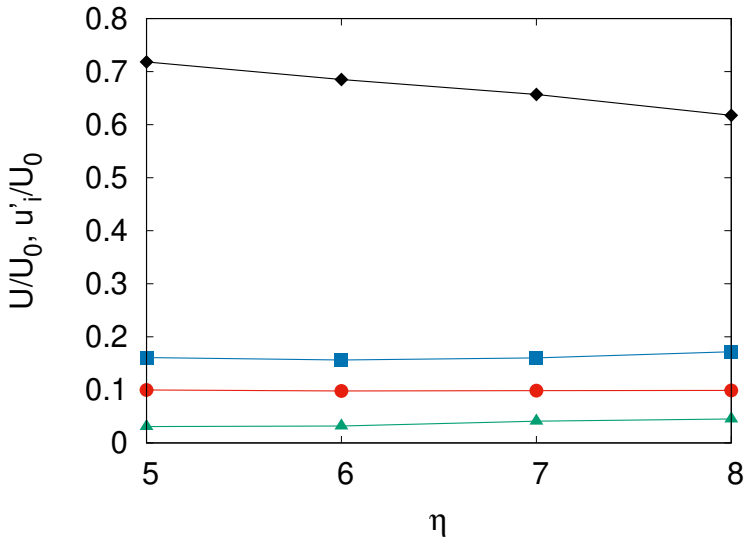


**Figure 5.4:** Mean velocity profiles $U$ (black diamonds) and components of rms velocity fluctuations ($u'_x$ blue squares, $u'_y$ green triangles, $u'_z$ red circles) in 3D simulations with different values of $\eta$.

(5.1) over $x$, $y$ in stationary conditions we obtain the stress budget

$$\partial_z \Pi_r = \partial_z \left( \Pi_\nu + \Pi_p \right) + f_x, \tag{5.3}$$

where $\Pi_r = \overline{u_x u_z}$ is the Reynolds stress, $\Pi_\nu = \nu \partial_z \overline{u_x}$ the viscous stress, and $\Pi_p = \overline{\sigma_{xz}}$ the polymer stress. In the statistically stationary state all these quantities display a monochromatic profile

$$\Pi_r = S \sin(Kz), \qquad \Pi_\nu = -\nu K U \sin(Kz), \qquad \Pi_p = -\Sigma \sin(Kz), \tag{5.4}$$

and therefore (5.3) becomes an algebraic equation for the coefficients

$$SK + \nu K^2 U + \Sigma K = F. \tag{5.5}$$

Dividing all the terms of (5.5) by $KU^2$ we obtain the dimensionless version of the momentum budget, where we define the friction coefficient $f = F/(KU^2)$, which quantifies the ratio between the work done by the force and the kinetic energy of the mean flow, the Reynolds stress coefficient $s = S/U^2$ and the polymer stress coefficient $\sigma = \Sigma/U^2$:

$$f = \frac{1}{Re} + s + \sigma \tag{5.6}$$

In the laminar solution we have $s = \sigma = 0$ and $f = 1/Re$. Figure 5.5 shows that the increase of the polymers concentration produces an enhancement of the friction factor with respect to the laminar case, which is mostly due to the increment of the polymer stress and partly also to a weaker growth of the viscous stress. The Reynolds stress remains in all cases negligible, showing that inertial terms do not contribute to the transfer of momentum.

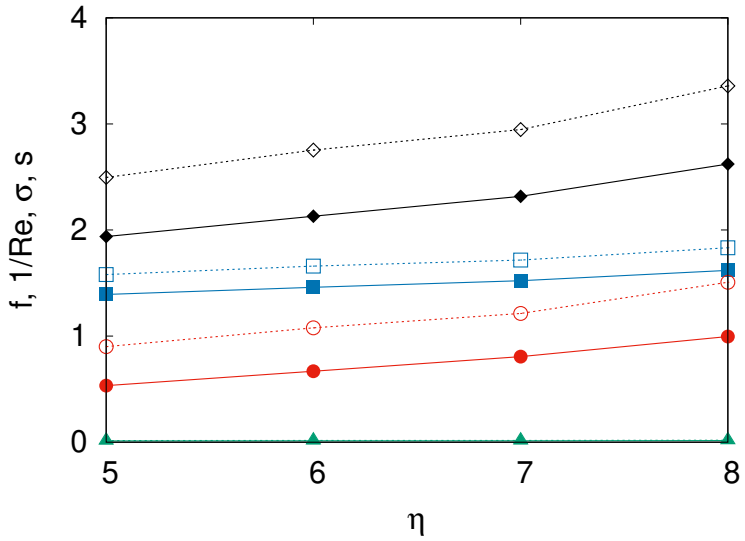


**Figure 5.5:** Friction factor $f$ (black diamonds) normalized viscous stress $1/Re$ (blue squares), polymer stress coefficient $\sigma$ (red circles) and Reynolds stress coefficient $s$ (green triangles), as function of $\eta$. Filled symbols are for the three-dimensional DNS, empty ones are for the two-dimensional DNS.

By definition, the Reynolds number $Re$ and the drag coefficient $f$ are linked by $f = Re_0/Re^2$, where $Re_0 = U_0/K\nu = F/K^3\nu^2$ is the Reynold number of the laminar solution. Polymers therefore exert two complementary effects: they reduce the Reynolds number of the flow and increase its resistance. We notice also that the contribution of the polymer stress ($\propto 1/Re^2$) is dominant compared to that of the viscous stress ($\propto 1/Re$) to the increase of the drag coefficient. This is clearly shown in Figure 5.6 in which the friction factor $f$ is plotted as a function of $Re$ for the different values of $\eta$. Since both $f$ and $Re$ have not an explicit dependence on $\eta$, points corresponding to simulations at the same $F$ and

$\nu$ lie on the same line $Re_0/Re^2$. The point at $Re = 1$ corresponds to the laminar fixed point, which is stable in the absence of polymers. We remark that this plot is done keeping fixed the forcing $F$, so the different Reynolds numbers are due to the different mean velocities produced at various $\eta$. The inset of Fig. 5.6 instead shows how the effective viscosity $\nu_{eff} \equiv F/(K^2U)$ increases as a function of the mean shear rate $\dot{\gamma} = KU$, obtained by varying the amplitude $F$ of the forcing at fixed polymer concentration (data from two-dimensional simulations). In this range of values, the polymer solution displays a shear-thickening behaviour.

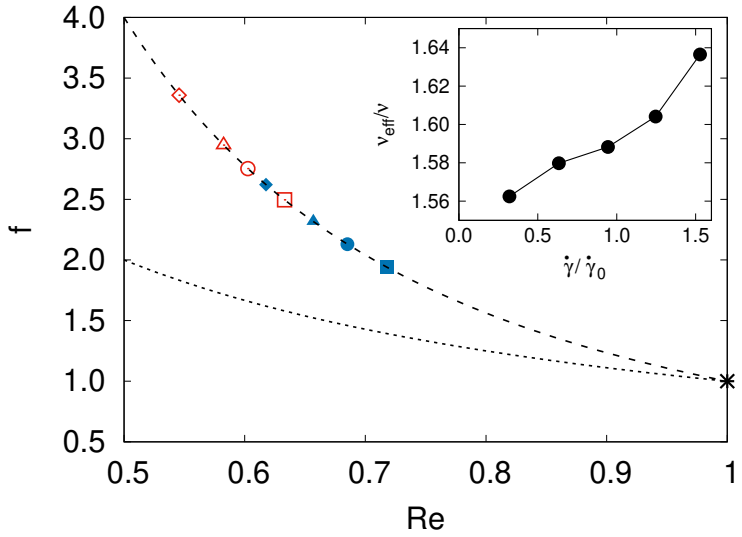


**Figure 5.6:** Friction factor $f$ as a function of $Re$ in the 3D (blue, filled symbols) and 2D (red, empty symbols) simulations at concentrations $\eta = 5$ (squares), $\eta = 6$ (circles), $\eta = 7$ (triangles), $\eta = 8$ (diamonds). The black asterisk at $Re = 1$ represents the laminar fixed point at $\eta = 0$. The dashed line represents the curve $f = Re_0/Re^2$ while the dotted line is the laminar law $f = 1/Re$. Inset: effective viscosity $\nu_{eff}$ as a function of the mean shear rate $\dot{\gamma}$ for $2D$ simulations with $\eta = 5$.

### 5.3.3 Energy budget

From the analysis of the energy budget we get additional information regarding the effects of polymers on the flow. If we multiply (5.1) by $\boldsymbol{u}$, and we integrate over the volume, we obtain the balance equation for the mean kinetic energy (we remark that, unlike he case of elastic polymers,

we cannot associate a deformation energy to rigid polymers, in absence of Brownian effects [24])

$$\frac{d}{dt}\langle E\rangle = \varepsilon_I - \varepsilon_\nu - \varepsilon_p, \tag{5.7}$$

where $\varepsilon_I = \langle \boldsymbol{f} \cdot \boldsymbol{u}\rangle = FU/2$ is the mean energy input, $\varepsilon_\nu = \langle \nu \left|\nabla \boldsymbol{u}\right|^2\rangle$ the mean viscous dissipation rate, and $\varepsilon_p = \langle \sigma_{ij}\partial_j u_i\rangle$ is an additional dissipation of kinetic energy due to the coupling with polymers. We remark that the local values of the term $\sigma_{ij}\partial_j u_i$ can be either positive or negative, meaning that polymers can locally either give or subtract energy from the flow. Nonetheless the volume average of $\varepsilon_p$ is always negative, indicating that the global effect of polymers is dissipative. Physically, this is due to the fact that the coupling between rods and the fluid is due to viscous forces at the molecular scale, whose mean effect is to dissipate a fraction of the kinetic energy [24] (see also Chapter 3).

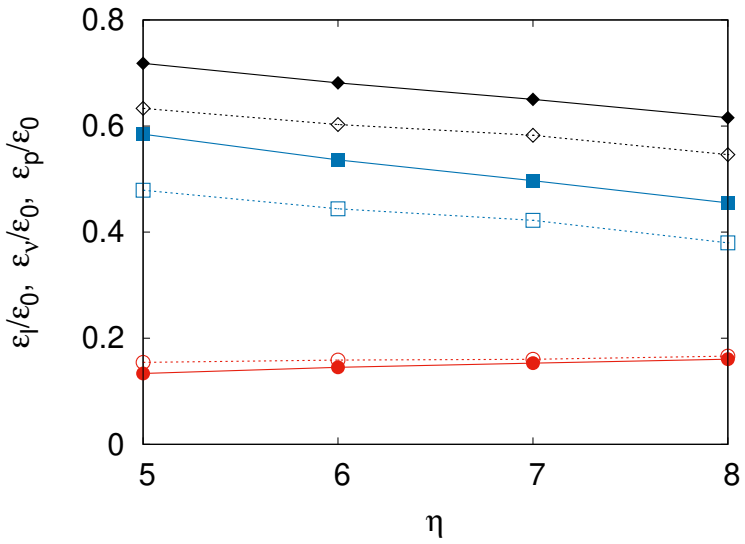


**Figure 5.7:** Mean values of energy input $\varepsilon_I$ (black diamonds), viscous dissipation $\varepsilon_\nu$ (blue squares) and polymer dissipation $\varepsilon_p$ (red circles), as function of $\eta$. Filled symbols are for the three-dimensional DNS, empty ones are for the two-dimensional DNS.

In the statistical stationary state, averaging over sufficiently long times, the energy can be assumed constant, and therefore the energy balance reduces to $\varepsilon_I = \varepsilon_\nu + \varepsilon_p$. These quantities are displayed in Fig. 5.7, normalized with the mean energy input of the laminar flow $\varepsilon_0 = FU_0/2$. We

can observe a slight increase in the polymer dissipation as the concentration coefficient increases, but the main effect of polymers appears to be a suppression of the energy input provided by the constant forcing, as a consequence of the reduction of the mean flow amplitude. This result is consistent with the data plotted in Fig. 5.1, showing that kinetic energy is reduced at increasing polymer concentration. Figure 5.7 indicates that for all values of $\eta$, energy is mostly dissipated by viscosity. Therefore we expect that the small scale properties of the flow are weakly affected by the polymer concentration.

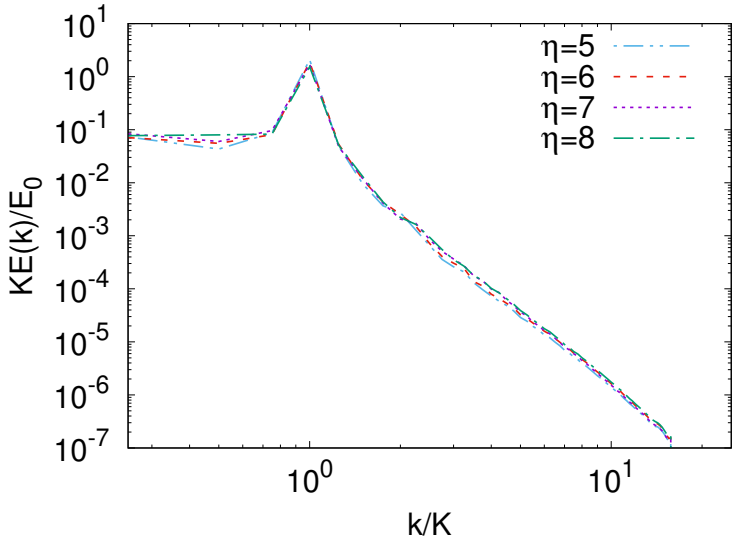


**Figure 5.8:** Time averaged, kinetic energy spectra as a function of wavenumber from 3D simulations with different values of $\eta$.

In order to investigate in details this point, in Fig. 5.8 we plot the kinetic energy spectra in stationary conditions and for the different values of concentration. Note the peak of the spectra at the forcing wavenumber $K$ (the only active wavenumber in the laminar case). We observe very small variations of the spectrum with $\eta$, mostly concentrated at small wavenumbers (since the total energy changes with $\eta$). At large wavenumbers the spectra shows a power law behaviour $E(k) \sim k^{-\alpha}$ with $\alpha \simeq 4.8$, which indicates the presence of fluctuations at all scales. The fact that the power spectrum is steeper than $k^{-3}$ indicates that the ve-

locity field is smooth in this regime, similarly to what observed in elastic turbulence [55, 58].

### 5.3.4 Mixing properties

Since we noted the presence of velocity fluctuations over a wide range of spatial scales, we expect that this fact causes a strong influence on the mixing efficiency of the flow. In order to address this point we investigated the mixing of a passive scalar by simultaneously integrating equation for a scalar field $\theta(\boldsymbol{x}, t)$ transported by the velocity field $\boldsymbol{u}$ obtained from Eqs. (5.1)

$$\partial_t \theta + u_k \partial_k \theta = D \partial^2 \theta \tag{5.8}$$

where $D$ is the molecular diffusivity, which we set to $D = 2 \times 10^{-3}$ in all the simulations. The integration of the Equation (5.8), obtained with the same pseudo-spectral method discussed in Appendix A, starts at an arbitrary time in the stationary regime of chaotic flow. We considered a monochromatic initial condition for $\theta$, having the same periodicity of the mean flow $\theta(\boldsymbol{x}, 0) = \theta_0 \cos(Kz)$. With this initial condition, in absence of polymers, the mixing is due exclusively to molecular diffusion, since the gradients of the scalar field $\nabla\theta$ are orthogonal to the laminar velocity field. In particular, for $\eta = 0$ the variance of the scalar field (as well as the variance of its gradients) decays exponentially as $\langle\theta^2\rangle \propto \langle(\nabla\theta)^2\rangle \propto \exp(-\beta_0 t)$, with $\beta_0 = 2DK^2$.

The presence of polymers causes a strong enhancement of the mixing, which is illustrated by the vertical sections of $\theta$ fields displayed in Fig.5.9. At variance with the diffusive case at $\eta = 0$ in which the scalar field remains monochromatic, here we observe the formation of thin scalar filaments, which rapidly transfer the scalar fluctuations to small dissipative scales, ultimately leading to a strong enhancement in the mixing efficiency.

A quantitative evaluation of the mixing properties is provided by the temporal evolution of the variance of $\theta$ and $\nabla\theta$ shown in Figure 5.10. Here and in the following, the results presented are averaged over 13 independent simulations of Equation (5.8), starting from the same initial

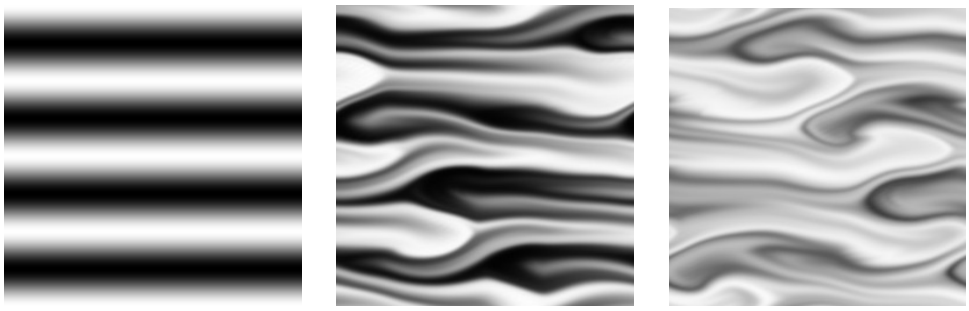

**Figure 5.9:** Vertical section in the $x-z$ plane at fixed $y=0$ of the scalar field $\theta$ for the 3D simulation with $\eta=8$ at different times. From left to right: $t=0$, $t=32T_0$, $t=64T_0$.

condition $\theta(\boldsymbol{x},0)$ and different velocity fields. The decay of $\langle\theta^2\rangle$ in the chaotic regime induced by the polymers is much faster with respect to the case $\eta=0$. We can observe the same result for the long-time decay of the variance of scalar gradients $\langle(\nabla\theta)^2\rangle$, even though the chaotic advection of the scalar field causes an initial increase of its gradients (this effect is clearly seen in Fig 5.9). For the concentration values considered in our study, we are not able to observe a clear dependence of the mixing efficiency on $\eta$.

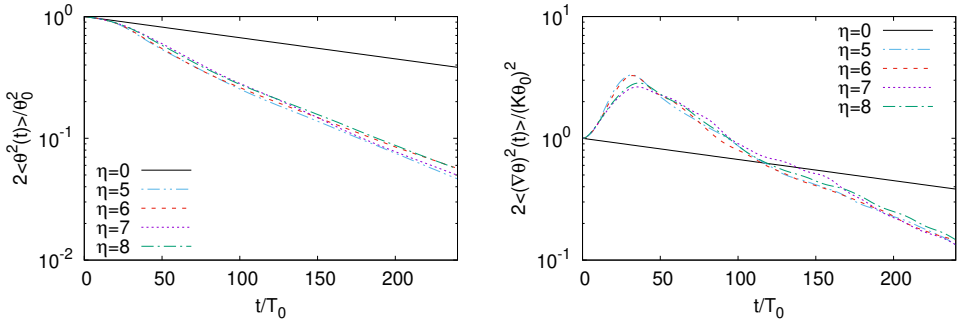


**Figure 5.10:** Decay of the variance of the scalar field $\langle\theta^2\rangle$ (left panel) and of the scalar gradients $\langle\nabla\theta)^2\rangle$ (right panel) for the different values of $\eta$ in 3D simulations. Solid black line represents the diffusive exponential decay in absence of polymers.

The instantaneous exponential decay rate of the scalar variance $\beta_p = -\frac{d}{dt}\log\langle\theta^2\rangle$ can be expressed, using (5.8), as

$$\beta_p(t) = -\frac{d}{dt}\log\langle\theta^2\rangle = 2D\frac{\langle(\nabla\theta)^2\rangle}{\langle\theta^2\rangle} \tag{5.9}$$

which can be directly compared with the decay rate due to molecular

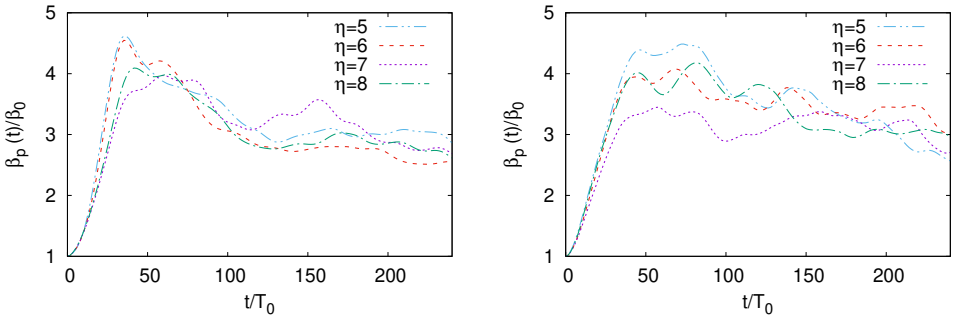


**Figure 5.11:** Instantaneous exponential decay rate $\beta_p(t)$ for different values of $\eta$ in 3D simulations (left panel) and 2D simulations (right panel).

diffusion $\beta_0 = 2DK^2$.

The decay rate $\beta_p$ reaches a maximum value after a very short time, corresponding to the maximum development of thin filaments of the scalar field. At longer time, since both $\langle\theta^2\rangle$ and $\langle(\nabla\theta)^2\rangle$ decay exponentially, $\beta_p$ approaches an almost constant value, about three times larger than $\beta_0$ (see Fig. 5.11) which gives us a good quantification of the increased mixing efficiency. We note that the ratio $\beta_p/\beta_0$ is proportional to the square of the ratio between the large scale of the scalar field $1/K$ and the typical scale of its gradients $(\langle\theta^2\rangle/\langle(\nabla\theta)^2\rangle)^{1/2}$.

### 5.3.5 Comparison between 2D and 3D

According the results presented so far, we can assert that the properties of the chaotic flow, which is obtained from 3D numerical simulations of the model (5.1) for a dilute solution of rigid rods, are qualitatively similar to those reported in previous numerical studies in 2D domains [70, 71]. In particular, we observed that the fluctuations of the $y$-component of the velocity $u_y$, which is transverse both to the streamwise direction of the mean flow $x$ and to the direction of its gradient $z$, remain considerably smaller than those of $u_x$ and $u_z$ (see Figure 5.4). This confirms that the dynamics of the three-dimensional system is substantially two-dimensional, and that the properties of the chaotic flow are qualitatively independent on its dimensionality.

In order to perform a qualitative comparison between the properties of the 3D and 2D flows, we also performed a new set of 2D simulations of the system of equations (5.1) with the same parameters of the 3D simulations. The comparison of the mean flow and velocity fluctuations, reported in Figure 5.12, clearly shows that the effects of polymers are more pronounced in 2D than in 3D. Keeping fixed the value of the polymer concentration $\eta$, we notice that the velocity fluctuations are more intense in 2D than in 3D. Similarly, the reduction of the amplitude $U$ of the mean flow, with respect to the laminar solution $U_0$, is stronger in 2D than in 3D. It is worth to notice that 2D and 3D curves of $U$ and $u'$, as a function of $\eta$, appear to be almost parallel, which is an indication of the fact that the effect of dimensionality is systematic and not dependent on $\eta$.

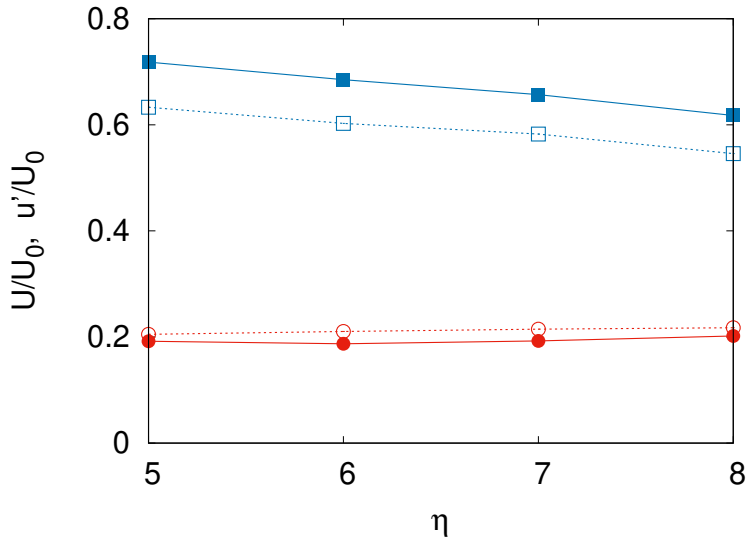


**Figure 5.12:** Amplitudes of mean velocity profiles $U$ (blue squares) and rms velocity fluctuations $u'_{rms}$ (red circles) as a function of $\eta$ in 3D (filled symbol) and 2D (empty symbols) simulations.

In Figure 5.5 we report the comparison of the momentum balance. Also in this case we observe that the values of the friction factor in 2D are systematically higher than in 3D at fixed $\eta$. In both cases, the enhancement of the drag is mostly due to the increase of the polymer stress, with a subdominant contribution due to the increase of the viscous Newtonian stress. The combined effect of increased friction factor and reduced

Reynolds number can be observed in Figure 5.6, where the deviation from the Newtonian point $f = 1$ is stronger for the 2D simulations. Considering the energy balance, the reduction of the amplitude of the mean flow causes a reduction of the energy injection rate $\varepsilon_I$ in 2D simulations with respect to the 3D ones at fixed $\eta$ (see Figure 5.7). This phenomenon is balanced by a reduction of the viscous dissipation rate $\varepsilon_\nu$, while the energy dissipation due to polymers remains almost unchanged.

In summary, we can conclude that the effects of rod-like polymers in viscous flows in three-dimensions is significantly weaker than in two-dimensions. We believe that the origin of this difference can be probably attributed to the different rotational degrees of freedom of the rods. In 2D, the rotation of the polymers can occur only in the $x - z$ plane, implying that, during the rotation, the $R_{zz}$ component of the conformation tensor is non-zero, and therefore the polymers are oriented in the direction of the gradient of the mean flow (the $z$-direction). Conversely, in 3D they can rotate also in the $x - y$ plane, indeed in the stationary regime the average values of $R_{yy}$ and $R_{zz}$ appear to be very similar, but the polymer rotations in the $x - z$ and $x - y$ planes have very different consequences on the polymer stress tensor $\sigma_{ij}$. We remind that $\sigma_{ij}$ is proportional to the product of the configuration tensor $R_{ij}$ and the velocity gradient tensor $\partial_i u_j$. In the case of the laminar Kolmogorov flow $\boldsymbol{u}(\boldsymbol{x}) = (U_0 \cos(Kz), 0, 0)$, the only component of the velocity gradient which is non-zero is $\partial_z u_x$. As a consequence, there is no stress induced by rotations in the $x-y$ plane (which is allowed only in 3D). This means that in the case of the chaotic flow, the gradients of velocity in the $y$-direction originates are due only to the fluctuating part of the velocity field, and therefore they are significantly smaller than those in the $z$-direction. As a result, the polymer stress in 3D is on average weaker than in 2D flow with the same $\eta$.

We obtained an heuristic estimate of the dimensional dependence of the average polymer stress, considering the formal expression of the stress tensor in $d$-dimensions [24] $\sigma_{ij} = 2d\nu\eta R_{ij}(\partial_l u_k)R_{kl}$, which is derived under the assumption of isotropy of the conformation tensor $R_{ij} = \delta_{ij}/d$ in

the limit of zero shear. Even though this hypothesis is not fulfilled in the case of the Kolmogorov flow, since the non-vanishing mean shear induces a preferential alignment of the rods in the direction of the mean flow, we can suppose that simulations in 2D and 3D can be simply mapped by rescaling the polymer concentration as $\eta^{2D} = (2/3)\eta^{3D}$. We tested this prediction by comparing two simulations in 2D, with reduced parameters $\eta^{2D} = 4$ and $\eta^{2D} = 5.33$, with the corresponding simulations in 3D with $\eta^{3D} = 6$ and $\eta^{3D} = 8$. In both cases, we noticed that the rescaling of the concentration reduces the difference between the amplitude of the mean flow in 2D and 3D below 3%. Therefore, although the rescaling is not exact, it still provides a simple and useful empirical rule to translate 2D results for 3D applications, at least for this flow. This mapping also supports the interpretation of the dimensional effects reported in our study in terms of the different rotational degrees of freedom of the rods.

Finally we compare the mixing properties of 2D and 3D flows by integrating the transport equation (5.8) for a two-dimensional scalar field $\theta$ transported by the 2D flow. Initial conditions and diffusion coefficient are identical to those of 3D simulations. In Figure 5.11 we show the temporal trends of the instantaneous exponential decay rate $\beta_p(t)$ obtained in the 2D simulations, which appear to be very similar to those obtained in 3D simulations: this is in agreement with the observation that the intensity of velocity fluctuations, which causes the mixing, is very similar as well (see Fig. 5.12).

# Chapter 6

# Multi-scale stability analysis

In order to better understand the transition from laminar to chaotic regime at low Reynolds number, we tried to perform a linear stability analysis of the Kolmogorov flow with rigid rod-like polymers. In particular, we considered a multiple-scale analysis [114, 115] similar to the one that was adopted for the same flow with flexible polymers. [100] Our starting point is the Squire's theorem, [104] which states that for parallel flows the most unstable perturbations are two-dimensional. This allows us to disregard the neutral direction: $x$ will be the flow direction, and $y$ the shear one.

Writing again the equations of the Doi-Edwards model: [24]

$$\partial_i u_i = 0, \tag{6.1a}$$

$$\partial_t u_i + u_j \partial_j u_i = -\partial_i p + \nu \nabla^2 u_i - 6\eta\nu \partial_j R_{ij} \left( R_{kl} \partial_l u_k \right) + f_i, \tag{6.1b}$$

$$\partial_t R_{ij} + u_k \partial_k R_{ij} = R_{kj} \partial_k u_i + R_{ik} \partial_k u_j - 2 R_{ij} \left( R_{kl} \partial_l u_k \right), \tag{6.1c}$$

we can combine the incompressibility condition with the equation for the velocity field, in order to obtain an equation for the pressure field:

$$\nabla^2 p + \partial_i u_j \partial_j u_i - 6\eta\nu \partial_i \partial_j R_{ij} \left( R_{kl} \partial_l u_k \right) = 0. \tag{6.2}$$

Assuming a cosinusoidal forcing $f_x = F \cos(Ky)$, the laminar solution is:

$$u_x = U \cos\left(Ky\right), \quad u_y = 0, \quad p = 0, \quad R_{xx} = 1, \quad R_{xy} = 0, \qquad R_{yy} = 0. \tag{6.3}$$

In order to have a simpler notation, we call $u_x = u$ and $u_y = v$, and we apply a generic perturbation to the system (assuming $u' \ll U$ and $R'_{xx} \ll 1$):

$$u = U\cos(Ky) + u', \qquad v = v', \qquad p = p',$$
$$R_{xx} = 1 + R'_{xx}, \qquad R_{xy} = R'_{xy}, \qquad R_{yy} = R'_{yy}. \tag{6.4}$$

All the perturbations have to respect the periodicity of the base flow, in order to be physically acceptable. Substituting (6.4) into (6.1), and keeping only linear terms in the perturbations, we have the six linearised equations:

$$\partial_t u' + U\cos(Ky)\partial_x u' - UK\sin(Ky)v' + \partial_x p'$$
$$-\nu\nabla^2 u - 6\eta\nu\partial_x\left(\partial_x u' - UK\sin(Ky)R'_{xy}\right) = 0 \tag{6.5a}$$

$$\partial_t v' + U\cos(Ky)\partial_x v' + \partial_y p' - \nu\nabla^2 v = 0 \tag{6.5b}$$

$$\nabla^2 p' - 2UK\sin(Ky)\partial_x v' - 6\eta\nu\partial_x^2\left(\partial_x u' - UK\sin(Ky)R'_{xy}\right) \tag{6.5c}$$

$$\partial_t R'_{xx} + U\cos(Ky)\partial_x R'_{xx} = 0, \tag{6.5d}$$

$$\partial_t R'_{xy} + U\cos(Ky)\partial_x R'_{xy} + UK\sin(Ky)R'_{yy} - \partial_x v' = 0, \tag{6.5e}$$

$$\partial_t R'_{yy} + U\cos(Ky)\partial_x R'_{yy} = 0. \tag{6.5f}$$

We can see that the $R'_{xx}$ component does not influence the other quantities, so we disregard its equation. $R'_{yy}$ instead appears also in the equation for $R'_{xy}$, but, from physical consideration, we can consider $R'_{yy}$ as a second-order perturbation, since the tensor $R_{ij}$ is quadratic in the perturbation of the director $n_i$. For this reason we also set $R'_{yy} = 0$.

At this point, further assumptions simplify our computation. We choose to consider only large-scale perturbations (in the Newtonian situation, it can be demonstrated that the flow is always linearly stable for small-scale perturbations), for which we expect that perturbation evolves on time scales much larger than base flow typical time scale. Moreover, we expect a diffusive behaviour at large scales, which implies a quadratic relationship between space and time.

The core idea of the multiple scale analysis is therefore to consider the variables related to the base flow (*fast* variables) as independent from the

variables related to the perturbation evolution (*slow* variables). Therefore this method can work only if there is a clear separation between scales of base flow and perturbation, otherwise it can give wrong predictions.

If we denote as $\epsilon$ the ratio between small and large spatial scale (separation between scales therefore implies $\epsilon \ll 1$), we define the slow variables as $X = \epsilon x$, $Y = \epsilon y$, $T = \epsilon^2 t$, which implies that differential operators will become:

$$\partial_x \to \partial_x + \epsilon\partial_X, \quad \partial_y \to \partial_y + \epsilon\partial_Y, \quad \partial_t \to \partial_t + \epsilon^2\partial_T. \tag{6.6}$$

The fact that the base flow does not depend on $t$ and $x$ allows us to disregard the $\partial_x$ and $\partial_t$ terms, and the Laplacian operator will have this form:

$$\nabla^2 \to \partial_y^2 + 2\epsilon\partial_y\partial_Y + \epsilon^2(\partial_X^2 + \partial_Y^2). \tag{6.7}$$

In order to further simplify the notation, we rename $R'_{xy} = R'$. We make another assumption: we consider only transverse perturbations (which are the most unstable in the Newtonian case), so we can neglect also the slow variable $Y$, and the equation for $u'$, since $u'$ does not appear into the other equations. With this hypothesis we expand the perturbations in terms of $\epsilon$:

$$p' = p_0(y, X, T) + \epsilon p_1(y, X, T) + \epsilon^2 p_2\,(y, X, T) + ..., \tag{6.8a}$$

$$v' = v_0(y, X, T) + \epsilon v_1(y, X, T) + \epsilon^2 v_2\,(y, X, T) + ..., \tag{6.8b}$$

$$R' = R_0(y, X, T) + \epsilon R_1(y, X, T) + \epsilon^2 R_2\,(y, X, T) + ..., \tag{6.8c}$$

and we substitute the perturbation into the linearised equations (6.5), until the second order in $\epsilon$:

$$\begin{aligned}\epsilon^2\partial_T v_0 + \epsilon U\cos(Ky)\partial_X(v_0 + \epsilon v_1) + \partial_y(p_0 + \epsilon p_1 + \epsilon^2 p_2)\\ -\nu(\epsilon^2\partial_X^2 + \partial_y^2)(v_0 + \epsilon v_1 + \epsilon^2 v_2) = 0,\end{aligned} \tag{6.9a}$$

$$\begin{aligned}(\epsilon^2\partial_X^2 + \partial_y^2)(p_0 + \epsilon p_1 + \epsilon^2 p_2) - 2UK\epsilon\sin(Ky)\partial_X(v_0 + \epsilon v_1)\\ -6\eta\nu\epsilon^2 UK\sin(Ky)\partial_X^2 R_0 = 0,\end{aligned} \tag{6.9b}$$

$$\epsilon^2\partial_T R_0 + \epsilon U\cos(Ky)\partial_X(R_0 + \epsilon R_1) - \epsilon\partial_X(v_0 + \epsilon v_1 + \epsilon^2 v_2 + ...) = 0. \tag{6.9c}$$

Now, we can analyse the terms having the same dependence on $\epsilon$.

**Zero-th order**

$$\partial_y p_0 - \nu \partial_y^2 v_0 = 0 \tag{6.10a}$$
$$\partial_y^2 p_0 = 0 \tag{6.10b}$$
$$0 = 0 \tag{6.10c}$$

We do not have any information about $R_0$, while $p_0$ can not depend on $y$. Although a linear dependence of $p_0$ on $y$ would be admitted by $\partial_y^2 p_0 = 0$, it would violate the periodicity of the system. For the same reason, also $v_0$ can not depend on $y$:

$$p_0 = c_0(X,T), \qquad v_0 = b_0(X,T), \qquad R_0 = R_0(y,X,T). \tag{6.11}$$

**First order**

$$UK\cos(Ky)\partial_X v_0 + \partial_y p_1 - \nu \partial_y^2 v_1 = 0 \tag{6.12a}$$
$$\partial_y^2 p_1 - 2UK\sin(Ky)\partial_X v_0 = 0 \tag{6.12b}$$
$$U\cos(Ky)\partial_X R_0 - \partial_X v_0 = 0 \tag{6.12c}$$

From the second equation we obtain $p_1$:

$$p_1 = c_1(X,T) - \frac{2U}{K}\sin(Ky)\partial_X b_0, \tag{6.13}$$

and we substituted it into the first one, so we have $v_1$:

$$v_1 = b_1(X,T) + \frac{U}{\nu K^2}\cos(Ky)\partial_X b_0. \tag{6.14}$$

From the third one we instead obtain informations about $R_0$:

$$\partial_X R_0 = \frac{\partial_X b_0}{U\cos(Ky)}, \qquad \Rightarrow \qquad R_0 = \frac{b_0}{U\cos(Ky)} + r_0(y,T). \tag{6.15}$$

**Second order**

$$\partial_T v_0 + U\cos(Ky)\partial_X v_1 + \partial_y p_2 - \nu\partial_y^2 v_2 - \nu\partial_X^2 v_0 = 0, \tag{6.16a}$$
$$\partial_y^2 p_2 + \partial_X^2 p_0 - 2UK\sin(Ky)\partial_X v_1 - 6\eta\nu UK\sin(Ky)\partial_X^2 R_0 = 0, \tag{6.16b}$$
$$\partial_T R_0 + U\cos(Ky)\partial_X R_1 - \partial_X v_1 = 0. \tag{6.16c}$$

In the second equation, we substitute $v_1$ and $\partial_X R_0$ using the information we have from the first order:

$$\partial_y^2 p_2 = \partial_X^2 c_0 + 2UK\sin(Ky)\partial_X b_1 + 2\frac{U^2}{\nu K}\sin(Ky)\cos(Ky)\partial_X^2 b_0 \\ +6\eta\nu K\tan(Ky)\partial_X^2 b_0, \quad (6.17)$$

and we integrate, in order to obtain $\partial_y p_2$:

$$\partial_y p_2 = -2U\cos(Ky)\partial_X b_1 - \frac{U^2}{2\nu K^2}\cos(2Ky)\partial_X^2 b_0 - 6\eta\nu(\ln|\cos(Ky)|)\partial_X^2 b_0 \quad (6.18)$$

where, in order to not violate the periodicity, we set $\partial_X c_0 = 0$. If we substitute $\partial_y p_2$, $v_0$ and $v_1$ into the first equation, we get:

$$\partial_T b_0 - U\cos(Ky)\partial_X b_1 + \frac{U^2}{\nu K^2}\cos^2(Ky)\partial_X^2 b_0 - \frac{U^2}{2\nu K^2}\cos(2Ky)\partial_X^2 b_0 - \\ -6\eta\nu(\ln|\cos(Ky)|)\partial_X^2 b_0 - \nu\partial_y^2 v_2 - \nu\partial_X^2 b_0 = 0 \quad (6.19)$$

Similarly to the study in [100], at this point we average on the period in the $y$ direction. Since we know that:

$$\frac{1}{2\pi}\int_0^{2\pi}\cos(x)dx = 0, \qquad \frac{1}{2\pi}\int_0^{2\pi}\cos^2(x)dx = \frac{1}{2}, \\ \frac{1}{2\pi}\int_0^{2\pi}\ln|\cos(x)|dx = -\ln 2, \qquad \frac{1}{2\pi}\int_0^{2\pi}\cos(2x)dx = 0, \quad (6.20)$$

we obtain a relationship about the temporal evolution of the perturbation $b_0$ (in the Kolmogorov flow, $U/(\nu K^2)$ is an alternative expression of the Reynolds number):

$$\partial_T b_0 = \nu\left(1 - \frac{1}{2}Re^2 - 6\ln(2)\eta\right)\partial_X^2 b_0. \quad (6.21)$$

Hence, the flow is stable if:

$$1 - \frac{1}{2}Re^2 - 6\ln(2)\eta \geq 0, \quad (6.22)$$

corresponding to a critical Reynolds number:

$$\boxed{Re_c = \sqrt{2}\sqrt{1 - 6\eta\ln 2}}. \quad (6.23)$$

In absence of polymers ($\eta = 0$) we recover the Newtonian value $Re_c = \sqrt{2}$. Unfortunately, our numerical simulations do not agree with the prediction at $\eta > 0$, implying that some of our hypothesis, for example the scale separation, are not valid in the context of Kolmogorov flow with rod-like polymers.

# Chapter 7

# Turbulent flows at high-Reynolds number

As it has been described in chapter 2, turbulent flows are affected by small amounts of flexible polymers, in particular we can observe a strong reduction of the hydrodynamic drag. [22, 25] This behaviour has been extensively investigated in pipe and channel flows, but, in order to obtain a clearer picture of the effect of flexible polymers, also in homogenous turbulence, [47, 48, 116] in thermal convection, [50, 51] and in a shear flow without walls (the Kolmogorov flow). [46] In particular, in the Kolmogorov flow, it was observed an increase of the mean velocity profile, corresponding to drag reduction also in absence of walls. On the contrary, despite also rigid rod-like polymers alter wall-bounded flows in a similar way, [39, 41] no analogous studies have been performed so far on the effect of rigid polymers in absence of walls. For this reason, we performed a study of the Kolmogorov flow with rod-like polymers at high-Reynolds numbers, and we found that, differently from the case with flexible polymers, in absence of walls rigid polymers cause the suppression of turbulent fluctuations without a corresponding increase of mean flow, which instead appears slightly reduced.

## 7.1 Model and simulations

A dilute solution of rigid rod-like polymers can be described using the Doi-Edwards model [24]:

$$\partial_t u_i + u_k \partial_k u_i = -\partial_i p + \nu \partial^2 u_i + \partial_k \sigma_{ik} + f_i, \tag{7.1a}$$

$$\partial_t R_{ij} + u_k \partial_k R_{ij} = (\partial_k u_i) R_{kj} + R_{ik}(\partial_k u_j) - 2R_{ij}(\partial_l u_k) R_{kl}, \tag{7.1b}$$

where $\boldsymbol{u}(\boldsymbol{x}, t)$ is the incompressible ($\partial_i u_i = 0$) velocity field, $\boldsymbol{R}(\boldsymbol{x}, t)$ the polymer configuration tensor, $p(\boldsymbol{x}, t)$ the kinematic pressure, $\nu$ the kinematic viscosity, $\boldsymbol{f}(\boldsymbol{x}, t)$ the external forcing, and $\sigma_{ij} = 6\nu\eta R_{ij}(\partial_l u_k) R_{kl}$ the polymer stress tensor (more details in chapter 3). Additional terms regarding Brownian rotations can be safely disregarded in turbulent flows, since their characteristic time is very much greater than the large eddy turnover time of the flow. In order for equations (7.1) to be valid, the polymer length has to be significantly smaller than the Kolmogorov length of the flow. Both the conditions are easily met by commercial available rigid-rod like polymers. [110] $\boldsymbol{f}(\boldsymbol{x}) = (F\cos(Kz), 0, 0)$ is the Kolmogorov forcing, where $F$ is the amplitude and $K$ is the wavenumber. It induces a monochromatic mean flow, $\langle u_x \rangle = U\cos(Kz)$, where $U = F/(\nu K^2)$ in the laminar regime. A quantitative investigation of the relationship between $F$ and $U$ (and therefore the Reynolds number $Re = U/(\nu K)$) in the Newtonian turbulent regime has been presented in [86].

We integrated equations (7.1) in a cubic periodic domain of size $L = 2\pi$ discretized on a regular grid of $N^3 = 256^3$ gridpoints, using a pseudospectral code with 1/2 dealising, due to the cubic nonlinearities. [111] Time integration is performed with a 4th order Runge-Kutte scheme, [112] with an implicit integration of linear dissipative terms. A diffusive term $\kappa\partial^2 R_{ij}$ has been added to eq. (7.1b) in order to improve numerical stability. [113] More details on numerical methods are provided in Appendix A

We set $\nu = \kappa = 10^{-3}$ and $K = 1$. We performed a total of four different simulations: two with $F = 0.016$ and two with $F = 0.032$, which, combined with the other parameters we choose, in the Newtonian turbulent regime correspond respectively to $Re \approx 340$ and $Re \approx 480$.

[86] For every value of forcing, we performed one simulation without polymers ($\eta = 0$) and another one with $\eta = 6$. In order to have a coherent comparison, also Newtonian simulations are subjected to 1/2 dealiasing.

## 7.2 Results and discussions

Our simulations confirms the monochromaticity of the turbulent Kolmogorov flow, both with polymers and without. Decomposing the velocity field into a a mean component and fluctuations:

$$\boldsymbol{u}(\boldsymbol{x}) = U(\cos(Kz), 0, 0) + \boldsymbol{u}'(\boldsymbol{x}) \tag{7.2}$$

we can compare the amplitude of mean velocity profiles, with or without polymers, for the two different forcing we considered.

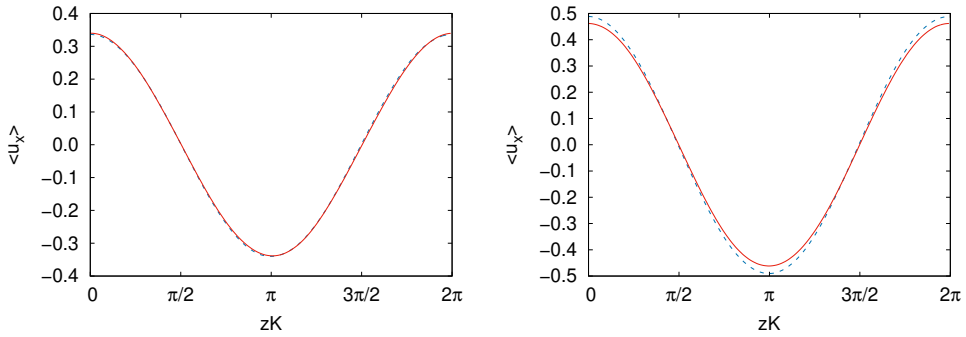


**Figure 7.1:** Mean velocity profiles for $F = 0.016$ (left) and $F = 0.032$ (right). Red solid lines correpond to $\eta = 6$, blue dashed line to $\eta = 0$.

Profiles in fig. 7.1 clearly indicate that rigid polymers do not cause an increase of the mean flow: at $Re \approx 340$ the flow appears to be unchanged, while at $Re \approx 480$ we can even observe a decrease, hence some form of drag enhancement. It is a very different situation from the one in wall bounded flows, where it is well known that also rod-like polymers cause drag reduction, and from flexible polymers, which in an analogous setting cause an increase of the mean flow. If we compute the friction factor, which in Kolmogorov flow assumes the form $f = F/(KU^2)$, we have indeed, respectively for the flow without or with the polymers, $f = 0.1399$

vs $f = 0.1402$ at $Re \approx 340$, and $f = 0.1323$ vs $f = 0.1479$ at $Re \approx 480$. We recall that, asymptotically, in the Newtonian turbulent regime we have $f \propto Re^{-1}$. [86]

Other informations about the flows can be obtained from the velocity fluctuations $\boldsymbol{u}'$. We observe that the root-mean-squared (rms) values of the fluctuation velocity field, in all the three directions, are significantly reduced in the flow with the polymers compared with the Newtonian one (see Table 7.1). This fact suggests that the rodlike polymers inhibit the turbulent motion.

| $\eta$ | F | $f$ | U | $u'_x$ | $u'_y$ | $u'_z$ | $10^3\varepsilon_I$ | $10^3\varepsilon_\nu$ | $10^3\varepsilon_p$ |
|---|---|---|---|---|---|---|---|---|---|
| 0 | 0.016 | 0.1399 | 0.338 | 0.181 | 0.149 | 0.164 | 2.70 | 2.71 | - |
| 6 | 0.016 | 0.1402 | 0.338 | 0.174 | 0.136 | 0.148 | 2.69 | 1.24 | 1.45 |
| 0 | 0.032 | 0.1323 | 0.492 | 0.254 | 0.215 | 0.250 | 7.88 | 7.88 | - |
| 6 | 0.032 | 0.1479 | 0.465 | 0.241 | 0.200 | 0.227 | 7.40 | 3.36 | 4.04 |

**Table 7.1:** Parameters of the simulations: $F$ amplitude of the forcing, $f$ friction factor, $U$ amplitude of the mean flow, $u'_x, u'_y$ and $u'_z$ rms value of the velocity fluctuations, $\varepsilon_I$ mean energy input, $\varepsilon_\nu$ mean viscous dissipation and $\varepsilon_p$ mean polymer dissipation.

This hypothesis is confirmed by energy spectra. In particular fig. 7.2 clearly shows that the small-scale motion is strongly suppressed by polymers, while at large scales the spectra appear to be almost unchanged.

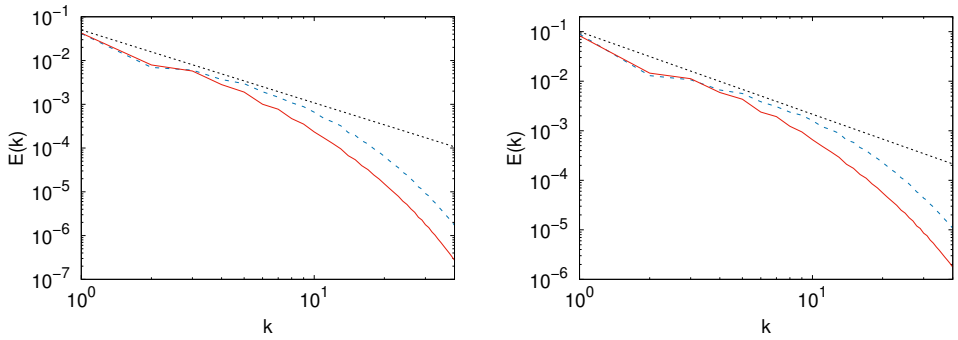


**Figure 7.2:** Mean kinetic energy spectra for $F = 0.016$ (left) and $F = 0.032$ (right). Red solid lines correponds to $\eta = 6$, blue dashed line to $\eta = 0$. Pointed black line represents the $\propto k^{-5/3}$ Kolmogorov's law.

The small-scale behaviour we see is compatible with spectra observed in a very recent experimental work about drag reduction in pipe flow, [117]

where a $\propto k^{-3}$ law was proposed for inertial range in flows with polymers. In our simulations, the inertial range is probably too small to evaluate the power-law behaviour, but it still appears to be compatible to the observations in [117]. However, the large scale behaviour is obviously different, since in [117] the phenomenon of drag reduction is observed.

A different small-scale behaviour in spectra, between the Newtonian and the non-Newtonian flows, means that dissipation is strongly affected by polymers. The total energy budget in our system is:

$$\frac{d}{dt}\langle E\rangle = \varepsilon_I - \varepsilon_\nu - \varepsilon_p, \tag{7.3}$$

where $\varepsilon_I = \langle \boldsymbol{f}\cdot\boldsymbol{u}\rangle = FU/2$ is the mean energy input, $\varepsilon_\nu = \langle \nu\,|\nabla\boldsymbol{u}|^2\rangle$ the mean dissipation rate due to Newtonian viscosity, and $\varepsilon_p = \langle \sigma_{ij}\partial_j u_i\rangle$ the one due to polymers. If we average over a sufficient long time, the total energy can be considered constant, and so we have $\varepsilon_I = \varepsilon_\nu + \varepsilon_p$. The values we obtained (Table 7.1) confirm that the dissipation is strongly affected by polymers, since in the non-Newtonian case more than half of the energy is dissipated by the polymer stress.

In order to explain the difference between our simulations without walls, and the ones in channel flows (and the experiments) where drag reduction is observed, we can consider the momentum budget. Averaging the Eq. (7.1a) over $x, y$ and time, we have

$$\partial_z \Pi_r = \partial_z\left(\Pi_\nu + \Pi_p\right) + f_x, \tag{7.4}$$

where $\Pi_\nu = \nu\partial_z\overline{u_x}$ the viscous Newtonian stress, $\Pi_p = \overline{\sigma_{xz}}$ the polymer non-Newtonian stress and $\Pi_r = \overline{u_x u_z}$ is the Reynolds stress. In the case of Kolmogorov flow we have that all these quantities have a sinusoidal profile:

$$\begin{aligned} \Pi_\nu = \nu\partial_z\overline{u_x} = -KU\sin(Kz), \qquad \Pi_p = \overline{\sigma_{xz}} = -\Sigma\sin(Kz), \\ \Pi_r = \overline{u_x u_z} = -S\sin(Kz). \end{aligned} \tag{7.5}$$

This fact means that, if we consider the average profile, not only the mean Newtonian stress $\Pi_\nu$ is proportional to the mean shear rate $\partial_z u_x$ (which is trivially the definition of Newtonian fluid), but that also the

(which, instead, is not trivial) mean polymer stress $\Pi_p$ is proportional to the mean shear rate: this means that, for the mean flow, the fluid remains Newtonian, with a modified value of the viscosity. This is a very different situation from wall-bounded flows, where the theory predicts a non-uniform effective polymer viscosity, [39, 41] confirmed by recent experiments [30] which observed a "near-wall lubricating layer", *i.e.* a very small effective viscosity near the walls. This is probably related also to the fact that in bounded flows polymers appear to be strongly aligned with the mean flow near the walls, [41,110] *i.e.* $\overline{R_{xx}} \approx 1 \gg \overline{R_{yy}}, \overline{R_{zz}}$, while in our simulations we have everywhere $\overline{R_{xx}} \lesssim 0.4$ and $\overline{R_{yy}}, \overline{R_{zz}} \gtrsim 0.3$, a situation that in bounded flows is observed far from the boundaries, in the turbulent bulk.

The absence of drag reduction we observed is therefore probably due with the absence of the lubricating layer, induced by the strong alignment of polymers, caused by solid walls. It is important to remark that the effective Newtonian behaviour we observed is valid at large scales in the mean flow, but not for the fluctuating small scale motion, where we can not assume a constant effective viscosity. This fact is confirmed by the energy spectra (and partially by the rms values of velocity fluctuations, which take in account both large-scale and small-scale turbulent motion), which reveal important qualitative differences between the flows with and without polymers. The similarities between the large wavenumbers behaviour of our spectra, and experimental spectra from [117], can be instead explained by the fact that we expect the small scale turbulent motion to be less influenced by walls.

# Part II

# Dense bacterial suspensions

# Chapter 8

# Introduction to active fluids

An important chapter of statistical physics of these last decades is the study of active matter. It can be defined as an out-of-equilibrium system composed by a certain number of constituent elements, which convert some forms of external energy (for example, chemical energy) into some forms of motion or forces. The crucial difference with other forms of out-of-equilibrium systems is that the energy is injected individually by every individual entity, thus breaking the time-reversal symmetry at local scale. [118] As a comparison, also the inertial turbulence in fluids is a out-of-equilibrium phenomenon, but it is generated by an external forcing acting globally, or at the boundaries of the domain. For this reason, the study of active matter has attracted the interest of scientists from very different research fields, as a paradigm of a novel class of out-of-equilibrium phenomena. [119]

Examples of active matter in nature go from human crowds [120] and bird flocks [121] to fish schools, [122] from microswimmers suspensions [123] to epithelial tissues [124] and microtubule-kinesin mixtures. [125] Synthetic active matter includes particles powered by electric fields (Quincke rollers [126]) or chemical activity (Janus particles [127]). According this definition, also systems whose components are not self-propelling can be considered active matter, if the external energy is applied at individual scale: an example is vibrated granular matter. [128]

Given such a wide variety of systems, several different approaches to

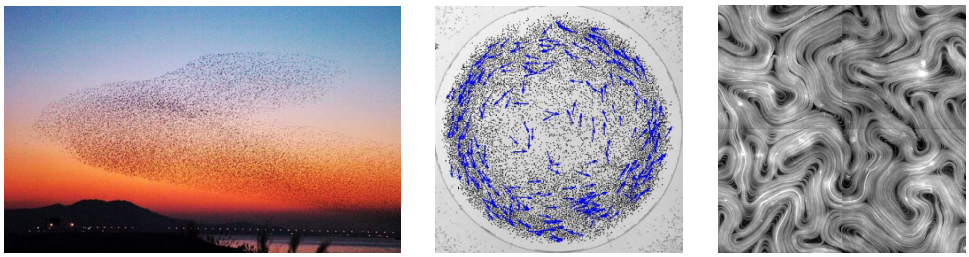

**Figure 8.1:** Examples of active matter exhibiting collective motion: starling flock (left), circular flock of Quincke rollers [126] (center) and active turbulence in microtubule-kinesin mixture [129] (right).

study active matter exist, from which a huge number of models derives, since many of these systems have different basic symmetries and fundamental properties, thus preventing a unified description. We are interested in systems whose properties (related in particular to collective behaviour) can be investigated with a continuum approach, which allows us to employ numerical methods and conceptual instruments from fluid mechanics. Such models are therefore denoted as active fluids.

A great number of active fluid models exists, a first fundamental classification is about their symmetry. Some systems exhibit directional order (similar to the ferromagnetic order in solid state physics), while others show a preferred orientation $\hat{\boldsymbol{n}}$, but with a $\hat{\boldsymbol{n}} \to -\hat{\boldsymbol{n}}$ symmetry (analogous to nematic phase of liquid crystals). The first ones are the **polar** active fluids, with a vectorial order parameter, while the second ones are the **nematic** active fluids, with a rank-2 tensorial order parameter. Other forms include scalar active matter (without a preferential alignment) and chiral active fluids (not invariant under parity inversion). [130] The polar/nematic behaviour is usually due to the symmetry of the constituent particles, with the nematic systems usually composed by "head-tail" symmetric rods, but in some cases, polar particles can still exhibit a nematic order, if the alignment interactions do not distinguish the polarity. For this reasons, in some system we have both nematic and polar effects, which would requires the use of both vectorial and tensorial order parameters, [131,132] although usually the dominant dynamics can be obtained using only one order parameter.

The best-known examples of polar fluids are microswimmers suspensions, [123] Quincke rotors [126] and flocking birds, [133, 134] while the nematic symmetry is typical of microtubules suspensions, [135] crawling bacteria [136] (which are an example of polar particles exhibiting nematic order) and cell tissues. [124] The different symmetries generate peculiar phenomena: in polar fluids we can have emergence of flocking behaviour, while in nematic system a great importance is given to the dynamics of topological defects. Forms of spatio-temporal chaos are present in both of categories: for their apparent resemblance with turbulent flows, they are usually denoted as **active turbulence**. [137] To be more precise, active turbulence is a class of different phenomena, related by some common features (like power-law energy spectra, a complex spatio-temporal structure, absence of energy cascade), but with important differences between them.

Another fundamental distinction is between 'dry' and 'wet' models: dry models are the ones where the solvent dynamics (or the explicit interaction with a substrate) is not explicitly considered, thus the equations do not conserve the momentum. Obviously, in the reality every active system conserves the momentum, but in some cases this can be neglected. For example, an herd of animals moving above a field exchanges momentum with the terrain, but in order to investigate the collective motion of the herd it is not necessary to consider the global system animals + terrain. The distinction dry-wet is therefore more related to the point of view on the system, than the system itself.

In general, we can distinguish two principal approaches in the formulation of the hydrodynamics equations of the models: [137] the first one is phenomenological, starting with a Navier-Stokes-like equation, with terms reproducing the principal features, while the second one is based on liquid crystal models, built from symmetries and conservation laws, although the distinction between these two approaches is not always evident. The first one is particularly adopted for polar models (Toner-Tu model [138] and its variations, but also generalized Navier-Stokes equations [139]), while the second one is the standard in the study of active

nematic, [125] although a research field in polar active liquid crystal also exists. [140]

## 8.1 Toner-Tu model

The Toner-Tu model is the archetype of the description of flocking phenomena with a polar active fluid model. It was originally proposed in 1995 [133], as a continuum version of the discrete Vicsek model, [141] which can be considered an $XY$ model for ferromagnetism, with motile spins. The fundamental hallmark of the Vicsek model is the fact that it exhibits a phase transition towards a long-range ordered phase, in two spatial dimensions, with non-zero thermal noise, thus violating the fundamental Mermin-Wagner-Hohenberg theorem. [142, 143] This theorem states that, in a two-dimensional model with short-range interactions, at thermal equilibrium (with non-zero temperature), it is impossible to have a spontaneous symmetry breaking (if the symmetry is continuous), since thermal fluctuations would destroy the ordered phase. The reason why in the 2D Vicsek model (and in its continuum version) we can have the spontaneous breaking of the rotational symmetry is due to the motility (the only real difference between the Vicsek and the standard $XY$ model), which drives the system away from the thermal equilibrium. [138, 144] In this case, ordered phase means a coordinate collective motion in a particular direction, *i. e.* flocking.

Toner and Tu considered the most general equation of motion for the density $\rho$ and the polarization/velocity $\boldsymbol{u}$, consistently with the symmetries of the system, keeping only the lowest order in gradients and temporal derivatives:

$$\partial_t \rho + \nabla \cdot (\boldsymbol{u}\rho) = 0, \tag{8.1a}$$

$$\begin{aligned} \partial_t \boldsymbol{u} + \lambda_0 (\boldsymbol{u} \cdot \nabla) \boldsymbol{u} + \lambda_1 \nabla \left( \|\boldsymbol{u}\|^2 \right) + \lambda_2 (\nabla \cdot \boldsymbol{u}) \boldsymbol{u} = \\ \alpha \boldsymbol{u} - \beta \|\boldsymbol{u}\|^2 \boldsymbol{u} - \nabla P_1 - \boldsymbol{u} (\boldsymbol{u} \cdot \nabla P_2) \\ + D_1 \nabla (\nabla \cdot \boldsymbol{u}) + D_2 (\boldsymbol{u} \cdot \nabla)^2 \boldsymbol{u} + D_T \nabla^2 \boldsymbol{u} + \boldsymbol{f}. \end{aligned} \tag{8.1b}$$

Here we can observe some resemblances with the compressible Navier-Stokes equation, but also several important differences. Since in this system we do not have Galilean invariance, in the advective term we can have all the combinations of one spatial gradient and two velocities that transform as vectors: this is different from NS, where the momentum conservation implies $\lambda_0 = 1$ and $\lambda_1 = \lambda_2 = 0$. The $\alpha \boldsymbol{u} - \beta \|\boldsymbol{u}\|^2$ term is taken form the Landau theory of phase transitions, [145] and it causes the spontaneous symmetry breaking if $\alpha > 0$. Together with the standard isotropic pressure $P_1$, we have also an anisotropic one $P_2$, both of them are function of the local density and the magnitude of the local velocity. The diffusivity coefficients $D$ play the role of viscosities, while $\boldsymbol{f}$ is an external forcing, which in the original model corresponds to a random "thermal" noise (where $\Delta$ is a constant value and $i, j$ denote the Cartesian components):

$$\langle f_i(\boldsymbol{x}, t)\, f_j(\boldsymbol{x}', t') \rangle = \Delta \delta_{ij} \delta(\boldsymbol{x} - \boldsymbol{x}')\, \delta(t - t')\,. \tag{8.2}$$

The spontaneous breaking of the rotational symmetry, and therefore the establishment of the long-range ordered phase was investigated using methods from the statistical mechanics, in particular the dynamical renormalization group. [144, 146] The analysis showed that in $d > 4$ dimensions, the dynamics is analogous to spin systems at equilibrium, while for $d < 4$ the long distance behaviour is strongly out-of-equilibrium, confirming the spontaneous symmetry breaking in $d = 2$, forbidden at equilibrium by the Mermin-Wagner-Hohenberg theorem. In particular, it was highlighted the fundamental role of nonequilibrium nonlinearities (the $\lambda$ terms) in the stabilization of the ordered phase.

The Toner-Tu is a very generic model, from which numerous variations have been then derived. The first one, already in [144], is the anisotropic version, where a motion along a plain is favoured over motion in other directions: this is the case, for example, of birds flocks, since gravity breaks the symmetry between horizontal and vertical directions. If we relax the "mass" conservation condition, adding a source term in equation (8.1a), we have the case of Malthusian flocks, [147–149] which corresponds to

the situation where the motile particles can reproduce and die. On the other direction, if we assume incompressible flocks the equation (8.1a) is reduced to $\nabla \cdot \boldsymbol{u} = 0$, a case that has been extensively studied both from a statistical physics [150–152] and a fluid mechanics [153–155] point of view. Recently, several works have been published for the case where, along or in place of thermal noise (annealed disorder), there is quenched disorder, which means a forcing random in space but constant in time (representing, for example, a "dirt" domain). This kind of noise destroys ordering in equilibrium systems in $d < 4$: for the compressible Toner-Tu model, it has been shown that long-ranged order is possible also for $d = 3$, while for $d = 2$ only quasi-long-ranged order can happen (which means velocity correlation functions with an algebraic decay), a situation however different from the equilibrium case (where only short-ranged order is possible). [156,157] For the incompressible situation, we have instead true long-ranged order with quenched disorder also for $d = 2$. [158–160] Other generalizations include for example the study in a curved surface [161] or the introduction of an additional "spin" field (in the sense of internal angular momentum) to be more accurate in the description of real birds flocks. [162]

In particular, an incompressible version with a negative "viscosity", and a fourth-order "hyperviscosity", was introduced in 2012 in order to describe dense bacterial suspensions. [123] This is the object of our investigation, and it will be described in the next chapter.

# Chapter 9

# Bacterial turbulence and TTSH model

One of the most simple examples of active fluid (at least regarding the experimental realization) are dense bacterial suspensions. Bacteria (although bacteria constitute an enormous and extremely variegated ensemble of organisms, we will consider elongated rod-shaped flagellated swimmers like *Bacillus subtilis*, *Escherichia coli* or *Serratia marcescens*) are usually pusher-like microswimmers, [5] which, when immersed in dilute environments, exhibit a particular motion denoted as 'run and tumble' behaviour. [18] But when they are grouped in dense package, they can display very complex phenomena, due to various forms of collective behaviour. In particular we will consider the so-called *bacterial turbulence*, an example of active turbulence.

In 2004, in dense quasi-2D suspensions of *B. subtilis*, the presence of coherent structures constituted by swimming bacteria was observed for the first time: [163] in particular, on scales much larger than single cells, the researchers observed "high-speed jets straddled by vortex streets" (see Fig. 9.1). A very interesting feature of this regime was also the fact that these large-scale structures have a much larger speed than the single bacteria self-propulsion. Vortices and jets were reminiscent of two-dimensional inertial turbulence, [105, 107] so already in that article the authors coined the therm "bacterial turbulence", although they

were aware that also important differences to high-Reynolds flows were present.

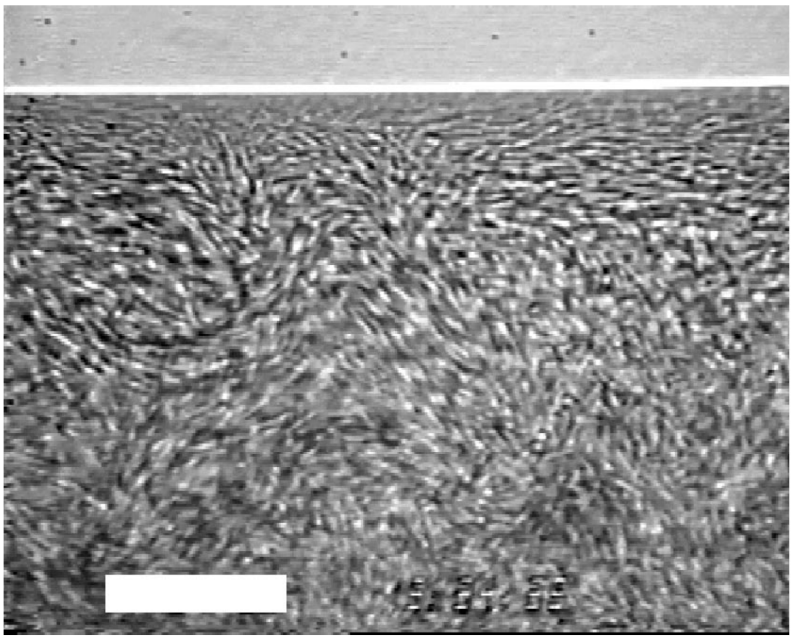

**Figure 9.1:** First experimental observation of bacterial turbulence. The white scale bar is $35\mu m$. *Image taken from* [163].

In the subsequent years several investigations followed, with the observation of further phenomena, like confinement-induced self-organization [164] or even a sort of *supefluidity* [16, 165] (in the sense of negligible viscosity) caused by bacterial activity. This phenomenon, culminating even in a negative viscosity, it has been related on the onset of bacterial turbulence. [18]

From our point of view, the most important work was an experimental-numerical paper in 2012, [123] where, together with an in-depth experimental quantitative study of bacterial turbulence, an effective continuum model was suggested. They proposed an incompressible version of Toner-Tu model for the coarse-grained collective velocity, with a negative effective viscosity (therefore a fourth-order hyperviscosity is necessary for stability reasons):

$$\nabla \cdot \boldsymbol{u} = 0, \tag{9.1a}$$

$$\partial_t \boldsymbol{u} + \lambda_0 \left(\boldsymbol{u} \cdot \nabla\right) \boldsymbol{u} = -\nabla p - \left(\alpha + \beta \|\boldsymbol{u}\|^2\right) \boldsymbol{u} + \Gamma_0 \nabla^2 \boldsymbol{u} + \Gamma_2 \nabla^4 \boldsymbol{u}. \tag{9.1b}$$

In the original paper also the $\lambda_1 \nabla \|\boldsymbol{u}\|^2$ term from TT was present, but, since in this case the velocity field is incompressible, this term can be incorporated in the effective pressure term, and therefore in subsequent papers usually is not displayed.

The equation (9.1) combines the TT terms (self-propulsion with a non unitary coefficient, and Landau forcing) with a double Laplacian, a distinctive element from the Swift-Hohemberg equation for pattern formation. [166] For this reason the model is denoted as Toner-Tu-Swift-Hohemberg (TTSH) equation, [137] although it is sometimes called with more generic names like "mean-bacterial velocity equation" or "bacterial turbulence equation".

Since this model does not describe explicitly the solvent fluid dynamics (and it does not conserve the momentum), it should be considered a dry model. However, works focused on derivation of TTSH model from microswimmers dynamics [167,168] showed that the coefficients take into account, at least as a first approximation, hydrodynamic interactions. It is also important to remark that, in this model, $\boldsymbol{u}$ has the double role of collective velocity and polar order parameter, since it is assumed that rod-shaped bacteria move in their symmetry axis direction, and also that they have approximately the same self-propulsion speed.

From the coefficients in (9.1) we can obtain space and velocity scales. In particular, the quantity $\Lambda \equiv 2\pi\sqrt{(2\Gamma_2)/\Gamma_0}$, emerging from the instability of null-field state (see section 9.1), corresponds to the length scale of vortices. The presence of this fixed scale, well observed in experiments (where $\Lambda \sim 20 - 50\mu m$ is found), indicates that this system is strongly non-scale invariant, a very important difference with inertial turbulence. [105] Regarding velocity scale, in this case we have two possibilities, depending on what is more important between the Landau potential or the Swift-Hohenberg operator in the dynamics of the flow we are considering:

$$U = \sqrt{\frac{-\alpha}{\beta}}, \qquad V = \sqrt{\frac{\Gamma_0^3}{\Gamma_2}}. \tag{9.2}$$

In the TTSH model we therefore have 5 different coefficients, but we

can simplify our parameter space. It is a common procedure to maintain fixed the value of $\Lambda$ (and therefore the values of $\Gamma_0$ and $\Gamma_2$) and $\beta$, while exploring the phase diagram varying $\lambda_0$ and $\alpha$. Regarding $\Lambda$, we can identify two different strategies: setting $\Lambda = 2\pi$ with $\Gamma_0 = -2$ and $\Gamma = -1$, [169–171], that we will call normalization A, or setting $\Gamma_0 = -0.045$ and $\Gamma_2 = \Gamma_2^3$, [123, 172–174] that we will call normalization B. Regarding the value of $\alpha$ and $\beta$,the situation is more complicated: while in normalization B is common to adopt $\beta = 0.5$, in normalization A the situation is more intricate: it is possible to find $\beta = 0.01$ [169] or $\beta = 1.6$ [171] and $\alpha$ can be re-expressed as $\alpha - 1$ or even $1 - \alpha$. For $\lambda_0$, being non-dimensional, we do not have such ambiguities. We chose to consider normalization A with $\beta = 0.01$, without re-definition of $\alpha$ (so $\alpha < 0$ means forcing and $\alpha > 0$ friction).

The TTSH model is a simplified effective model, thus having several limitations. For these reasons, in the last years two different extensions have been proposed: a two-fields version, in order to investigate also the dynamics of the solvent fluid, and a compressible version, since the incompressibility hypothesis is not always physically justified. The first one was elaborated especially in order to relate the phenomenological coefficients to microscopic parameters, [167, 168] and it will be better described in section 9.2. The second one was proposed in order to unify the description of bacterial turbulence with the one of motility-induced phase separation, [175, 176] and it includes a non-trivial density field, described by an advection-diffusion equation. In this version, velocity and polarization are not the same field, since, although they are still parallel, self-propulsion speed is assumed to be dependent on density, which affects the ratio of their moduli, as well as the effective coefficient $\alpha$ (see equation (9.3)).

$$\partial_t \rho = -\nabla \cdot [v(\rho)\,\boldsymbol{p}] + D\nabla^2 \rho \tag{9.3a}$$

$$\partial_t \boldsymbol{p} + \lambda_0 (\boldsymbol{p} \cdot \nabla)\,\boldsymbol{p} = -\frac{1}{2}\nabla [v(\rho)\,\rho] - \left(\alpha(\rho) + \beta \|\boldsymbol{p}\|^2\right)\boldsymbol{p} + \Gamma_0 \nabla^2 \boldsymbol{p} + \Gamma_2 \nabla^4 \boldsymbol{p}, \tag{9.3b}$$

$$v(\rho) = -c\left[\rho - \frac{1}{2}(\rho_{max} - \rho_{min})\right]^2 + v_0, \qquad \alpha(\rho) = \alpha_0(\rho_c - \rho). \tag{9.3c}$$

## 9.1 Linear stability

Equation 9.1, with periodic boundary conditions, has two uniform steady solution: the isotropic disordered state $(\boldsymbol{u}, p) = (\boldsymbol{0}, p_0)$ and, for $\alpha < 0$, the manifold of globally ordered states $(\boldsymbol{u}, p) = (\boldsymbol{u}_0, p_0)$, where $\boldsymbol{u}_0$ is a vector with arbitrary orientation and modulus $\|u_0\| = U \equiv \sqrt{-\alpha/\beta}$. In both cases, $p_0$ is a constant pressure. It is trivial that for $\alpha < 0$ the ordered state is favourite over the disordered one, it is an example of spontaneous symmetry breaking. The following analysis is aimed to understand the stability of uniform states over non-uniform perturbations. It was originally displayed in the supplementary of [123] and extended in [177], and in the subsequent years other studies, more rigorous from a mathematical point of view, have deepened the topic (along other related issues, like wellposedness of the model). [178–180]

#### Disordered state

We will consider the equation 9.1 in a two-dimensional domain with periodic boundary conditions. We start considering the disordered state ($\alpha > 0$), setting the perturbation as $(\boldsymbol{\varepsilon}, \eta)$ (with $\eta \ll p_0$), and we linearize the TTSH equation around the perturbed solution:

$$\nabla \cdot \boldsymbol{\varepsilon} = 0, \tag{9.4a}$$

$$\partial_t \boldsymbol{\varepsilon} = -\nabla \eta - \alpha \boldsymbol{\varepsilon} + \Gamma_0 \nabla^2 \boldsymbol{\varepsilon} + \Gamma_2 \nabla^4 \boldsymbol{\varepsilon}. \tag{9.4b}$$

Now, it is natural to consider a monochromatic perturbation (with $\boldsymbol{k} \neq 0$):

$$(\boldsymbol{\varepsilon}, \eta) = (\hat{\boldsymbol{\varepsilon}}, \hat{\eta})\, e^{i\boldsymbol{k}\cdot\boldsymbol{x} + \sigma t}, \tag{9.5}$$

in order to obtain an algebraic relationship (where $k = \|\boldsymbol{k}\|$):

$$\boldsymbol{k} \cdot \hat{\boldsymbol{\varepsilon}} = 0, \tag{9.6a}$$

$$\sigma \hat{\boldsymbol{\varepsilon}} = -i\boldsymbol{k}\hat{\eta} - \left(\alpha + \Gamma_0 k^2 - \Gamma_2 k^4\right) \hat{\boldsymbol{\varepsilon}}. \tag{9.6b}$$

Multiplying the second equation for $\boldsymbol{k}$, to satisfy the incompressibility we must have $\hat{\eta} = 0$, and therefore we get a dispersion relationship:

$$\sigma\left(\boldsymbol{k}\right) = -\alpha - \Gamma_0 k^2 + \Gamma_2 k^4. \tag{9.7}$$

Now, since we already assumed $\Gamma_2 < 0$ and $\alpha > 0$, the sign of $\Gamma_0$ is crucial: if $\Gamma_0 > 0$, we have $\sigma < 0$ for every $k$, and therefore the disordered state is always linearly stable. But, if $\Gamma_0 < 0$ (*i.e.* for a negative effective viscosity) we obtain an unstable band of modes: $\sigma(\boldsymbol{k}) > 0$ for $k_-^2 < k^2 < k_+^2$, with

$$k_\pm^2 = \frac{|\Gamma_0|}{|\Gamma_2|}\left(\frac{1}{2} \pm \sqrt{\frac{1}{4} - \frac{\alpha|\Gamma_2|}{|\Gamma_0|^2}}\right), \qquad \text{if} \qquad \alpha < \alpha_s \equiv \frac{1}{4}\frac{|\Gamma_0|^2}{|\Gamma_2|}. \tag{9.8}$$

This means that, if misaligning effects between swimmers (parametrized by a positive value of $\alpha$) are not too much intense, the uniform disordered will be substituted by a non-uniform state corresponding to bacterial turbulence. In particular, if we derive the relationship 9.7 with respect to $k$, we obtain the most unstable mode $k_c = \sqrt{\Gamma_0/2\Gamma_2}$. Since this one is the mode corresponding to the maximum perturbation growth, this instability selects the establishment of structures with particular length scale:

$$\Lambda = \frac{2\pi}{k_c} = 2\pi\sqrt{\frac{2\Gamma_2}{\Gamma_0}}. \tag{9.9}$$

For this reason $\Lambda$ is called vortex length scale, since vortices are the coherent structures originated by the instability (see figure 9.2). This mechanism of pattern formation is precisely the one described by the Swift-Hohemberg equation.

#### Polar state

For the polar state ($\alpha < 0$), we can adopt a similar procedure. In this case, the perturbed solution is $(\boldsymbol{u}_0 + \boldsymbol{\varepsilon}, p_0 + \eta)$, and, since in this case we do not have rotational symmetry, it is convenient to explicitly define a reference frame. We can set the $x$-axis as the orientation, and therefore decompose the perturbation in parallel and perpendicular components:

$$\boldsymbol{u}_0 + \boldsymbol{\varepsilon} = \left(U + \varepsilon_\parallel, \varepsilon_\perp\right). \tag{9.10}$$

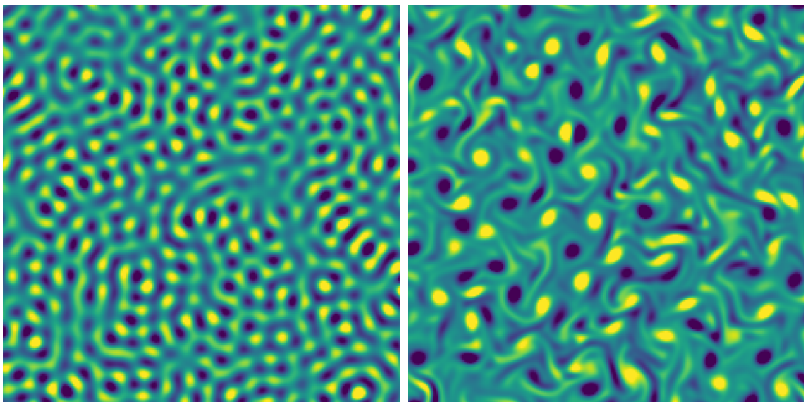

**Figure 9.2:** Vorticity fields (from direct numerical simulations) emerging from the instability (using a very small random perturbation) of the disordered state ($\alpha > 0$), during the linear regime (*left*) and during the non-liner regime at later times (*right*). We can clearly observe the isotropic pattern expected from the stability analysis, from which the vortices originate. *Own work*

Linearizing around this perturbed solution (recalling that $U^2\beta = -\alpha$) we get a slightly more complicated equation:

$$\nabla \cdot \boldsymbol{\varepsilon} = 0, \tag{9.11a}$$

$$\partial_t \boldsymbol{\varepsilon} + \lambda_0 \left(\boldsymbol{u}_0 \cdot \nabla\right) \boldsymbol{\varepsilon} = -\nabla\eta + 2\alpha\varepsilon_\parallel \boldsymbol{e}_x + \Gamma_0 \nabla^2 \boldsymbol{\varepsilon} + \Gamma_2 \nabla^4 \boldsymbol{\varepsilon}. \tag{9.11b}$$

Considering also in this case a monochromatic perturbation:

$$\left(\varepsilon_\parallel, \varepsilon_\perp, \eta\right) = \left(\hat{\varepsilon}_\parallel, \hat{\varepsilon}_\perp, \hat{\eta}\right) e^{i\boldsymbol{k}\cdot\boldsymbol{x}+\sigma t}, \tag{9.12}$$

the algebraic relationship is now:

$$\boldsymbol{k} \cdot \hat{\boldsymbol{\varepsilon}} = 0, \tag{9.13a}$$

$$\sigma\hat{\boldsymbol{\varepsilon}} = -i\boldsymbol{k}\hat{\eta} + \mathbf{A}\hat{\boldsymbol{\varepsilon}}, \tag{9.13b}$$

where $\mathbf{A}$ is a $2 \times 2$ matrix:

$$\mathbf{A} = \begin{pmatrix} 2\alpha & 0 \\ 0 & 0 \end{pmatrix} - \left(\Gamma_0 k^2 - \Gamma_2 k^4 + i\lambda_0 k_x U\right) \mathbf{I}. \tag{9.14}$$

If we multiply the second equation with $i\boldsymbol{k}$ and we use the incompressibility relationship, we obtain:

$$\hat{\eta} = -i\frac{\boldsymbol{k} \cdot (\mathbf{A}\hat{\boldsymbol{\varepsilon}})}{k^2}. \tag{9.15}$$

At this point we can define another matrix $\mathbf{A}_\perp$ as:

$$\mathbf{A}_\perp = \mathbf{\Pi}(\boldsymbol{k})\,\mathbf{A}, \qquad \text{with} \qquad \Pi_{ij} = \delta_{ij} - k_i k_j, \tag{9.16}$$

which allows us to express equation 9.13b as:

$$\sigma\hat{\boldsymbol{\varepsilon}} = \mathbf{A}_\perp\hat{\boldsymbol{\varepsilon}}. \tag{9.17}$$

Eigenvalues of $\mathbf{A}_\perp$ provide us the dispersion relationship:

$$\sigma(\boldsymbol{k}) \in \{0, -\Gamma_0 k^2 + \Gamma_2 k^4 + 2\alpha\frac{k_x^2}{k^2} - i\lambda_0 U k_x\} \tag{9.18}$$

The second eigenvalue in 9.18 is what interests us, and its corresponding eigenvector is $(-k_y, k_x)$. We have maximum $\Re[\sigma(\boldsymbol{k})]$ for $\boldsymbol{k} = \left(0, \sqrt{\Gamma_0/2\Gamma_2}\right)$, and therefore $\left(-\sqrt{\Gamma_0/2\Gamma_2}, 0\right)$ as eigenvector. This means that the polar uniform state is always unstable if $\Gamma_0 < 0$, and that we have the establishment of elongated coherent structures transverse with respect to mean flow (corresponding to the *vorticity streaks* observed in simulations), having a wavelength $\Lambda$ along the mean flow direction (see figure 9.3).

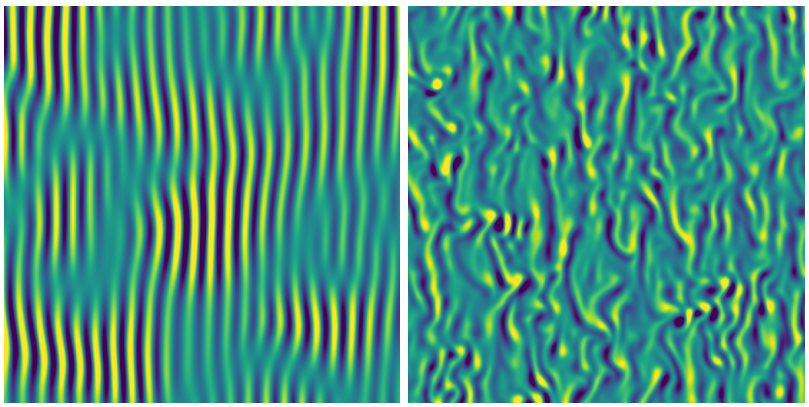

**Figure 9.3:** Vorticity fields (from direct numerical simulations) emerging from the instability (using a very small random perturbation) of the polar state ($\alpha < 0$), during the linear regime (*left*) and during the non-liner regime at later times (*right*). Mean flow goes horizontally from left to right. We can clearly observe the transverse pattern expected from the stability analysis, not completely destroyed by non-linear terms. *Own work*

This stability analysis is therefore important because, in addition to the problem of stability itself, it explains the principal features of structures that we can observe in simulations also at strongly nonlinear regimes.

In particular, the structures originated by the instability of polar state will have great importance in our study of the flocking turbulence and the circular flocking we observed (see Chapters 10 and 11).

## 9.2 Derivation of the TTSH model

A first phenomenological derivation of TTSH, from general considerations, was presented in [123, 177]. Some years later, in [167, 168] a more rigorous derivation was proposed, from microscopic dynamics. In this case, the TTSH model emerges from a two-fields (solvent and bacteria velocities) model, in the limit of weak coupling between swimmers and fluid.

### 9.2.1 Phenomenological derivation

Originally, [123, 177] the TTSH model was proposed according two hypothesis:

- at high densities, bacteria suspensions have an incompressible dynamics;
- the interesting dynamics can be captured by a single vectorial field having the double role of coarse-grained velocity and mean orientation.

The first hypothesis is implemented with a divergence-free field $\nabla \cdot \boldsymbol{u} = 0$. The second one leads to a generalized Navier-Stokes equation:

$$(\partial_t + \boldsymbol{u} \cdot \nabla)\, \boldsymbol{u} = -\nabla p - \left(\alpha + \beta \|\boldsymbol{u}\|^2\right) \boldsymbol{u} + \nabla \cdot E \tag{9.19}$$

where the $(\alpha + \beta\|\boldsymbol{u}\|^2)$ terms is inherited from Toner-Tu model in order to describe aligning interactions, $p$ is a Lagrangian multiplier assuring incompressibility and $E$ is an effective rate of strain tensor. Then, a closure of $E$ in terms of velocity field is postulated:

$$E_{ij} = \Gamma_0 \left(\partial_i u_j + \partial_j u_i\right) + \Gamma_2 \nabla^2 \left(\partial_i u_j + \partial_j u_i\right) + S q_{ij} \tag{9.20}$$

where $q_{ij} = u_i u_j - (\delta_{ij}/d)\,\|\boldsymbol{u}\|^2$ is a mean-field approximation of the nematic active stress tensor in $d$ dimensions. [181] From general hydrodynamics arguments it is assumed that we have $S < 0$ for pusher-like swimmers, while $S > 0$ for puller-like ones. [182] It is also assumed that the "viscosity" $\Gamma_0$ can be negative (in order to destabilize the uniform state), and so also $\Gamma_2 < 0$ for stability reasons.

So, if we substitute the expression (9.20) into equation (9.19), and we define:

$$\lambda_0 = 1 - S, \qquad \lambda_1 = -S/d, \tag{9.21}$$

we obtain the standard TTSH model

$$\partial_t \boldsymbol{u} + \lambda_0 \left(\boldsymbol{u}\cdot\nabla\right)\boldsymbol{u} = -\nabla p + \lambda_1 \nabla\|\boldsymbol{u}\|^2 - \left(\alpha + \beta\|\boldsymbol{u}\|^2\right)\boldsymbol{u} + \Gamma_0\nabla^2\boldsymbol{u} + \Gamma_2\nabla^4\boldsymbol{u}. \tag{9.22}$$

As anticipated, we can redefine pressure in order to include the $\lambda_1$ term:

$$p - \lambda_1\|\boldsymbol{u}\|^2 \quad \rightarrow \quad p. \tag{9.23}$$

So $\lambda_0 > 1$ corresponds to pushers suspensions, while $\lambda_0 < 1$ should correspond to pullers, although at 2022 there are no experimental works proving that the dynamics of a pullers suspension can be simulated with the TTSH model having $\lambda_0 < 1$.

### 9.2.2 Derivation in terms of microscopic parameters

Although it was immediately proved, comparing simulations to experiments, that the TTSH model can describe pusher-like dense suspensions, [123, 183] a clear link between phenomenological coefficients and microscopic physical quantities was missing. A first attempt to resolve this problem was presented in 2016, [167] and expanded in 2018. [168] Since it requires very long calculations, only fundamental aspects of this derivation will be described in this section.

In this subsection, $\boldsymbol{u}$ denote the solvent fluid velocity field, differently from the rest of the chapter.

#### Swim and interactions

The starting point is to assume that, at large distances, microswimmers can be represented as cylindrical rods moving, with constant velocity $v_0$, along their mean axis direction, $\boldsymbol{n}$ causing a flow that can be modelled as a stresslet, *i. e.* a force-dipole. A swimmer will therefore exert a force $\mathbf{F} = \pm f_0 \boldsymbol{n}$, with positive sign for pullers and negative one for pushers.

It is then necessary to model interactions between swimmers, crucial in dense suspensions. In the coarse-grained description in [168], authors distinguished between short range alignment interactions and far-field hydrodynamic interactions (see Fig. 9.4). Short-range ones are parametrized by an effective potential, and it is assumed that they are of two different typologies. Authors postulated that there is a activity-driven polar alignment due to near-field hydrodynamic interactions, and a passive nematic alignment due to steric effects. The ansatz chosen for the potential between the $\mu$-esim and the $\nu$-esim swimmer is:

$$\phi\left(\boldsymbol{n}^{\mu}, \boldsymbol{n}^{\nu}, r^{\mu\nu}\right) = -\frac{\gamma_0 v_0}{2} \boldsymbol{n}^{\mu} \cdot \boldsymbol{n}^{\nu} \Theta\left(\epsilon_a - r^{\mu\nu}\right) - \frac{\gamma_1}{4} \left(\boldsymbol{n}^{\mu} \cdot \boldsymbol{n}^{\nu}\right)^2 \Theta\left(\epsilon_p - r^{\mu\nu}\right), \tag{9.24}$$

where $r^{\mu\nu}$ is the distance between the swimmers, $\gamma_0$ and $\gamma_1$ are the magnitude of active and passive interactions, $\Theta$ is the Heaviside function, and $\epsilon_a$ and $\epsilon_p$ are the ranges of these interactions. $\epsilon_a = \epsilon_p = \epsilon$ will be assumed for simplicity. The first term is multiplied by $v_0$ in order to depend on activity. The fact that the first term depends on the scalar product $\boldsymbol{n}^{\mu} \cdot \boldsymbol{n}^{\nu}$, while the second one on its square, indicates that the first one induces a polar alignment, while the second one a nematic order. Far-field hydrodynamic interactions will be instead included in the stress tensor, and therefore in the fluid velocity field.

#### Langevin and Fokker-Planck

At this point, we consider the equations of motion for a single swimmer. We have two Langevin equations, one for the translational motion, and one for the rotational one:

$$\frac{d}{dt}\mathbf{X}^{\mu} = v_0 \boldsymbol{n}^{\mu} + \boldsymbol{u}\left(\mathbf{X}^{\mu}, t\right) + \sqrt{2D}\boldsymbol{\xi}^{\mu}\left(t\right), \tag{9.25a}$$

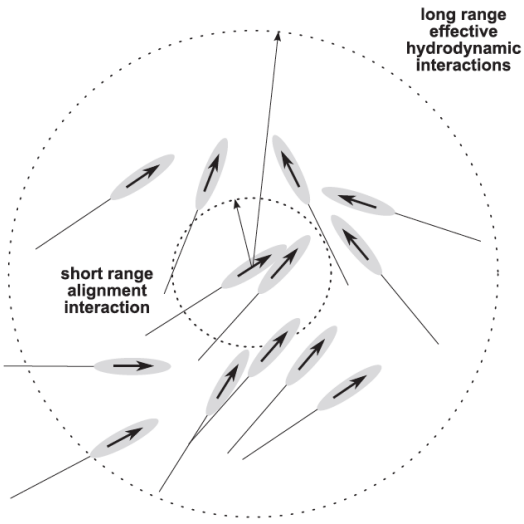


**Figure 9.4:** Coarse-grained interactions between microswimmers, according [168].

$$\frac{d}{dt}\boldsymbol{n}^{\mu}(t) = \boldsymbol{\Omega}(\mathbf{X}^{\mu}, t)\cdot\boldsymbol{n}^{\mu} + (\mathbf{I} - \boldsymbol{n}^{\mu}\boldsymbol{n}^{\mu})\cdot$$
$$\left[a_0\boldsymbol{\Sigma}(\mathbf{X}^{\mu}, t)\cdot\boldsymbol{n}^{\mu}(t) - \nabla_{\boldsymbol{n}^{\mu}}\Phi(\boldsymbol{n}) + \tau^{-1/2}\boldsymbol{\eta}^{\mu}(t)\right]. \tag{9.25b}$$

As we can see, the equation for the center of mass contains self-propulsion, advective transport and thermal noise $\boldsymbol{\xi}$, while rotational motion is a modified version of the Jeffery equation, with a term due to short-range interactions (with $\Phi(\boldsymbol{n}) = \Sigma_{\mu,\nu}\phi(\boldsymbol{n}^{\mu}, \boldsymbol{n}^{\nu}, r^{\mu\nu})$) and another term $\boldsymbol{\eta}$ due to thermal noise. $D$ and $\tau$ are the Brownian diffusivities, while $a_0$ is the geometrical Jeffery factor, assumed to be identical to the one for passive particles.

From these Langevin equations, we want to obtain a continuum description. We therefore define a one-particle probability distribution $\mathcal{P}(\boldsymbol{x}, \boldsymbol{n}, t)$, first three moments of the distribution will be, respectively, the scalar, polar and nematic (made traceless) order parameter:

$$\rho(\boldsymbol{x}, t) = \int d\boldsymbol{n}\mathcal{P}(\boldsymbol{x}, \boldsymbol{n}, t), \tag{9.26}$$

$$\mathbf{P}(\boldsymbol{x}, t) = \int d\boldsymbol{n}\mathcal{P}(\boldsymbol{x}, \boldsymbol{n}, t)\,\boldsymbol{n}, \tag{9.27}$$

$$\mathbf{Q}(\boldsymbol{x}, t) = \left(\int d\boldsymbol{n}\mathcal{P}(\boldsymbol{x}, \boldsymbol{n}, t)\,\boldsymbol{n}\boldsymbol{n}\right) - \frac{\mathbf{I}}{d}. \tag{9.28}$$

The corresponding Fokker-Planck equation to the Langevin equations (9.25a) and (9.25b) is:

$$\begin{aligned}\partial_t \mathcal{P}(\boldsymbol{x},\boldsymbol{n},t) &= -\nabla\cdot\left[\left(v_0\boldsymbol{n}+\boldsymbol{u}\right)\mathcal{P}\right]+D\nabla^2\mathcal{P}\\ -\nabla_{\boldsymbol{n}}&\left[\left(\boldsymbol{\Omega}\cdot\boldsymbol{n}+a_0\boldsymbol{\Pi}(\boldsymbol{n})\cdot\boldsymbol{\Sigma}\cdot\boldsymbol{n}-\frac{1}{\tau}\boldsymbol{n}\right)\mathcal{P}\right]+\\ &\frac{1}{2\tau}\nabla_{\boldsymbol{n}}\nabla_{\boldsymbol{n}}:\left[\boldsymbol{\Pi}(\boldsymbol{n})\cdot\boldsymbol{\Pi}^T(\boldsymbol{n})\,\mathcal{P}\right]+\mathcal{C}^{(2)}[\Phi],\end{aligned}\tag{9.29}$$

where $\boldsymbol{\Pi}(\boldsymbol{n})$ is the orthogonal projector $\mathbf{I}-\boldsymbol{nn}$. The last term of equation (9.29) is the two-particles interaction integral, depending on short-range potential $\Phi$ and the two-particles probability distribution $\mathcal{P}(\boldsymbol{x},\boldsymbol{n};\boldsymbol{x}',\boldsymbol{n}';t)$. Expressing this term in a simple form requires several approximation and long calculations, authors of [168] at the end obtained:

$$\begin{aligned}\partial_t \mathcal{P}(\boldsymbol{x},\boldsymbol{n},t) &= -\nabla\cdot\left[\left(v_0\boldsymbol{n}+\boldsymbol{u}\right)\mathcal{P}\right]+D\nabla^2\mathcal{P}\\ -\nabla_{\boldsymbol{n}}&\left[\left(\boldsymbol{\Omega}\cdot\boldsymbol{n}+a_0\boldsymbol{\Pi}(\boldsymbol{n})\cdot\boldsymbol{\Sigma}\cdot\boldsymbol{n}-\frac{1}{\tau}\boldsymbol{n}\right.\right.\\ &\left.\left.+\gamma_0 v_0\boldsymbol{\Pi}(\boldsymbol{n})\cdot\boldsymbol{J}(\rho\mathbf{P})+\gamma_1\boldsymbol{\Pi}(\boldsymbol{n})\cdot\boldsymbol{J}(\rho\mathbf{Q})\cdot\boldsymbol{n}\right)\mathcal{P}\right]+\\ &\frac{1}{2\tau}\nabla_{\boldsymbol{n}}\nabla_{\boldsymbol{n}}:\left[\boldsymbol{\Pi}(\boldsymbol{n})\cdot\boldsymbol{\Pi}^T(\boldsymbol{n})\,\mathcal{P}\right],\end{aligned}\tag{9.30}$$

with:

$$\boldsymbol{J}(\,) = \left(A_d + B_d\nabla^2 + C_d\nabla^4\right)(\,),\tag{9.31}$$

where $A_d$, $B_d$ and $C_d$ are geometrical factors depending on interaction range $\epsilon$ and dimensionality $d$.

#### Stress tensor

Now, in order to close equation (9.30) we have to consider how the solvent velocity $\boldsymbol{u}$ is affected by microswimmers. We assume, since bacteria swim at very low Reynolds number, $\boldsymbol{u}$ to be described by Stokes equation, with a extra non-Newtonian stress $\boldsymbol{\sigma}$ due to swimmers:

$$\mu^*\nabla^2\boldsymbol{u}-\nabla p+\nabla\cdot\boldsymbol{\sigma}=0,\qquad\qquad \nabla\cdot\boldsymbol{u}=0.\tag{9.32}$$

Here $\mu^*$ is the effective viscosity, which takes into account the effect of swimmers volume fraction $c$ to the Newtonian viscosity. Usually a

Batchelor-Einstein relationship [80, 184] is assumed:

$$\mu^* = \mu_0 \left(1 + k_1 c + k_3 c^2\right) \tag{9.33}$$

where, for pusher-like swimmers, the coefficients $k_i$ have to be fitted with experimental data. The non-Newtonian stress tensor is composed by an active $\boldsymbol{\sigma}^a$ and a passive $\boldsymbol{\sigma}^p$ part. The active component is defined as $\nabla \cdot \boldsymbol{\sigma}^a = \mathbf{f}$, where $\mathbf{f}$ is the force density deriving from bacteria swimming, that we can express using a multipole expansion, which averaged through $\mathcal{P}(\boldsymbol{x}, \boldsymbol{n}, t)$ becomes:

$$\begin{aligned}\boldsymbol{\sigma}^a \approx -f_0 \left[\zeta_1 (\rho \overline{\boldsymbol{nn}}) + \zeta_2 \nabla \cdot (\rho \overline{\boldsymbol{nnn}}) + \zeta_3 \nabla\nabla : (\rho \overline{\boldsymbol{nnnn}}) + \right. \\ \left. \zeta_4 \nabla\nabla\nabla : \cdot (\rho \overline{\boldsymbol{nnnnn}}) + \dots \right],\end{aligned} \tag{9.34}$$

where $\zeta_i$ are coefficients dependent on dipole length. The passive stress can be instead computed from liquid crystal theory, [185] and it depends on the nematic order parameter (and higher-order terms):

$$\boldsymbol{\sigma}^p \approx \rho \vartheta \mathbf{Q} + \dots \tag{9.35}$$

where $\vartheta$ is a concentration dependent parameter.

#### Field equations

From the Fokker-Planck equation we want to obtain simpler equations for the order parameters, viable to be numerically simulated. Averaging equation (9.30) over $\boldsymbol{n}$ we obtain a continuity equation for the density $\rho$:

$$\partial_t \rho = -\nabla \cdot \left[\rho \left(v_0 \mathbf{P} + \boldsymbol{u}\right)\right] + D \nabla^2 \rho. \tag{9.36}$$

Here comes one of the fundamental hypothesis of the TTSH model: negligibility of density fluctuations ($\rho$ = constant). This implies $\nabla \cdot (v_0 \mathbf{P} + \boldsymbol{u}) = 0$, and since we know that solvent velocity is incompressible ($\nabla \cdot \boldsymbol{u} = 0$), this means that also the polarization $\mathbf{P}$ is incompressible:

$$\nabla \cdot \mathbf{P} = 0. \tag{9.37}$$

Multiplying equation (9.30) with $\boldsymbol{n}$ and averaging, we obtain the equation for $\mathbf{P}$. Knowing that $\rho$ = constant, $\overline{\boldsymbol{nn}} = \mathbf{Q} + \mathbf{I}/d$ and the fact that

$\boldsymbol{u}$ (and its derivatives $\boldsymbol{\Omega}$ and $\boldsymbol{\Sigma}$) are already averaged quantities, we get:

$$(\partial_t + \boldsymbol{u}\cdot\nabla)\,\mathbf{P} = \boldsymbol{\Omega}\cdot\mathbf{P} + a_0\boldsymbol{\Sigma}\cdot\mathbf{P} - v_0\nabla\cdot\mathbf{Q} + D\nabla^2\mathbf{P} - \frac{1}{\tau}\mathbf{P} - a_0\boldsymbol{\Sigma} : \overline{\boldsymbol{nnn}}$$
$$+\gamma_0 v_0\rho\frac{d-1}{d}\boldsymbol{J}(\mathbf{P}) - \gamma_0 v_0\rho\mathbf{Q}\cdot\boldsymbol{J}(\mathbf{P}) + \gamma_1\rho\boldsymbol{J}(\mathbf{Q})\cdot\mathbf{P} - \gamma_1\rho\boldsymbol{J}(\mathbf{Q}) : \overline{\boldsymbol{nnn}}. \tag{9.38}$$

Similar arguments lead to the equation for the nematic tensor $\mathbf{Q}$:

$$\begin{aligned}(\partial_t + \boldsymbol{u}\cdot\nabla)\,\mathbf{Q} = {} & 2\,(\boldsymbol{\Omega}\cdot\mathbf{P})^{ST} + 2a_0\,(\boldsymbol{\Sigma}\cdot\mathbf{P})^{ST} - v_0\,(\nabla\cdot\overline{\boldsymbol{nnn}})^{ST} \\ & + D\nabla^2\mathbf{Q} - \frac{3}{\tau}\mathbf{Q} + \frac{2a_0}{d}\boldsymbol{\Sigma} - a_0\,(\boldsymbol{\Sigma} : \overline{\boldsymbol{nnnn}})^{ST} \\ & + 2\gamma_0 v_0\rho\,(\boldsymbol{J}(\mathbf{P})\,\mathbf{P})^{ST} - 2\gamma_0 v_0\rho\,(\cdot\boldsymbol{J}(\mathbf{P})\cdot\overline{\boldsymbol{nnn}})^{ST} \\ & + 2\gamma_1\rho\,(\boldsymbol{J}(\mathbf{Q})\cdot\mathbf{Q})^{ST} + \frac{2\gamma_1\rho}{d}\boldsymbol{J}(\mathbf{Q}) - \gamma_1\rho\,(\boldsymbol{J}(\mathbf{Q}) : \overline{\boldsymbol{nnnn}})^{ST},\end{aligned} \tag{9.39}$$

where $ST$ means "symmetric-traceless". As it usual in moment equations, now we have a standard closure problem: computing evolution of $\mathbf{P}$ and $\mathbf{Q}$ requires knowledge of high-order moments. We therefore want to express these quantities in terms of $\mathbf{P}$ and $\mathbf{Q}$, and then, since we know from experiments that in bacterial suspensions polar effects are dominant over nematic ones, to express $\mathbf{Q}$ in terms of $\mathbf{P}$.

Regarding high-order moments, authors of [168] adopted the Hand closure, [186] which means:

$$(\overline{\boldsymbol{nnn}})^{ST} = (\overline{\boldsymbol{nnn}})^{ST} = (\overline{\boldsymbol{nnnnn}})^{ST} = 0. \tag{9.40}$$

In order to relate $\mathbf{Q}$ to $\mathbf{P}$ a modified version of Doi closure for passive nematics [24] was proposed:

$$\mathbf{Q} = q\,(\mathbf{PP})^{ST} + \lambda_K\boldsymbol{\Sigma}, \tag{9.41}$$

where the term proportional to $\Sigma$ should take in account velocity gradients generated by active particles. The coefficients $q$ and $\lambda_K$ are related to microscopic parameters, and are obtained imposing $\partial_t\mathbf{Q} = 0$ in equation (9.39), keeping only linear terms in $\mathbf{Q}$ and $\boldsymbol{\Sigma}$ or quadratic in $\mathbf{P}$.

After long calculations, applying these closures and neglecting higher order derivatives, finally we have the equations for the fluid velocity $\boldsymbol{u}$

and polarization $\mathbf{P}$:

$$\nabla^2 \boldsymbol{u} = \frac{f_0 \rho}{\mu_{eff}} \left[ \xi_1 \left( 1 - \frac{\vartheta}{f_0 \xi_1} \right) q\mathbf{P} \cdot \nabla \mathbf{P} + \left( \xi_2 + \xi_4 \nabla^2 \right) \nabla^2 \mathbf{P} \right] + \nabla p_{eff}, \tag{9.42a}$$

$$\begin{aligned} &\left(\partial_t + \boldsymbol{u} \cdot \nabla + \lambda_0 \mathbf{P} \cdot \nabla\right) \mathbf{P} = \\ &\left(\boldsymbol{\Omega} + \kappa \boldsymbol{\Sigma}\right) \cdot \mathbf{P} - \nabla p^* - \alpha \mathbf{P} - \beta \|\mathbf{P}\|^2 \mathbf{P} + \Gamma_0 \nabla^2 \mathbf{P} + \Gamma_2 \nabla^4 \mathbf{P}. \end{aligned} \tag{9.42b}$$

As we can see, the equation for the polarization is an extended version of TTSH model with additional terms related to solvent velocity and its derivatives, while in the Stokes equation we see how the solvent fluid is influenced by swimmers.

Effective pressures $p_{eff}$ and $p^*$ are given by the sum of a term proportional to ordinary pressure and a term proportional to $\|\mathbf{P}\|^2$ (corresponding to the $\lambda_1$ term), also the viscosity is modified by activity. The total velocity field of bacteria is therefore $\boldsymbol{w} = \boldsymbol{u} + v_0 \mathbf{P}$.

We see a huge number of coefficients: $\xi_i$ are geometrical factors related to swimmers dipole length, the other ones are combinations of the various microswimmers properties. To handle this parameter space, authors of [168] proposed also a normalization scheme, in order to express all the parameters in terms of five non-dimensional quantities, which quantify the weight of principal factors. Assuming that nematic effects are negligible ($\gamma_1 = \vartheta = 0$), as well as the translation diffusivity $D$, these non dimensional parameters are:

- persistence number $P_r = v_0 \tau / \ell$ (where $\ell$ is the bacterial length), quantifying the importance of rotational Brownian effects;
- feedback coefficient $c_F = f_0 \rho \ell^2 / (10 \mu_{eff} v_0)$, measuring the effect of activity on solvent fluid;
- interaction coefficient $c_I = \frac{8}{9} \pi \tau \rho \gamma_0 v_0 \epsilon^3$, estimating the strength of polar alignment between swimmers;
- ratio $\epsilon / \ell$ between bacterial length and interaction range;
- Jeffery factor $a_0$.

With this scheme, adopting $\ell$, $\ell/v_0$ and $v_0$ as space, time and velocity scales, the proposed values for the coefficients in the polarization equation are:

$$\alpha = \frac{1-c_I}{P_r}, \qquad \beta = \frac{3}{5}\frac{c_I^2}{P_r}, \qquad \lambda_0 = \frac{3}{5}\left(1+\frac{2}{3}a_0 P_r c_F\right),$$
$$\kappa = \frac{3}{5}a_0\left(1-\frac{c_I}{3}\right) \qquad \Gamma_0 = \frac{1}{10}\left(\frac{\epsilon}{\ell}\right)^2\frac{c_I}{P_r} - \frac{a_0}{15}P_r c_F \qquad \Gamma_2 = -\frac{a_0}{420}P_r c_F. \tag{9.43}$$

Importance of coefficient $c_F$ can be understood looking at normalized version of solvent equation:

$$\nabla^2 \boldsymbol{u} = c_F\left[6c_I \mathbf{P}\cdot\nabla\mathbf{P} + \nabla^2\mathbf{P} + \frac{1}{28}\nabla^4\mathbf{P}\right] + \nabla p_{eff}. \tag{9.44}$$

Here $c_F$ multiplies all terms depending on polarization: it means that, if $c_F \ll 1$ (for example, in the case of large effective viscosity, possible in very dense suspensions), the solvent fluid is not significantly affected by microswimmers motion. If also external forcing is not present, the solvent fluid will be (macroscopically) at rest ($\boldsymbol{u} = \boldsymbol{\Omega} = \boldsymbol{\Sigma} = 0$), and therefore dynamics of polarization $\mathbf{P}$ is decoupled from the solvent. In this case, equation (9.42b) reduces to the standard TTSH model.

A further extension of this model was proposed in [187], where the presence an external field affecting the polarization field was considered. At 2022 [187] and [188] (a work focused on comparison with experiments) remain the only application of this two-fields model. A mathematical analysis of the extended model was also performed in [189]

## 9.3 General phenomenology

Since its introduction in 2012, [123] the TTSH model has been subject to numerous studies which highlighted its rich phenomenology. In this section, a brief review of existing literature is present.

### 9.3.1 Mesoscale turbulence

The first regime described is the so called mesoscale turbulence. It is a isotropic and homogeneous state, emerging directly from the instability of

the disordered state, characterized by the presence of many vortices with fixed spatial length (the $\Lambda$ scale of the instability), which move chaotically. This was exactly the state for whose simulation the TTSH model was first proposed in 2012 (see figure 9.5). A study from 2013 [183] showed that a similar state can be observed (and simulated) also in 2D slice of 3D systems (at 2022 it remains the only study about TTSH model in three dimensions). In simulations, this state is obtained with $\lambda_0$ around 3.5 (the value commonly adopted) and values of alpha that go from positive (but lower than threshold value $\alpha_s$ in order to have the instability of uniform state) to slightly negative. It is important to notice that changing the value of $\alpha$ causes some quantitatively changes in the flow, but many qualitatively features are maintained.

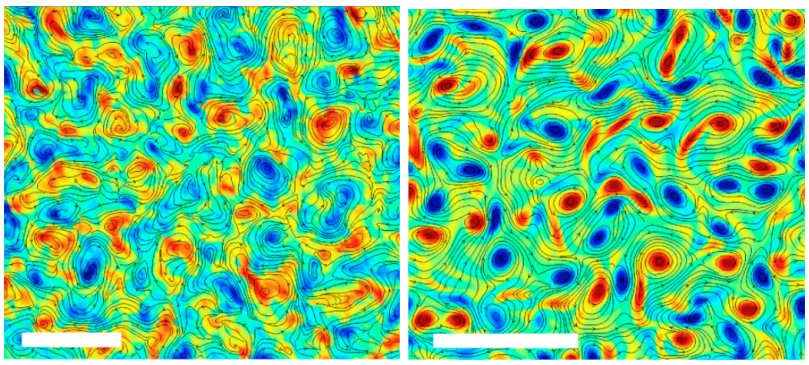

**Figure 9.5:** Flow streamlines and vorticity fields from quasi-2D *B. subtilis* suspensions (*left*) and from 2D simulations of TTSH model (*right*). [123]

Here, the term *mesoscale* is due to the fact that these structures are not on a macroscopic scale ($\Lambda \sim 20-50\mu m$), but they are still an order of magnitude greater than single swimmers. The (qualitatively) turbulent-like behaviour, but also its differences from "real" fluid turbulence, is visible from kinetic energy spectra (see figure 9.6). We can observe the presence of many active scales, but the power-laws are completely different from the $k^{-5/3}$ of Kolmogorovian turbulence. In particular, in the first paper about TTSH model, [123] it was observed a peak around $k = 0.1k_\ell$, where $k_\ell$ is the wavenumber corresponding to individual bacterial scale, (and therefore near $2\pi/\Lambda$), with a $k^{5/3}$ law on larger scales, and $k^{-8/3}$ on

smaller scales. However, further numerical studies [172,173,190] clarified that this power laws are not universal, but they depend (especially on larger scales) on the value of $\alpha$, and also that the peak position moves towards left (larger scales) with decreasing $\alpha$.

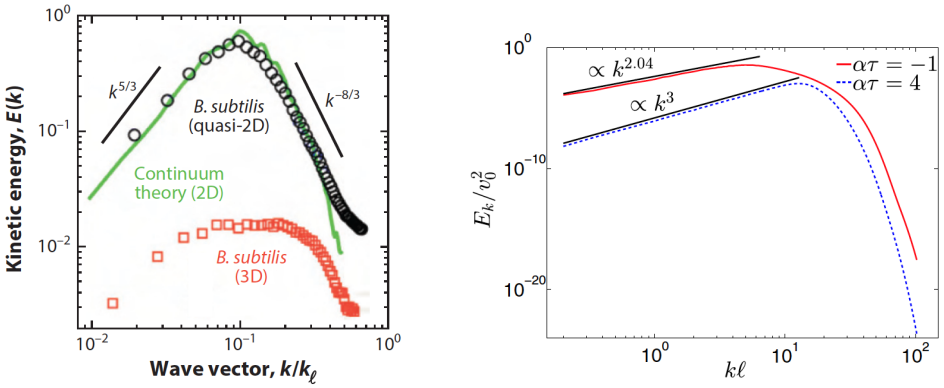


**Figure 9.6:** *Left*: kinetic energy spectra from 2D numerical simulations, compared to ones obtained by quasi-2D and 3D dense suspensions of *B. subtilis*. [123] *Right*: comparison between kinetic energy spectra obtained from numerical simulations with different values of $\alpha$. [172]

One of major differences between active and inertial turbulence is in the energy budget. One of the key features of high-Reynolds flow is the energy cascade (inverse in 2D, direct in 3D), corresponding to a range of scales with a constant energy flux, caused by advection term. [105] An investigation on energy budget in mesoscale turbulence was performed in [169,172]. If $E_k$ is the energy associated to Fourier mode $k$, its temporal evolution obeys to:

$$\partial_t E_k = 2\left(-\alpha - \Gamma_0 k^2 + \Gamma_2 k^4\right) E_k + T_k^{\mathrm{adv}} + T_k^{\mathrm{cub}}. \tag{9.45}$$

Linear terms are trivial: $\Gamma_0$ term injects energy around the scale $\Lambda$, while $\Gamma_2$ dissipates it at high-wavenumbers (small spatial scales). The $\alpha$ term injects or dissipates energy at all scales, according to its sign. The cubic non-linearity acts as a large scale friction, with a non-constant coefficient (proportional to total energy $E_{tot}$): it was shown in [172] that, in the stationary regime, the cubic term can be approximated as:

$$T^{\mathrm{cub}} \approx -8\beta E_{tot} E_k. \tag{9.46}$$

The advective non-linearity has a more complicated behaviour: it transfers energy from intermediate scales (near $\Lambda$, where the injection of energy due to $\Gamma_0$ is stronger) towards large scales (see fig. 9.7). This energy transfer is probably crucial in shaping the mesoscale state, since it explains how the spectrum peak can move at wavenumbers smaller than $2\pi/\Lambda$ when changing the value of $\alpha$ (and, from our simulations, the weight of advection term in energy budget is maximum in the transient from the linear instability to the stationary regime). But a constant (and stationary) energy (or enstrophy) flux lacks: we do not have an inertial range in bacterial turbulence. Absence of energy cascade is common to other forms of active turbulence, [191–194] as well as elastic turbulence. [26]

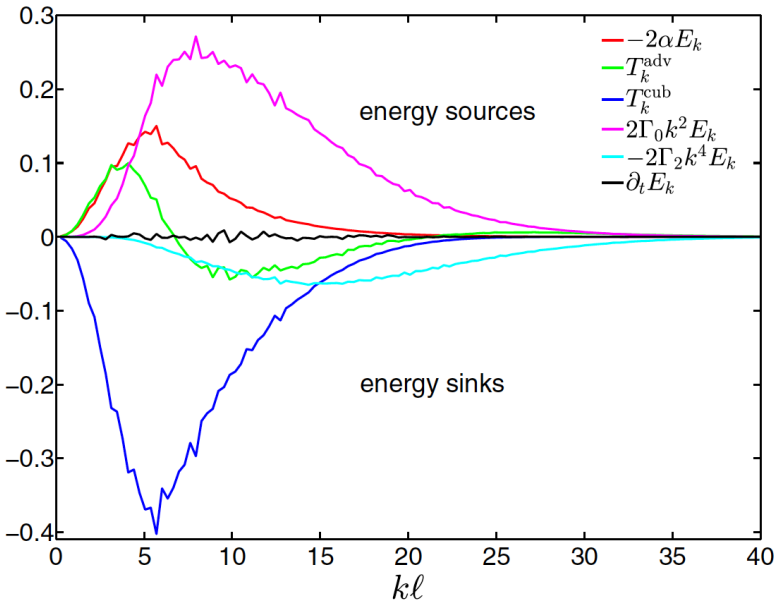


**Figure 9.7:** Spectral contributions to energy budget in the stationary mesoscale turbulent state, with $\alpha < 0$. The $\Gamma$ coefficients here are defined with opposite sign. *Image taken from* [172].

Probably, the more noticeable differences caused by changing the value of $\alpha$ (still in mesoscale turbulence regime) are observed in velocity and vorticity distributions, as it was highlighted in the paper. [173]. Using the normalization B, they compared the flow at $\alpha = 4$ (low energy) with the one at $\alpha = -1$ (high energy), and they found that, while at low energy

we have distributions that are almost Gaussian (especially the velocity), at high energy the velocity distribution is still close to Gaussian (but with relevant sub-Gaussian tails) and the vorticity one is strongly not-Guassian, even at its center (see figure 9.8).

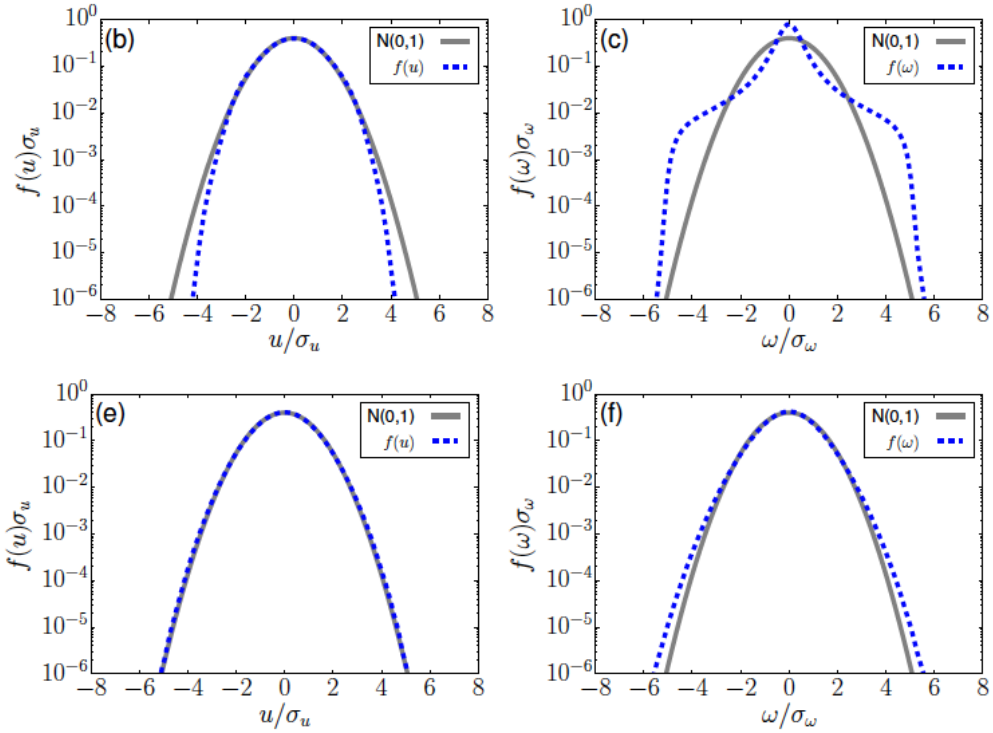


**Figure 9.8:** Velocity $u$ (left) and vorticity $\omega$ (right) distributions in the mesoscale turbulence regime computed and compared to Gaussian ones in [173]. *Top*: high energy ($\alpha < 0$) regime, *bottom*: low energy ($\alpha > 0$) regime.

Finally, several works [173, 174, 190, 195, 196] investigated Lagrangian properties of mesoscale turbulence, simulating the transport of tracer (point-like) particles, which dynamics is simply given by:

$$\frac{d\boldsymbol{x}_i(t)}{dt} = \boldsymbol{u}\left(\boldsymbol{x}_i(t), t\right). \tag{9.47}$$

All these papers agree on the fact that, if we compute the mean-squared displacement (MSD) of a large ensemble of particles:

$$\langle \Delta x^2 \rangle (t) = \frac{1}{N} \sum_{i=1}^{N} \left[\boldsymbol{x}_i(t_0 + t) - \boldsymbol{x}_i(t_0)\right]^2, \tag{9.48}$$

we have, for small $t$, a ballistic behaviour (*i.e.* $\langle \Delta x^2 \rangle \propto t^2$), while for large $t$ we can observe a diffusive trend (*i.e.* $\langle \Delta x^2 \rangle \propto t$). This behaviour is qualitatively identical at various $\alpha$, but the crossover time $\tau_c$ between ballistic and diffusive region shows a non-monotonic dependence in $\alpha$, with a minimum in $\alpha = 0$ (see figure 9.9). Transition from the diffusive to super-diffusive behaviour at large $\alpha$ is indeed one of the signals which indicate the transition to a different regime than the mesoscale turbulence. [174, 195]

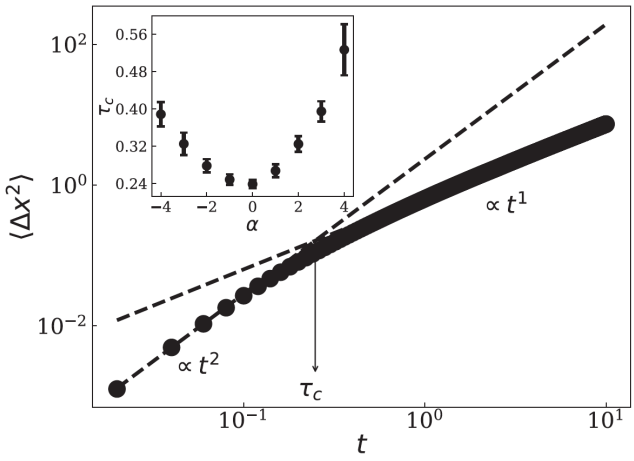


**Figure 9.9:** Mean-squared displacement of passive tracers in mesoscale turbulence regime. In the inset the non-monotonic dependence of crossover time $\tau_c$ in $\alpha$ is shown. *Image taken from* [190].

### 9.3.2 Stationary square lattice

Mesoscale turbulence emerges because of self-advection term, that chaotically "mixes" the structures generated by linear instability of the disordered state. For this reason, if we "shut off" this term setting $\lambda_0 = 0$, we obtain a regular state, composed by square vortices, with wave number $k_c = 2\pi/\Lambda$ and amplitude proportional to $\sqrt{(1-\alpha)/\beta}$ and $k_c$ (as it was shown in [169]). In this case, we simply have a classical phenomenon of pattern formation, described by a Swift-Hohenberg-like equation. A recent numerical work [197] demonstrates that this state is stable also for $\lambda_0 \neq 0$ under a certain threshold (depending on $\alpha$) $\lambda^\star$, and investigates

the transition between the stationary lattice and the mesoscale turbulence. In particular, they observed a qualitatively change in transport properties of Lagrangian tracers: for $\lambda_0 < \lambda^\star$ particles are trapped into closed loops, while for $\lambda_0 > \lambda^\star$ they are advected in irregular trajectories. Quantitatively, after the ballistic region, the MSD remains almost constant in the first case, not exhibiting the diffusive behaviour of the second case (see figure 9.10)

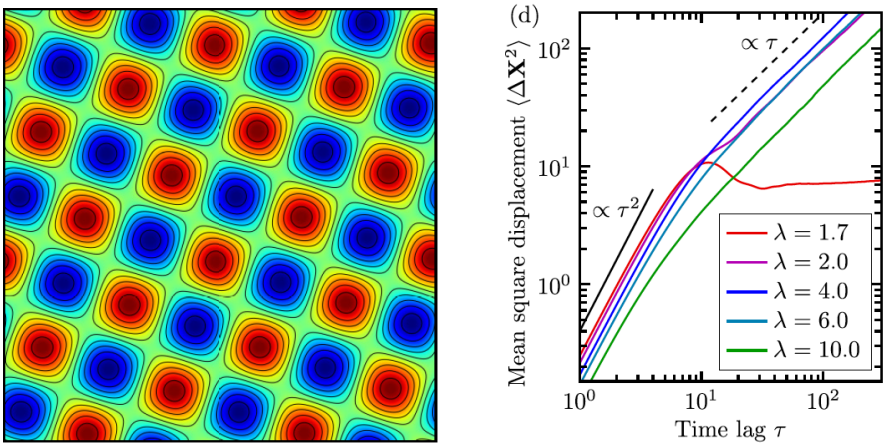


**Figure 9.10:** *Left*: flow streamlines and vorticity field in the stationary square lattice state. *Right*: mean-squared-displacement of Lagrangian tracers below and above the transition from stationary lattice to mesoscale turbulence. *Both images taken from* [197].

### 9.3.3 Active vortex lattice

Increasing the self-advection to very strong values it is possible to observe the emergence of another forms of vortex lattice, but very different from the stationary one previously described. In particular, there are two different forms of active vortex lattice (AVL) that have been simulated with the TTSH model: the spontaneous one, and the weakly constrained one.

The spontaneous AVL is a state observed for $\lambda_0 \gtrsim 6$ (with small $\alpha$ friction) in periodic domains without obstacles, originally announced in [169] and analyzed in details in [198]. This regime (until now) has not been observed in bacterial suspensions, but it shows similarities with a state

observed in sperm cells suspensions. [199] It was found that, with extreme strength of self-advection, the mesoscale turbulent state, where vortices with opposite handedness coexist, is not stable. After a long time transient, the system spontaneously break the vortices symmetry: one sign of vorticity prevails, resulting in a regular triangular lattice of same-sign vorticity, surrounded by a "sea" of opposite vorticity. In the case of a very large domain, this spontaneous symmetry breaking (SSB) is not uniform, with the establishment of clusters with opposite sign (and also different lattice orientation), separated by small boundaries of mesoscale turbulence. It is important to notice that this state is very different from the stationary square lattice, also because its wavelength is not the one ($\Lambda$) predicted by linear stability analysis, but it is greater than it (on the order of $1.7 - 1.8\Lambda$), and it slightly depends on intensity of the $\alpha$ friction.

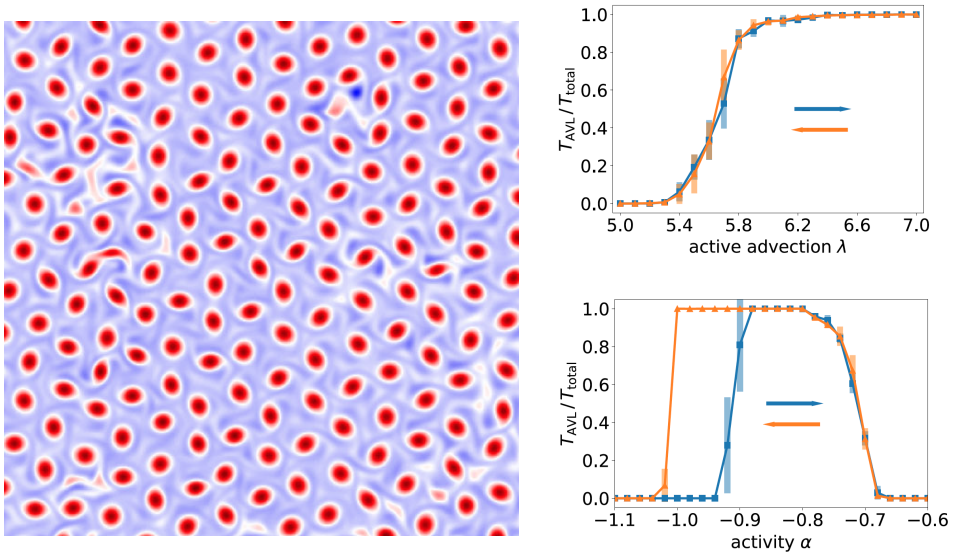


**Figure 9.11:** *Left*: snapshot of the vorticity field in the spontaneous active vortex lattice phase. *Right*: Transition from the AVL to the turbulent state (and vice versa), parametrized by the ratio between time spent in the AVL phase and the total time, changing the parameter $\lambda_0$ (top) or the parameter $\alpha$. In the first case we have coexistence, in the second (in the left side) hysteresis. It is important to notice that the parameter $\alpha$ here defined corresponds to our $\alpha - 1$.*Images taken from* [198]

This state does not exist if the friction due to the $\alpha$-term is too strong, but also if it is too weak (the boundary value, depending on $\lambda_0$, is close

to the change of sign of $\alpha$). It it interesting to notice that the transition mechanism between the turbulent and the AVL phase depends on the fact we change $\lambda$ or if we change $\alpha$. In the first case, we have a region of coexistence between the two phases, with the system that intermittently switches between turbulence and AVL. In the second one, we have hysteresis: if we go from AVL to turbulence, the transition value of $\alpha$ is different from the value necessary to go from turbulence to AVL. These behaviours can be quantified by the ratio between the time spent in the AVL phase and the total time (see figure 9.11).

The weakly constrained AVL has quite different features. In this case, we still have a periodic domain, but also a periodic array of small obstacles, which can alter significantly the dynamics of the system. A combined experimental-numerical study of 2020 [170] investigated the effect of small pillars (which occupy only a negligible fraction of the domain) disposed in various typologies of lattices, having wavelength comparable to $\Lambda$. In this paper, the authors found that, around an optimal lattice constant, the mesoscale turbulent state is stabilized into a regular pattern. In particular, in the case of Kagome lattice (fig. 9.12), another case of spontaneous symmetry breaking was observed: the emergence of a net rotational flow around the arrangement of pillars, thus breaking the mirror symmetry of the lattice (with both the configurations equiprobable). In this case, there is the emergence of a vortex pattern composed by six small vortices rotating in the same direction, surrounded by six larger vortices rotating in the other one. In a subsequent (only numerical) paper of 2022 [171], focused about square lattices, the authors associated to every elementary cell of the grid a $\pm 1$ value, according the sign of the mean vorticity computed in that cell, in order to map the system in an antiferromagnetic spin model. Using standard instruments from statistical mechanics (like order parameters and correlation functions), they showed a transition from an ordered "antiferromagnetic" phase to a disordered phase, for $\lambda_0 \gtrsim 9$, and especially that this phenomenon corresponds to a second-order phase transition, in the same class of universality of the Ising model, with $\lambda_0$ having the role of an effective temperature.

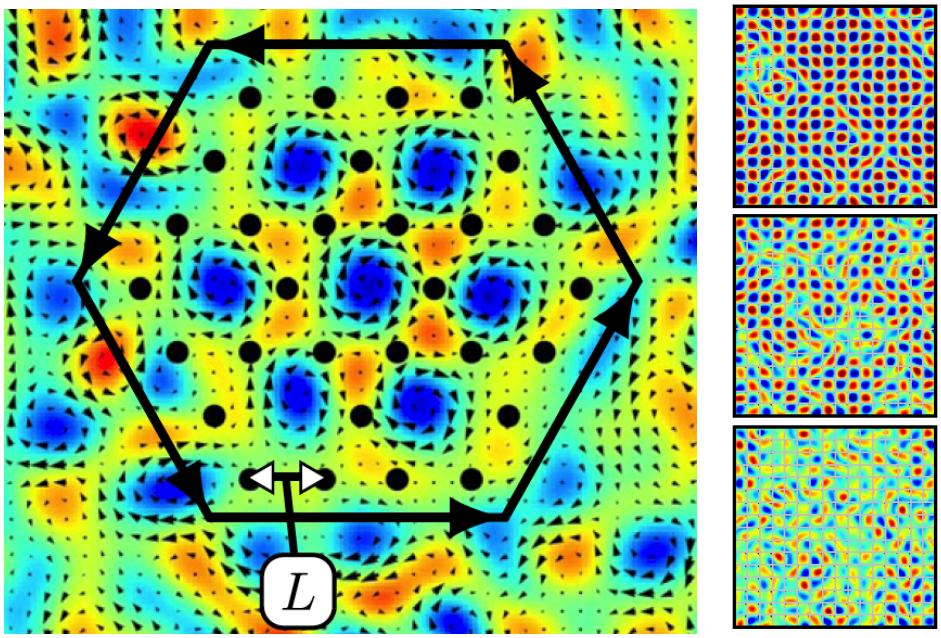


**Figure 9.12:** *Left*: flow streamlines and vorticity field in Kagoma lattice, with highlighted the closed loop having non-zero net circulation (black circles correspond to pillars). [170] *Right*: transition from ordered ferromagnetic phase to disordered phase at increasing $\lambda_0$, in a square lattice arrangement. [171]

### 9.3.4 Flocking turbulence

As in the Toner-Tu model, having $\alpha < 0$ means having a net polar aligning interaction between swimmers, which should lead to a polar state, a manifestation of flocking. But in the TTSH model we have also the destabilizing effect due to $\Gamma_0 < 0$, which not only destabilizes the uniform polar state, but it "tries" to suppress every attempt to flocking. This is the reason why the mesoscale turbulent state is stable also at moderate negative $\alpha$, with most all its properties qualitatively unchanged compared to positive $\alpha$. In the supplementary of [123], a criterion was proposed. We can define two different time scales, related to Landau potential and Swift-Hohenberg operator:

$$\tau_\alpha = -\frac{1}{\alpha}, \qquad \tau_\Gamma = \frac{|\Gamma_2|}{\Gamma_0^2}, \tag{9.49}$$

and therefore their ratio will be an (very approximate) indication of which term will prevail. We expect that the isotropic mesoscale state will be

unstable if:

$$\frac{\tau_\alpha}{\tau_\Gamma} \lesssim 1, \qquad \Longrightarrow \qquad -\alpha \gtrsim \frac{\Gamma_0^2}{|\Gamma_2|}. \tag{9.50}$$

As we will see in Chapter 10, this is a very crude estimate, which overestimates the value of $\alpha$ necessary to cause qualitative changes in the flow properties. As observed in [174, 195, 200], when the $\alpha$ forcing is relevant we can notice a modification in fluid structures, in particular filaments (defined by authors *vorticity streaks*) emerge next to usual vortices, and some vortices appear to be more dominant than others. Apparently, the domain is now divided in regions where the system is locally flocking, characterized by polar order (so, where the Landau potential is dominating), and regions with mesoscale turbulence (where the Swift-Hohenberg operator suppresses the flocking tendency). These regions (both of them) are not steady, instead they move and deform chaotically.

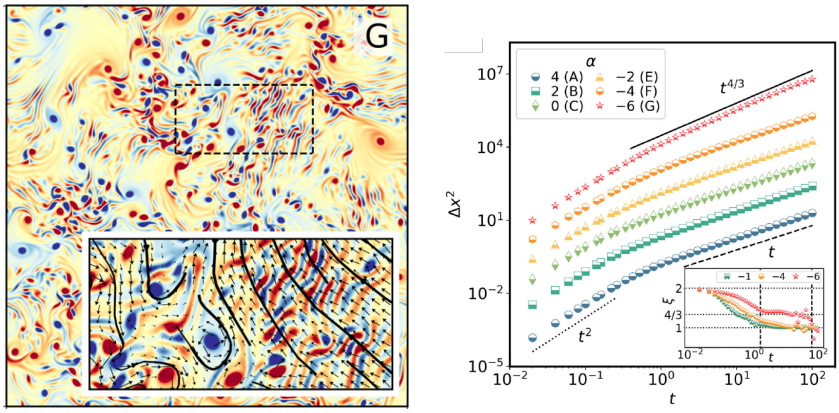


**Figure 9.13:** *Left*: vorticity field in the flocking turbulence regime. *Right*: transition from diffusive to superdiffusive behaviour in the transport of Lagrangian tracers (normalization B of $\alpha$ coefficient). *Images taken from* [174]

An important feature of this different regime is the observation of anomalous diffusion in the transport of Lagrangian particles: at large times, we have $\Delta x^2 \propto t^{4/3}$ [174]. Later investigations showed that this phenomenon is probably due to the fact that these streaky regions advect tracers much farther than the vortical regions. [195] Eulerian properties of this regime will be the subject of our investigation in chapter 10.

# Chapter 10

# From homogeneous to flocking turbulence

## 10.1 Introduction

As we have seen in the previous chapter, in the TTSH model the linear stability analysis [178] predicts that the regime of uniform flocking (which is present in the original Toner-Tu model) is destabilized by the Swift-Hohenberg operator, and therefore it cannot observed in the TTSH model. Nonetheless, recent works [174, 195, 200]. have shown that, if the aligning potential is sufficiently strong, the TTSH model displays the emergence of an inhomogeneous regime characterized by the presence of large-scale, isolated vortices, surrounded by regions of small vortices and elongated vortical structures, called vorticity streaks.

In this chapter, a detailed investigation of the inhomogeneous regime of large-scale vortices is presented. We show that these structures originate from local attempts to organize the flow in configurations of circular flocking induced by the aligning potential. The interactions between the flocking vortices give rise to a regime that we call *flocking turbulence*. By means of an extensive exploration of the parameter space we highlight the importance of the interplay between the Landau force and the nonlinear advection term to induce the transition from the regime of isotropic mesoscale turbulence towards the regime of flocking turbulence.

## 10.2 Model and numerical methods

The Toner-Tu-Swift-Hohenberg (TTSH) model describes the effective dynamics of a dense suspension of elongated pusher-like microswimmers as a polar active fluid, governed by an incompressible Navier-Stokes-like equation for the coarse-grained collective velocity field $\boldsymbol{u}$:

$$\partial_t \boldsymbol{u} + \lambda_0 \boldsymbol{u} \cdot \boldsymbol{\nabla} \boldsymbol{u} = -\boldsymbol{\nabla} p - (\alpha + \beta |\boldsymbol{u}|^2 + \Gamma_0 \nabla^2 + \Gamma_2 \nabla^4) \boldsymbol{u} \, . \tag{10.1}$$

The pressure term $\boldsymbol{\nabla} p$ ensures the incompressibility of the flow, $\boldsymbol{\nabla} \cdot \boldsymbol{u} = 0$, since in dense suspensions one can neglect density fluctuations. The coefficients $\lambda_0, \alpha, \beta, \Gamma_2, \Gamma_4$ are phenomenological parameters related to the properties of the microswimmers, the surrounding fluid and their interaction (see also Chapter 9).

Equation (10.1) is numerically integrated by a standard pseudo-spectral method in the vorticity-velocity formulation with a 1/2 dealising for the cubic nonlinearity, and a 4th order Runge-Kutta time stepping. Confinement in a circular domain is imposed by the penalization method [201, 202], which consists in modelling the region outside the domain as a porous medium with vanishing permeability. To this aim, the term $-\frac{1}{\tau}\mathcal{M}(\mathbf{x})\mathbf{u}$ is added to (10.1), where $\tau$ is the permeability time and the mask field $\mathcal{M}(\mathbf{x})$ is equal to 0 and 1 respectively inside and outside a circular domain of radius $R$ [203].

We performed two main sets of simulations. In the first we fix $\lambda_0 = 3.5$ and vary both $R = \{16, 23, 32, 63\}\Lambda$ and $\alpha = \{-0.25, -0.50, -0.75, -1.00, -1.25, -1.50, -1.75, -2.00\}$, while in the second set we fix both $\alpha = -1.00$ and $R = 63\Lambda$, and vary $\lambda_0 = \{2.0, 2.5, 3.0, 3.5, 4.0, 4.5, 5.0, 7.0\}$. An additional set of 269 simulations was performed with $\lambda_0 = 3.5$, $\alpha = -1.50$ and $R = 16\Lambda$ in order to study the transition time to the circular flocking state. The domains with radius $R = 63\Lambda$, $R = \{31, 23\}\Lambda$ and $R = 16\Lambda$ are embedded in squared periodic domains of size $L = \{160, 80, 40\}\Lambda$ with numerical resolutions $N = \{2048, 1024, 512\}$ respectively. In all the simulations the values of the other parameters are fixed as follows: $\beta = 0.01$, $\Gamma_0 = 2$, $\Gamma_2 = 1$. The characteristic scale is $\Lambda = 2\pi$. The permeability time of the penalization term is $\tau = 0.001$.

We identify vortices by means of the standard Okubo-Weiss parameter [204,205] $\mathcal{Q} = \left(\partial^2_{xy}\psi\right)^2 - \left(\partial^2_x\psi\right)\left(\partial^2_y\psi\right)$, where $\psi$ is the stream function (i.e. $\boldsymbol{u} = (\partial_y\psi, -\partial_x\psi)$ and $\omega = -\nabla^2\psi$ is the vorticity). $\mathcal{Q} < 0$ corresponds to vortical regions, while $\mathcal{Q} > 0$ to regions dominated by shear. Vortices are defined as connected regions of the space where $\mathcal{Q} \leq -\mathcal{Q}^\star$ and the threshold value $\mathcal{Q}^\star$ is chosen as 3 times the root mean squared (rms) value of the $\mathcal{Q}$ field. We checked that our results do not depend on the precise value of $\mathcal{Q}^\star$. We remark that the Okubo-Weiss criterion has been already used in TTSH simulations for the study of Lagrangian properties [195, 196].

## 10.3 Transition towards flocking turbulence

In order to study the effect of the intensity of the aligning potential on the dynamics of the system, we performed a first set of simulations varying the strength of the Toner-Tu term in the range from $\alpha = -0.25$ to $\alpha = -2$. In all the simulations, the initial condition is a vanishing velocity field, with a small random perturbation.

The early stage of the evolution of the system is driven by the linear term $\mathcal{L}\mathbf{u} = -\alpha\mathbf{u} - \Gamma_2\nabla^2\mathbf{u} - \Gamma_4\nabla^4\mathbf{u}$ and it is characterized by an exponential growth of the rms values of the velocity and vorticity, in agreement with the predictions of the linear stability analysis [177]. This phase ends when the nonlinear terms become relevant. The cubic dumping term of the Laudau force arrests the exponential growth and the self-advection term destabilizes the stationary pattern created by the Swift-Hohenberg term, thus inducing a mesoscale turbulence state [197]. This regime is characterized by an homogeneous, disordered population of small vortices (see Fig. 10.1 top). The vortices are uniformly distributed in the circular domain, with a high vortex number density $n$ (defined as the number of vortices per unit area).

For moderate negative values of $\alpha$ ($-1 \lesssim \alpha < 0$) the regime of mesoscale turbulence is statistically stable: once the system reaches it, it remains there forever. This is confirmed by the temporal evolution of the

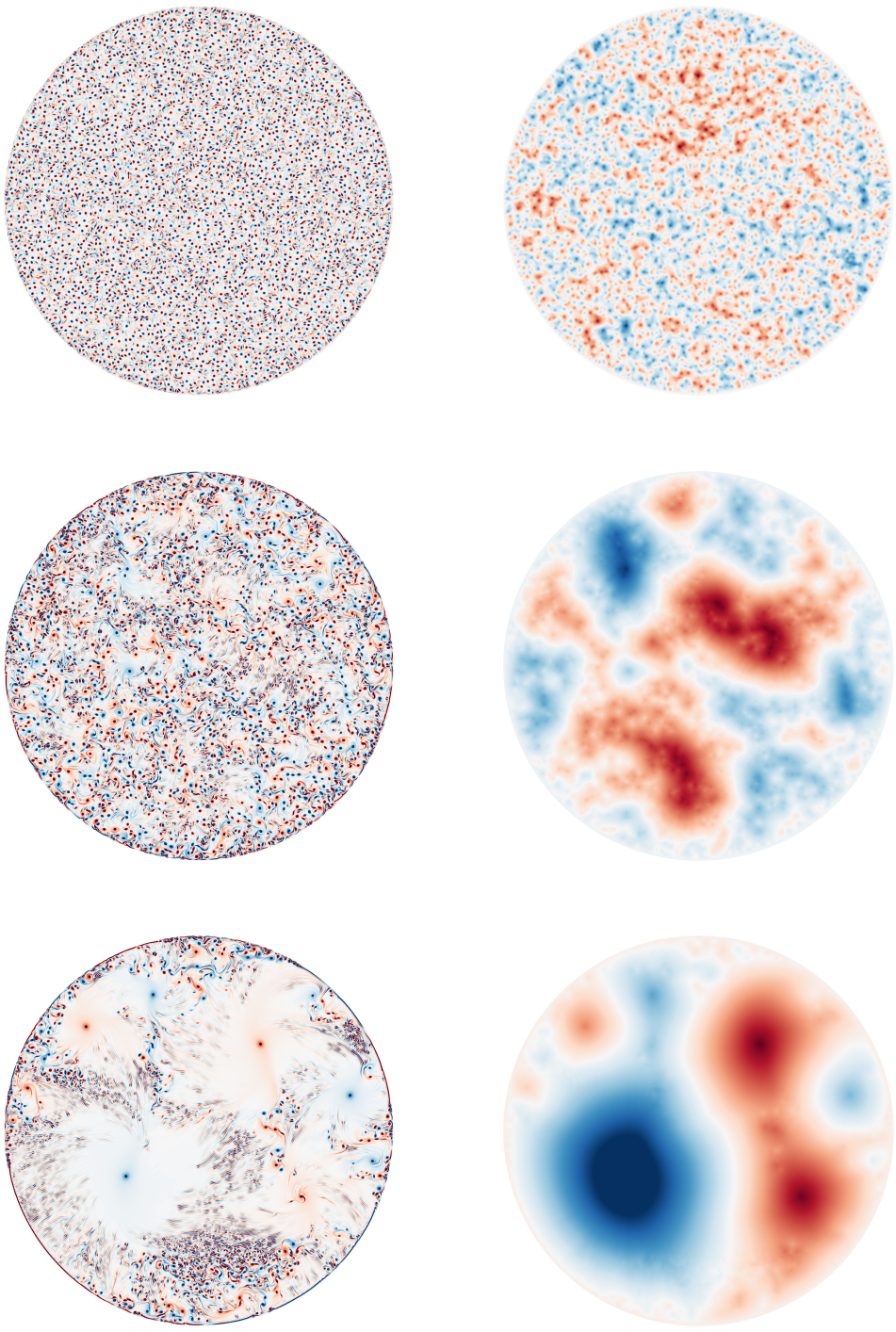

**Figure 10.1:** Vorticity fields $\omega$ (left) and stream function $\psi$ (right), in the stationary regimes of the simulations with $\alpha = -0.25$ (top), $\alpha = -1.00$ (center) and $\alpha = -1.75$ (bottom). Here $\lambda_0 = 3.5$ and $R = 63\Lambda$.

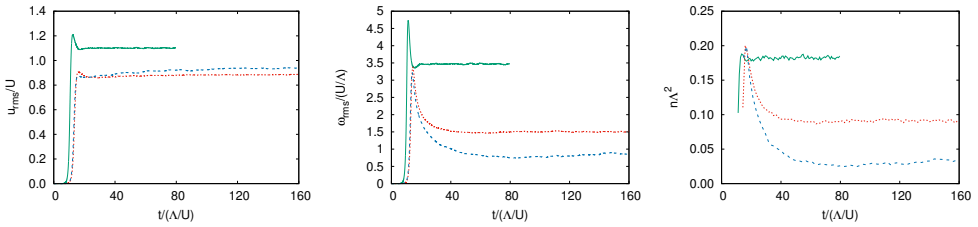


**Figure 10.2:** Time evolution of the rms velocity $u_{rms}$ (left), rms vorticity $\omega_{rms}$ (center) and vortex density $n$ (right) in the numerical simulations with $\alpha = -0.25$ (green solid line), $\alpha = -1.00$ (red dotted line) and $\alpha = -1.75$ (blue dashed line). Here $\lambda_0 = 3.5$ and $R = 63\Lambda$.

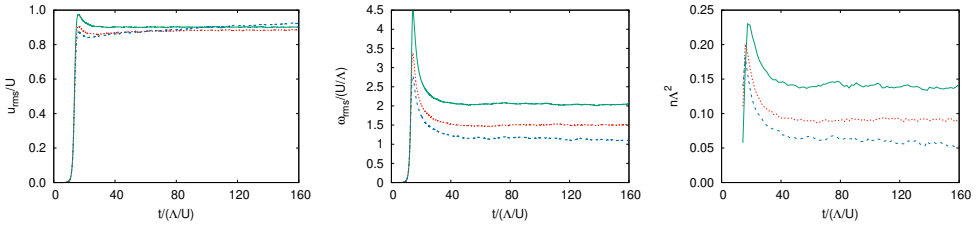


**Figure 10.3:** Time evolution of the rms velocity $u_{rms}$ (left), rms vorticity $\omega_{rms}$ (center) and vortex density $n$ (right) in the numerical simulations with $\lambda_0 = 2.0$ (green solid line), $\lambda_0 = 3.5$ (red dotted line) and $\lambda_0 = 5.0$ (blue dashed line). Here $\alpha = -1.00$ and $R = 63\Lambda$.

rms velocity $u_{rms}$, rms vorticity $\omega_{rms}$, and vortex density $n$, which remain stationary in time (after the initial transient) as shown in Fig. 10.2).

For $\alpha = -1$ the regime of uniform mesoscale turbulence is not stable anymore. It undergoes a slow evolution during which the number of vortices diminishes (see Fig. 10.2 left). The decrease of the vortex density is accompanied by a simultaneous decrease of the rms vorticity, which suggests that the average vorticity of each individual vortex remains almost constant in time. At long times ($t > 50\Lambda/U$), the system achieves an inhomogeneous, statistically steady state, characterized by the presence of isolated vortices and elongate filaments called vorticity streaks [174] (see Fig. 11.1 center). The flow is organized in large-scale structures, which are evident in the stream function.

Increasing further the strength of the aligning potential (i.e. for $\alpha \lesssim -1$) the system evolves toward a strongly inhomogeneous state, composed by few large vortices (see Fig. 11.1 bottom). Each vortex is surrounded by a wide region of circular motion with constant speed $U = \sqrt{-\alpha/\beta}$. The

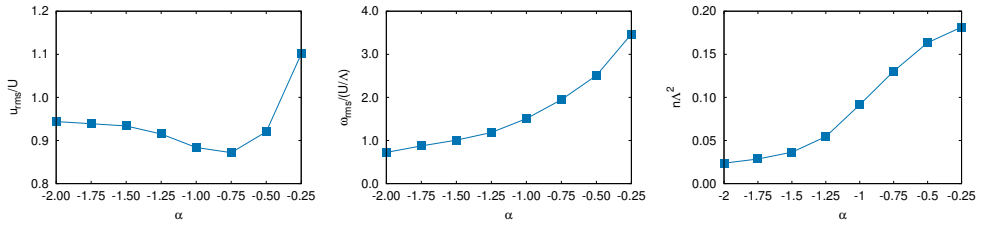


**Figure 10.4:** Asymptotic values of rms velocity $u_{rms}$ (left), rms vorticity $\omega_{rms}$ (center) and vortex density $n$ (right) as a function of $\alpha$ in the numerical simulations with $\lambda_0 = 3.5$ and $R = 63\Lambda$.

vorticity streaks are observed in the peripheral regions of these vortices, and they are preferentially aligned in the transverse direction with respect to the circular motion. The emergence of large-scale structures in the flow is clearly visible in the stream function. Local dense vortex clusters are still present between these structures and close to the boundary of the domain. During the evolution of the system toward this asymptotic state, we observe a decrease of the rms vorticity and vortices density (see Fig. 10.2), while the rms velocity increases slowly in time.

The formation of this state can be understood as follows. At large negative values of $\alpha$, the strong Landau force promotes the development of local attempt to organize the flow in states of circular flocking. This process occurs independently in different regions of the domain, producing large vortices with either positive or negative sign. The Swift-Hohenberg operator is not anymore capable to suppress completely the flocking tendency of the system, but it is still able to destabilize the peripheral regions of the vortices. Indeed, linear stability analysis of a global polar state predicts the appearance of a transverse pattern with respect to the mean flow with wavelength $\Lambda$ [177]. The streaks observed in Fig. 10.1 bottom) correspond to this pattern, distorted by the advection produced by the other vortices. Since this regime is characterized by the chaotic interaction between the flocking vortices, we call it *flocking turbulence*.

The non-linear self-advecting term $\lambda_0 \boldsymbol{u} \cdot \boldsymbol{\nabla u}$ plays a crucial role in the development of the flocking turbulence. To address this issue, we performed a second set of simulations keeping fixed $\alpha = -1$ and varying

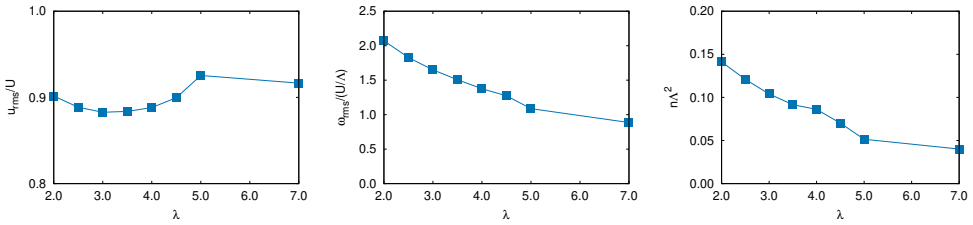


**Figure 10.5:** Asymptotic values of rms velocity $u_{rms}$ (left), rms vorticity $\omega_{rms}$ (center) and vortex density $n$ (right) as a function of $\lambda_0$ in the numerical simulations with $\alpha = -1.00$ and $R = 63\Lambda$.

$\lambda_0$ in the range from 2 to 7. The temporal evolution of the rms velocity, vorticity and vortex density is shown in Fig. 10.3 for three different values of $\lambda_0$. While the rms velocity is almost unaffected by the change of $\lambda_0$, the rms vorticity and vortex density reach different asymptotic values which decrease at increasing $\lambda_0$. This is qualitatively similar to what observed at increasing the intensity of $|\alpha|$ (see Fig. 10.2).

The dependence of the asymptotic, stationary values of rms velocity, vorticity and vortex density as a function of the parameter $\alpha$ and $\lambda_0$ is shown in Figs. 10.4 and 10.5 respectively. The transition from the two regimes of mesoscale and flocking turbulence is evident in the dependence of the $u_{rms}$ on $\alpha$. In the regime of flocking turbulence, at large negative values of $\alpha$ the ratio between $u_{rms}$ and $U = \sqrt{-\alpha/\beta}$ is almost constant, meaning that $u_{rms}$ grows proportionally to $\sqrt{|\alpha|}$. Conversely, at small values of $\alpha$ the ratio $u_{rms}/U$ increases, in agreement with the results of previous studies of the mesoscale turbulence regime [190]. We find that $u_{rms}$ is almost independent of $\lambda_0$. This is consistent with the observation that the self-advection term conserves the energy, and therefore the value of $\lambda_0$ is not expected to affect the energy balance.

Both the rms vorticity and the vortex density decrease by increasing the magnitude of $|\alpha|$, in agreement with the qualitative observation that the number of vortices decreases as shown in Fig. 10.1. A similar behaviour is observed also by increasing the strength of the self-advection: Larger values of $\lambda_0$ correspond to lower $\omega_{rms}$ and $n$. The above results suggest that the transition from mesoscale turbulence to flocking turbulence

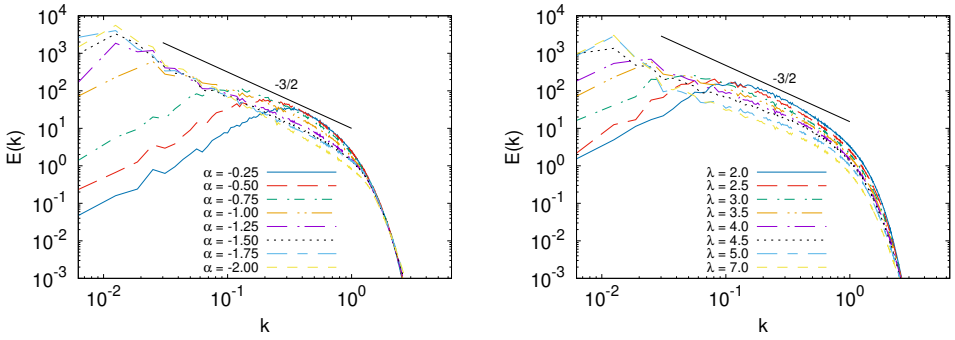


**Figure 10.6:** Kinetic energy spectra, averaged in the stationary regimes of the simulations with fixed $\lambda_0 = 3.5$ (left) and fixed $\alpha = -1.00$ (right). Here $R = 63\Lambda$.

is not solely due to the increase of the strength of the aligning potential $\alpha$, but it requires also a strong enough self-advection (i.e. non-linearity).

Further insights on this transition are given by the distribution of kinetic energy among different spatial scales, which is quantified by the energy spectrum $E(k)$, shown in Fig. 10.6. In the mesoscale turbulence regime, $E(k)$ is peaked around a characteristic wavenumber $k_{max} \simeq 2\pi/\Lambda$, Increasing the energy input (i.e. increasing the magnitude of $|\alpha|$) the peak of the spectrum shifts towards smaller wavenumbers $k_{max} < 2\pi/\Lambda$, in agreement with previous findings [172, 173, 190].

In the regime of flocking turbulence (for $|\alpha| \gtrsim 1$), we observe a qualitative change in the spectrum. The energy spectrum develops a power-law behaviour $E(k) \sim k^{-\delta}$ at intermediate wavenumbers $k_{max} \ll k \ll 2\pi/\Lambda$, with a spectral slope $\delta$ which is close to the theoretical value $\delta = 3/2$ predicted and observe in [200]. At large, negative values of $\alpha$ we observe a slight increase of the spectral slope $\delta$, which exceeds the value 3/2. At the same time, the wavenumber $k_{max}$ becomes almost constant and it is close to the smallest available wavenumber, i.e. the inverse of the size of the circular domain. As we will discuss in the next Section, these effects are due to the confinement.

Interestingly, we find that the decrease of peak of the energy spectrum $k_{max}$ and the development of the intermediate power-law behaviour is observed also at increasing the parameter $\lambda_0$ at fixed $\alpha$. This is a further clue that the transition from mesoscale to flocking turbulence is deter-

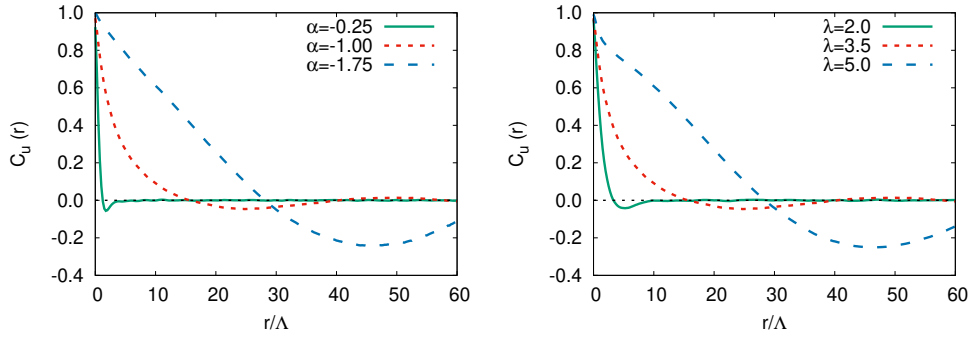


**Figure 10.7:** Autocorrelations functions of the velocity field $C_{\mathbf{u}}(r)$ in the stationary regimes of the simulations with fixed $\lambda_0 = 3.5$ (left) and fixed $\alpha = -1.00$ (right). Here $R = 63\Lambda$.

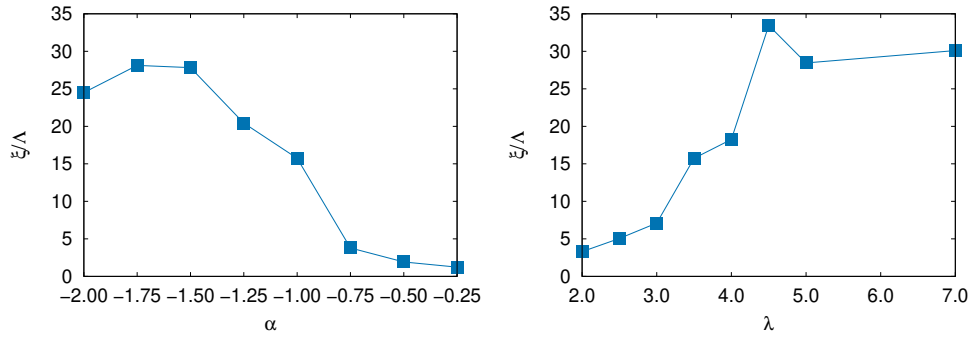


**Figure 10.8:** Velocity correlation length $\xi$, in the stationary regimes of the simularions with fixed $\lambda_0 = 3.5$ (left) and fixed $\alpha = -1.00$ (right). Here $R = 63\Lambda$.

mined by the interplay between the Landau force and the self-advection term.

The growth of the integral scale of the flow, signalled by the reduction of $k_{max}$, can be quantified by the analysis of the autocorrelation functions of the velocity field

$$C_{\boldsymbol{u}}(r) = \frac{\langle \boldsymbol{u}(\boldsymbol{x}) \cdot \boldsymbol{u}(\boldsymbol{x}') \rangle}{\langle |\boldsymbol{u}(\boldsymbol{x})|^2 \rangle}; \tag{10.2}$$

with $r = \|\boldsymbol{x} - \boldsymbol{x}'\|$, and angular brackets indicating average over space and time (in the stationary regime). We remark that correlation functions are a well established tool for the study of flocking phenomena [206].

The velocity autocorrelation function, plotted in Fig. 10.7, displays a negative minimum which allows to define a velocity correlation scale $\xi$ given by the first zero crossing of $C_{\boldsymbol{u}}$. The dependence of $\xi$ on the

parameters $\alpha$ and $\lambda_0$ is reported in Fig. 10.8. Both reducing $\alpha$ at fixed $\lambda_0$ and increasing $\lambda_0$ at fixed $\alpha$ we observe a sharp increase of $\xi$ from values comparable to $\Lambda$ to values of the order $30\Lambda$, which indicates the transition from the mesoscale regime to the flocking turbulence. At large values of $\Lambda$ and large negative values of $\alpha$ we also observe a saturation of the correlation scale to an asymptotic value $\xi \approx 30\Lambda$ which is comparable with the radius of the circular domain ($R = 63\Lambda$).

## 10.4 Role of confinement

The saturation of correlation length and of the peak of the energy spectrum $k_{max}$ reveals that the geometrical confinement of the bacterial turbulence influences significantly its dynamics. In this section we pursue the investigation of the effects of the confinement presenting the results of simulations of the TTSH model in circular domains at varying the radius $R$ of the domain.

In Figure 10.9 we show the temporal evolution of the rms velocity, vorticity and vortex density for a set of simulations in the regime of flocking turbulence with parameters $\alpha = -1.75$ and $\lambda_0 = 3.5$. The radius of the domain is varied from $R = 16\Lambda$ to $R = 63\Lambda$. Increasing the confinement, i.e. reducing $R$, we observe a decrease of the asymptotic values of $u_{rms}$ and an increase of $\omega_{rms}$ and $n$. This effects can be ascribed to the interactions of the flow with the no-slip boundary. The friction with the boundary dissipates part of the energy, thus reducing $u_{rms}$. Close to the boundaries, the energy dissipation is accompanied by the production of small vortices, which causes an increase of $\omega_{rms}$ and of the total number of vortices. These effects are stronger for the cases with smaller radius $R$, because of the larger ratio between the perimeter and the area of the domain.

In Fig. (10.10) we compare the asymptotic stationary values of $u_{rms}$, $\omega_{rms}$ and $n$ as a function of the domain size $R$, in the regime of mesoscale turbulence ($\alpha = -0.25$), in the transition regime ($\alpha = -1.00$) and in the regime of flocking turbulence ($\alpha = -1.75$). The parameter $\lambda_0 =$

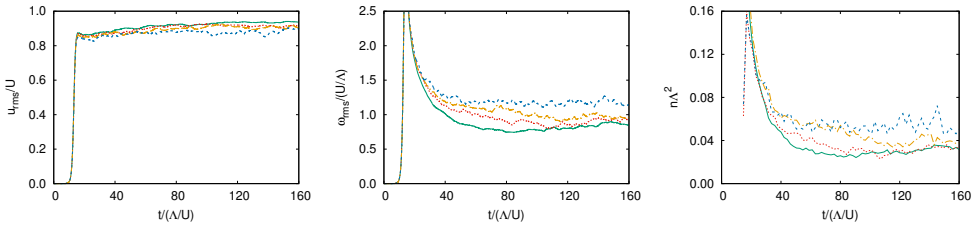


**Figure 10.9:** Time evolution of the rms velocity $u_{rms}$ (left), rms vorticity $\omega_{rms}$ (center) and vortex density $n$ (right) in the simulations with different values of confinement radius: $R = 63\Lambda$ (green solid line), $R = 31\Lambda$ (red dotted line), $R = 23\Lambda$ (orange dotted-dashed line) and $R = 16\Lambda$ (blue dashed line). Here $\alpha = -1.75$ and $\lambda_0 = 3.5$.

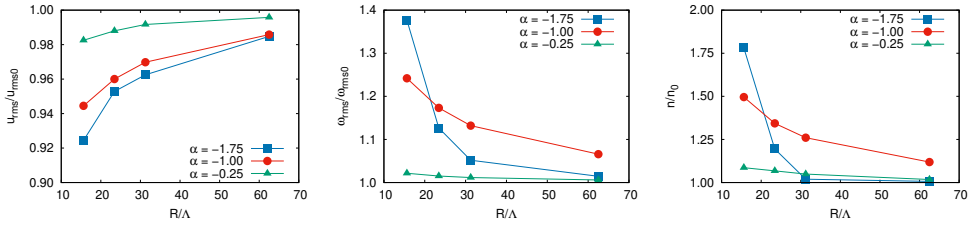


**Figure 10.10:** Asymptotic values of the rms velocity $u_{rms}$ (left), rms vorticity $\omega_{rms}$ (center) and vortex density $n$ (right) as a function of the confinement radius $R$. Here $\lambda_0 = 3.5$.

3.5 is fixed for all the simulations. The asymptotic values presented in Fig. (10.10) are normalized with the corresponding values $u_{rms0}$, $\omega_{rms0}$ and $n_0$ obtained in another set of simulations with identical parameters, performed in a large square domain with size $L = 160\Lambda$ and periodic BCs, which is the typical setup for the numerical studies of the TTSH model.

The effects of the confinement are qualitatively similar for all the regimes: Reducing $R$ we observe a reduction of $u_{rms}$ and an increase of $\omega_{rms}$ and $n$. Nonetheless, we observe significant quantitative differences. In the case of mesoscale turbulence ($\alpha = -0.25$) the values of $u_{rms}$, $\omega_{rms}$ and $n$ varies weakly with $R$ and they remains close to those of the simulations with periodic BCs. Conversely, the values obtained in the flocking turbulence regime displays a strong dependence on $R$.

The weak influence of the confinement on the mesoscale turbulence can be explained by the observation that in this regime the correlation length $\xi$ of the velocity field is approximately one order of magnitude smaller than $R$. Therefore the effects of the confinement are restricted to

a small region close to the boundary. In the intermediate case ($\alpha = -1$) the correlation length $\xi$ is larger than in the mesoscale turbulence (see Fig.10.8) and the effects of the confinement are stronger. In the flocking turbulence regime ($\alpha = -1.75$) the values of $u_{rms}$, $\omega_{rms}$ and $n$ change abruptly when the radius $R$ becomes smaller than the correlation length $\xi \approx 30\Lambda$.

The effects of the confinement manifest also in the energy spectra. In Fig. 10.11 we compare the spectral slope $\delta$ of the energy spectrum measured in simulations with different $R$ and $\alpha$. In the set of simulations with $\alpha = -1.25$ the slope is almost independent of $R$ and its value is close to the theoretical prediction 3/2 [200]. The independence of the spectra from $R$ is observed also for $\alpha > -1.25$ (not shown), which confirms that the effects of the confinement on the regime of mesoscale turbulence are weak.

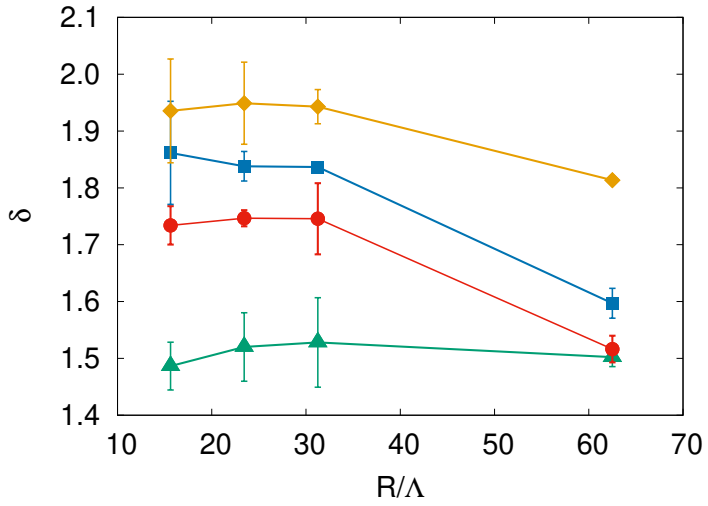


**Figure 10.11:** Spectral exponent $\delta$ as a function of confinement radius $R$, in the simulations with $\lambda_0 = 3.5$ and $\alpha = -2.00$ (orange diamonds), $\alpha = -1.75$ (blue squares), $\alpha = -1.50$, (red circles) and $\alpha = -1.25$ (green triangles).

In the regime of flocking turbulence the spectral slope $\delta$ varies significantly with $R$ and $\alpha$. Decreasing the radius $R$ we find that $\delta$ grows up to an asymptotic value which increases with $|\alpha|$. We argue that the steepening of the energy spectrum due to the confinement can be related

to some process of spectral energy condensation, i.e., of the accumulation of energy in the lowest mode accessible to the system, whose wavelength is comparable to the size of the domain. This explains the discrepancy between the slope of the energy spectra observed in our simulations and the results reported in [200]. The trend of the values of $\delta$ at increasing $R$ suggests the conjecture that the spectral slope attains an universal value $\delta = 3/2$ in the limit of unconfined, infinite domain.

## 10.5 Discussions

The data from our simulations, combined with the results reported in [200], suggest that, in the TTSH model, we have a transition between a homogeneous regime denoted as mesoscale turbulence to another one, with qualitatively different features, that we have called *flocking turbulence*. For moderate values of $\alpha$ we have smooth variations in quantitative properties of the system (position of the peak of energy spectra [172], crossover time in the transport of Lagrangian particles, [190] etc.), simply due to more energy inside the system, but going beyond a certain threshold $\alpha_c$, the real nature of the Landau forcing $(\alpha + \beta|\boldsymbol{u}|^2)\,\boldsymbol{u}$ appears, with consequent abrupt variations in the mean enstrophy, energy spectra and correlation functions. This term is not simply a forcing which injects energy into the system, but, since $\boldsymbol{u}$ represents also the order parameter of the system, it also induces a spontaneous symmetry breaking (SSB) in the velocity field, pushing all the swimmers to propel in the same direction with the same speed $U = \sqrt{-\alpha/\beta}$. Therefore, for $\alpha < \alpha_c$, in the system we can observe the formation of some large vortices (quite different from the small vortices in mesoscale turbulence) with constant speed $U$, which are nothing else than regions where the SSB happens in an independent way. If the dynamics of the system was driven only by the Landau terms, we would observe the transition at $\alpha_c = 0$, but in this model we have also the Swift-Hohenberg (SH) operator $(\Gamma_0\nabla^2 + \Gamma_2\nabla^4)\,\boldsymbol{u}$ which, if $\Gamma_0 > 0$, which always destabilizes the polar ordered state. [177]

Our study demonstrated that the self-advection term $\lambda_0\boldsymbol{u}\cdot\nabla\boldsymbol{u}$ plays an

important role in this transition. In particular, we find that the transition towards the flocking turbulence can be realized also keeping fixed $\alpha$ and increasing the strength of the self advection coefficient $\lambda_0$.

These observations can be rationalized by considering the time scales of the different terms of the TTSH model. The characteristic time scale of the Landau force $\tau_\alpha$, of the SH term $\tau_\Gamma$ and of the self-advection term $\tau_\lambda$ are:

$$\tau_\alpha = -\frac{1}{\alpha}, \qquad \tau_\Gamma = \frac{\Gamma_2}{\Gamma_0^2}, \qquad \tau_\lambda = -\frac{1}{\alpha\lambda_0} \,. \tag{10.3}$$

The expression of $\tau_\lambda$ follows from the consideration that, while the typical intensity of the velocity $U$ is determined by the Landau force, the velocity field in (5.1) is advected by the rescaled velocity $\lambda_0 U$. We note that for $\lambda_0 > 1$, (which corresponds to the case of pusher-like swimmers considered here), the self-advection time $\tau_\lambda$ is shorter that $\tau_\alpha$.

The transition from the mesoscale is expected to occur when $\tau_\Gamma \sim \min(\tau_\alpha, \tau_\lambda)$. Since we have $\tau_\lambda < \tau_\alpha$, the condition for the transition can be written as

$$\alpha\lambda_0 \sim -\frac{\Gamma_0^2}{\Gamma_2} \,. \tag{10.4}$$

Our prediction refines the criterion proposed in the Supplementary of [123], considering the role of self-advection. For fixed $\lambda_0 = 3.5$ the relation (10.4) give the critical value $\alpha_c \simeq -1.14$, while for fixed $\alpha = -1$ we get $\lambda_c \simeq 4$, which are both in quantitative agreement with our numerical findings. If we consider the normalization adopted in [200], we have $\alpha_c \sim -6.3$, close to the value $\alpha_c \sim -5$ they reported.

The crucial role of the self-advection coefficient $\lambda_0$ is not surprising, since, in other regions of the parameter space compared to those we have analyzed, it has been shown not only that varying $\lambda_0$ we have the transition from a stationary pattern to the chaotic mesoscale turbulence, [169, 197] but also the emergence of an out-of-equilibrium active vortex lattice [169, 198] or, in the presence of a periodic array of obstacles, the occurrence of an order-disorder second-order phase transition in the Ising universality class, with an effective temperature proportional to $\lambda_0$. [171] However, it is important to recall that the role of the self-advection in the TTSH model is quite different to the role of in the usual

Navier-Stokes equation, and that, despite some common features (like power-law energy spectra or intermittent behavior [200]), the classic high-Reynolds turbulence and the flocking turbulence regime we described are two very different phenomena (as well as forms of active turbulence in other systems [191–194]). The former is due to the inertia of the fluid, which, when it dominates over the viscosity, triggers the emergence of the energy cascade, *i.e.* a constant flux of energy across the scales of the system. The latter is caused by a spontaneous symmetry breaking of the system, where the self advection has the role to suppress the instabilities due to the SH term, and the energy is injected simultaneously on all the scales of the system.

# Chapter 11

# The giant vortex

## 11.1 Introduction

In the previous chapter we studied bacterial flocking turbulence in a confined domain, but this is a regime that we can observe also with periodic boundary conditions, which is only slightly affected by confinement. Nonetheless, it has been shown that in active fluids confining boundaries can induce the emergence of coherent structures, qualitatively different from the ones we can observe in periodic domains. [164, 207–209] In particular, considering experiments with bacterial suspensions, the confinement in circular micro-wells can induce the formation of a rectified vortex. [164, 210, 211] Here, by means of extensive numerical simulations of the TTSH model [123, 183] (see also Chapter 9), we show that geometrical confinement can induce the transition from the chaotic regime of flocking turbulence to a novel regime, characterized by the formation of a giant vortex surrounded by an annular region of elongated vorticity structures. We also highlight that this state has larger size and different velocity profile with respect to the vortical structures reported in previous studies [131, 164, 210] and that it originates from a different process which involves complex interactions between the chaotic flow and the boundaries.

## 11.2 Model and simulations

We modelled a dense bacterial suspension by mean of the TTSH model, where the coarse-grained collective velocity field $\boldsymbol{u}$ obeys to:

$$\partial_t \boldsymbol{u} + \boldsymbol{u} \cdot \boldsymbol{\nabla} \boldsymbol{u} = -\boldsymbol{\nabla} p - (\alpha + \beta |\boldsymbol{u}|^2 + \Gamma_0 \nabla^2 + \Gamma_2 \nabla^4) \boldsymbol{u} \, . \tag{11.1}$$

The pressure gradient $\boldsymbol{\nabla} p$ ensures the incompressibility of the flow, $\boldsymbol{\nabla} \cdot \boldsymbol{u} = 0$, which is valid for dense suspensions, and the parameters $\lambda_0, \alpha, \beta, \Gamma_0, \Gamma_2$ are determined by the properties of the microswimmers (more details in Chapter 9).

Numerical methods are the same adopted in Chapter 9: we integrated equation (11.1) in a two-dimensional circular domain of radius $R$, using a dealiased pseudospectral method, with an implicit Runge-Kutta scheme for time integration and a penalization term in order to implement the no-slip boundary conditions. Simulation parameters are reported in Table 11.1.

| | $R$ | $N^2$ | $\alpha$ |
|---|---|---|---|
| A1 | $16\Lambda$ | $512 \times 512$ | -2.00 |
| A2 | | | -1.75 |
| A3 | | | -1.5 |
| A4 | | | -1.25 |
| B1 | $23\Lambda$ | $1024 \times 1024$ | -2.00 |
| B2 | | | -1.75 |
| B3 | | | -1.5 |
| C1 | $31\Lambda$ | $1024 \times 1024$ | -2.00 |
| C2 | | | -1.75 |
| C3 | | | -1.5 |

**Table 11.1:** Values of coefficient $\alpha$, confinement radius $R$ and numerical resolution $N^2$, for the three sets of simulations (A, B, C). All the simulations are performed with parameters $\lambda_0 = 3.5$, $\beta = 0.01$, $\Gamma_0 = 2$, $\Gamma_2 = 1$, $\tau = 0.001$, and grid spacing $\Delta x = 5/64\Lambda$.

For the analysis, we decompose the velocity field in the radial and angular components $\boldsymbol{u} = u_r \hat{\boldsymbol{r}} + u_\varphi \hat{\boldsymbol{\varphi}}$ which define the radial and angular kinetic energies $E_r = \frac{1}{2}\langle u_r^2 \rangle$ and $E_\varphi = \frac{1}{2}\langle u_\varphi^2 \rangle$ (here and in the following, $\langle \cdot \rangle$ denotes spatial average over the circular domain of radius $R$).

## 11.3 Emergence of the giant vortex

As an initial condition, we considered a null velocity field seeded with an infinitesimal random perturbation. At the beginning of the simulation, phenomenologically lead by the Swift-Hohenberg term, the swimmers organize in a large number of small-scale vortices, with equal probability of positive and negative vorticity and homogeneous and isotropic spatial distribution. This state corresponds to the mesoscale turbulence, therefore the statistical properties of the flow are identical to those observed in simulations with periodic boundary conditions [172, 173, 190]. Since we are considering values of $\alpha$ beyond the threshold $\alpha_c$ we defined in the previous chapter, the mesoscale turbulence is not stable: after a short time, the system evolves towards the regime of flocking turbulence, characterized by the presence of multiple large-scale vortices, which move chaotically and are surrounded by regions of vorticity streaks (see Fig. 11.1, left panel).

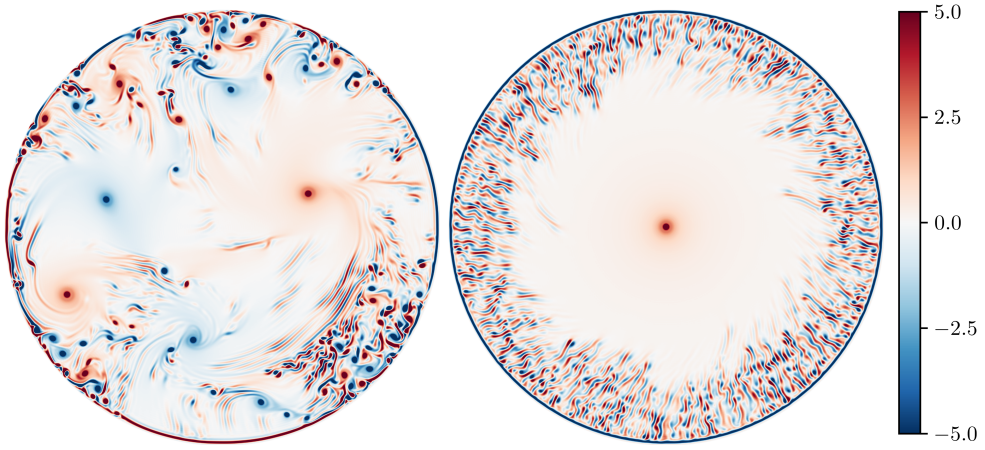


**Figure 11.1:** Vorticity field for the simulation with $R = 31\Lambda$ and $\alpha = -1.75$ at $t = 210\Lambda/U$ (left) and $t = 550\Lambda/U$ (right).

During this chaotic regime we observe an approximate equipartition (with strong temporal fluctuations) between the radial and angular components of the kinetic energy (see Fig. 11.2 left panel). At later times, the system displays a rapid increase of $E_\varphi$ accompanied by the decrease of $E_r$, which indicates the transition to a novel regime characterized by

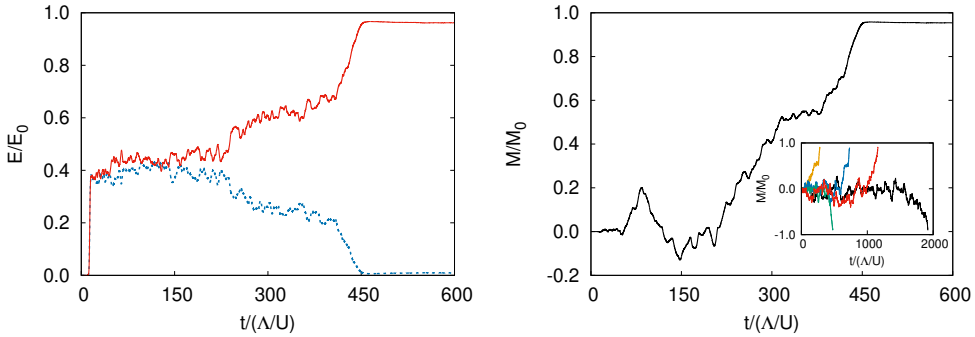


**Figure 11.2:** (*left*) Temporal evolution of the radial and angular components of the kinetic energy $E_r$ (blue, dashed line), $E_\varphi$ (red, solid line) normalized with $E_0 = \frac{1}{2}U^2$. Simulation at $R = 31\Lambda$ and $\alpha = -1.75$. (*right*) Temporal evolution of the angular momentum $M$ normalized with $M_0 = \frac{2}{3}UR$ for the simulation at $R = 31\Lambda$ and $\alpha = -1.75$. The inset shows the evolution of the angular momentum for an ensemble of simulation with different initial conditions with $\alpha = -1.50$ and $R = 16\Lambda$.

$E_\varphi \simeq E_0 \equiv \frac{1}{2}U^2$ and $E_r \simeq 0$. This means that the swimmers self-organize in a state of *circular flocking*, that is, a stationary, single, giant vortex which spans the whole domain (see Fig. 11.1 right panel), similar to that observed in experiments of bacterial suspension in a viscoelastic fluid [212].

The formation of this large-scale structure corresponds to a symmetry breaking of the angular momentum of the flow $M = \langle \boldsymbol{r} \times \boldsymbol{u} \rangle$. As shown in the right panel of Figure 11.2, the values of $M$ display strong fluctuations around zero before the formation of the giant vortex. With the ultimate transition to circular flocking, $M$ saturates to a constant value $|M| \simeq M_0 \equiv \frac{2}{3}UR$ with definite sign. The transition times, from the chaotic regime of flocking turbulence to the stationary giant-vortex state, appears to be unpredictable, since we observed a strong variability, changing the initial random perturbation (see the inset in the right panel of Figure 11.2). The variability of transition time will be discussed further in this chapter.

In Figure 11.3 we compare the energy spectra $E(k)$before and after the transition (the spectra correspond to the fields shown in Figure 11.1). Before the transition, we find that the intermediate regime is characterized by the turbulent-like power-law energy spectrum $E(k) \sim k^{-\zeta}$, that we dis-

cussed in the previous chapter, where the spectral slope $\zeta \simeq -2$ observed in our simulations is steeper than the value $-3/2$ reported in [200] because of confinement. After the formation of the giant vortex, we observe a spectral condensation of the energy in the lowest mode, accompanied by a depletion of the energy spectrum at intermediate wavenumbers. At wavenumbers $k \gtrsim 2\pi/\Lambda$ the spectrum remains almost unchanged.

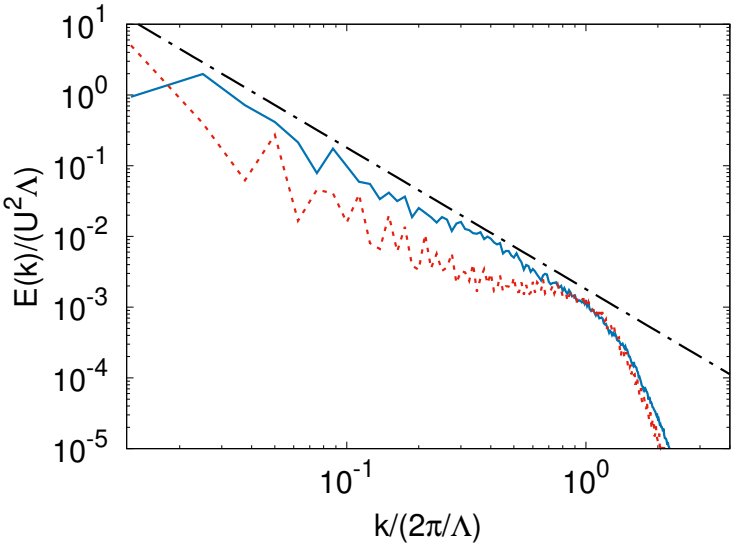


**Figure 11.3:** Energy spectra for the simulation with $R = 31\Lambda$ and $\alpha = -1.75$ at $t = 210\Lambda/U$ (blue, solid line) and $t = 550\Lambda/U$ (red, dashed line). The black, dash-dotted line represents the slope $k^{-2}$.

We can quantify the degree of order of the collective motion of the swimmers in the giant vortex adopting the vortex order parameter [164, 210, 211] (VOP) which is defined as $\Phi = (\langle|\boldsymbol{u}\cdot\hat{\boldsymbol{\varphi}}|\rangle/\langle|\boldsymbol{u}|\rangle - 2/\pi)/(1-2/\pi)$. A velocity field oriented in the angular direction $\boldsymbol{u} \parallel \hat{\boldsymbol{\varphi}}$ gives $\Phi = 1$, while $\Phi = 0$ corresponds to random-oriented velocity. The values of $\Phi$ measured in the late stage are very close to 1, (see Figure 11.4), which indicates that the motion of the swimmers is highly ordered. The degree of order increases reducing the radius $R$ of the domain and increasing $|\alpha|$.

The temporal evolution of $\Phi$ provide us a good criterium fo the evaluation of the transition time. For this purpose, we performed an additional ensemble of 269 simulations of the case A3, at fixed $\alpha = -1.50$, $\lambda_0 = 3.5$ and $R = 16\Lambda$ (we chose the smallest domain in order to reduce the com-

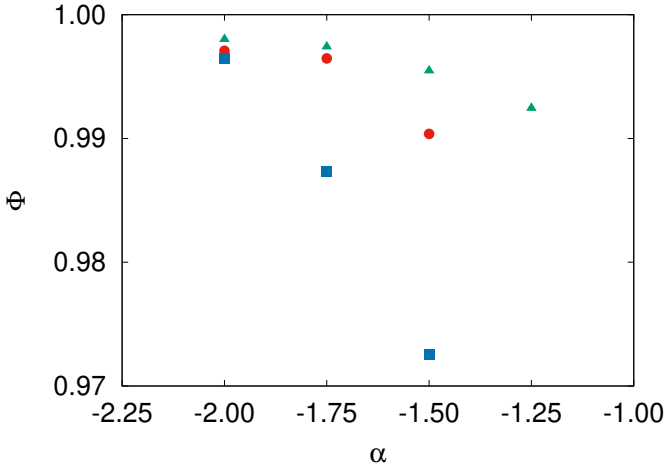


**Figure 11.4:** Mean value of the vortex order parameter $\Phi$ as a function of $\alpha$ for $R = 16\Lambda$ (green triangles), $R = 23\Lambda$ (red circles), $R = 31\Lambda$ (blue squares).

putation time), with different initial random perturbations. We assume as evidence of the transition the fact that the VOP exceeds the threshold value of $\Phi_{thr} = 0.95$.

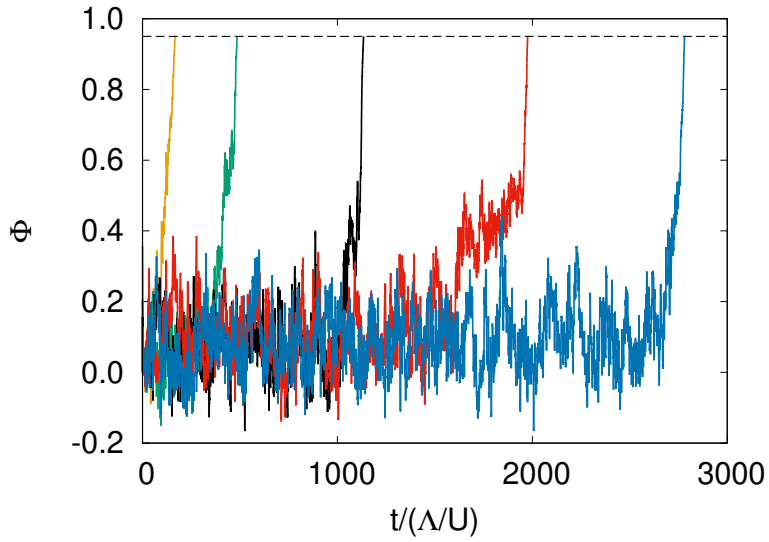


**Figure 11.5:** Temporal evolution of the vortex order parameter $\Phi$, for an ensemble of simulations with $\lambda_0 = 3.5$, $\alpha = -1.50$ and $R = 16\Lambda$, with different initial conditions.

From Figure 11.5 we can notice the metastable nature of the flocking turbulence regime: this ultimate transition to the circular flocking can

require an unpredictable transient time in order to happen: it is frequent that, before the giant vortex state is achieved, the system goes through several failed attempts, with one of the larger vortices which, after reaching a size greater than that of the other one, suddenly inverts its growth process.

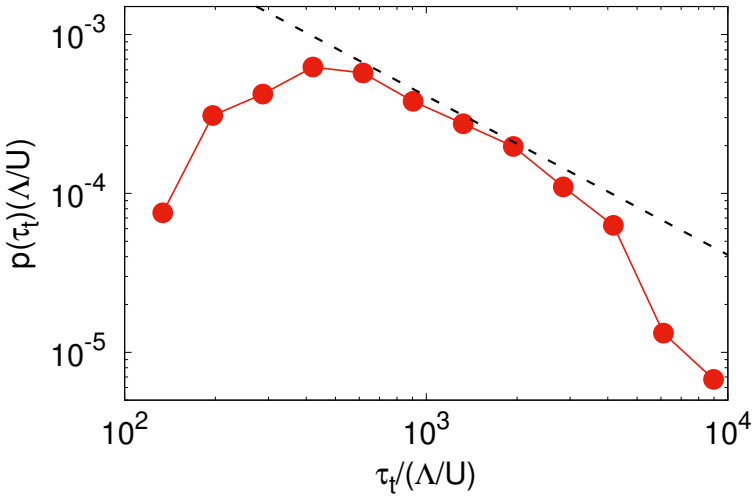


**Figure 11.6:** Probability density function $p(\tau_t)$ of the transition time $\tau_t$ to the circular flocking state, with $R = 16\Lambda$, $\alpha = -1.50$ and $\lambda_0 = 3.5$. The black dashed line represents the slope $\tau_t^{-1}$.

We observed almost two orders of magnitude in the variability of the transition time $\tau_t$. The probability density function we computed (fig. 11.6) shows a maximum around $\tau_t \sim 400\Lambda/U$, and it seems to be compatible with a $\tau_t^{-1}$ decay in the range $\sim 500 - 4000\tau_t/(\Lambda/U)$, before an apparent cut-off at larger times.

Unfortunately we do not have a theory which could predict such a law, or a different one, since this ultimate transition appears to be strongly out-of-equilibrium. However, it is reasonable to expect that the statistic of the transition time depends on the parameters $\alpha$, $\lambda_0$ and $R$, but an investigation in that sense would require larger ensembles of simulations, with an extensive exploration of the parameter space.

## 11.4 Radial profiles of the giant vortex

If we consider the time-averaged, mean radial vorticity profile of the giant vortex $\overline{\omega}(r) = \frac{1}{2\pi r}\int \omega(\boldsymbol{r}')\delta(|\boldsymbol{r}'| - r)d^2r'$ we can observe a power law behaviour $\overline{\omega}(r) \propto 1/r$ in the region $\Lambda \lesssim r \lesssim R - \Lambda$ far from the boundaries and from the center (Figure 11.7). We can derive a theoretical prediction for $\overline{\omega}(r)$ by assuming that the radial component of the velocity vanishes, $u_r = 0$, and that the angular component depends only on $r$ as $u_\varphi = r\Omega(r)$, where $\Omega(r)$ is the angular velocity. The resulting vorticity field is $\omega = \boldsymbol{\nabla} \times \boldsymbol{u} = 2\Omega(r) + r\partial_r\Omega(r)$. Inserting these expressions in the equation for the vorticity, which is obtained by taking the curl of Eq. (11.1), and imposing the stationarity condition, one gets the following equation for $\Omega(r)$

$$(\alpha + \Gamma_0\nabla^2 + \Gamma_2\nabla^4)(2\Omega + r\partial_r\Omega) + \beta r^2\Omega^2(4\Omega + 3r\partial_r\Omega) = 0. \qquad (11.2)$$

We also assume that the Swift-Hohenberg term is negligible for $r \gg \Lambda$, this assumption is justified *a posteriori*, since the Swift-Hohenberg operator applied to a vorticity field $\overline{\omega}(r) = \pm U/r$ gives subleading terms of order $O((r/\Lambda)^{-3})$ which are negligible for $r \gg \Lambda$. In this case, the equation (11.2), admits the power-law solution $\Omega(r) = cr^\gamma$ with $c = \pm\sqrt{-\alpha/\beta}$ and $\gamma = -1$. This gives a prediction for the radial profiles of velocity $\overline{\boldsymbol{u}}(r) = \pm U\hat{\boldsymbol{\varphi}}$ and vorticity $\overline{\omega}(r) = \pm U/r$, which is in perfect agreement with our numerical findings (see Figure 11.7).

Beside the giant vortex, Figure 11.1 also shows the presence of vorticity fluctuations in an annular region close to the boundary. These elongated structures, slightly leaned in the direction of the mean flow of the vortex, correspond to the same vorticity streaks we noticed in the flocking turbulence regime. Since they have a typical transverse width of the order of $\Lambda$, the average number of streaks in a domain of radius $R$ is therefore $N \simeq 2R\sqrt{\Gamma_0/2\Gamma_2}$.

The intensity of the vorticity fluctuations can be quantified by the RMS vorticity profile $\overline{\omega}_{rms}(r) = (\overline{\omega^2}(r))^{1/2}$ which is shown in Figure 11.7. Vorticity fluctuations are absent in the central region of the vortex, in which $\overline{\omega}_{rms}(r)$ coincides with the mean radial profile $|\overline{\omega}(r)|$. They appear

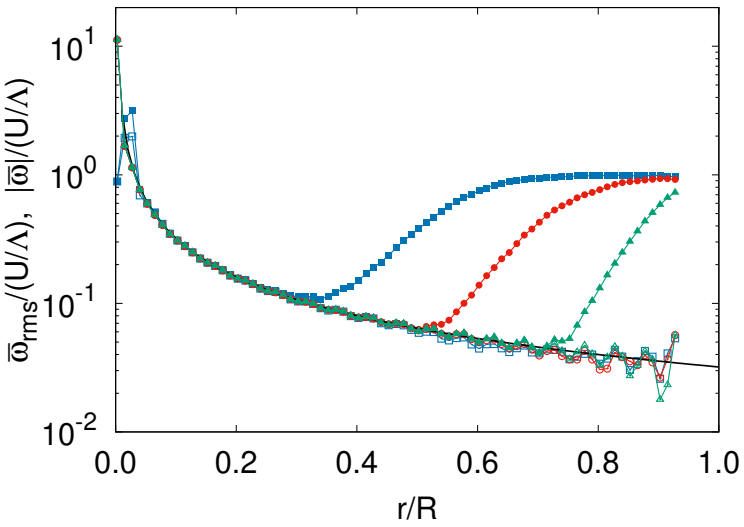


**Figure 11.7:** Radial profiles of the vorticity, $\overline{\omega}(r)$ (empty symbols), and of the RMS vorticity, $\overline{\omega}_{rms}(r)$ (filled symbols), for simulations with $R = 31\Lambda$, $\alpha = -1.5$ (blue squares), $\alpha = -1.75$ (red circles) and $\alpha = -2$ (green triangles). The black line is the prediction $|\overline{\omega}(r)| = U/r$.

at larger $r$, as shown by the increase of $\overline{\omega}_{rms}(r)$ which reaches an almost constant plateau close to the boundary $\overline{\omega}_{rms}(r) \simeq U/\Lambda$.

Further details on the statistics of the streaks are revealed by the profiles of radial and angular velocity fluctuations defined as $\overline{u'_r}(r) = (\overline{u_r^2}(r))^{1/2}$ and $\overline{u'_\varphi}(r) = (\overline{u_\varphi^2}(r) - \overline{u_\varphi}^2(r))^{1/2}$, shown in Figure 11.8. The radial component is predominant in the velocity field of the streaks. Close to the boundary, the ratio between the intensities of radial and angular fluctuations is almost constant $\overline{u'_r}/\overline{u'_\varphi} \simeq 4.2$. The intensity of velocity fluctuations decays at increasing the distance from the boundary $R - r$.

The width of the region in which the streaks are present can be quantified as the distance $\delta$ from the boundary at which the radial profile of the order parameter exceeds a given threshold value $\overline{\Phi}(R-\delta) = \Phi_{thr}$ (see Fig. 11.9). The values of $\delta$ (with $\Phi_{thr} = 0.9995$) are reported in the inset of Figure 11.9. We find that $\delta$ increases monotonically increasing the radius $R$ of the circular domain and decreasing the parameter $|\alpha|$. The scaling of $\delta$ as a function of the parameters of the model and of the radius $R$ remains an open question which deserves further theoretical studies.

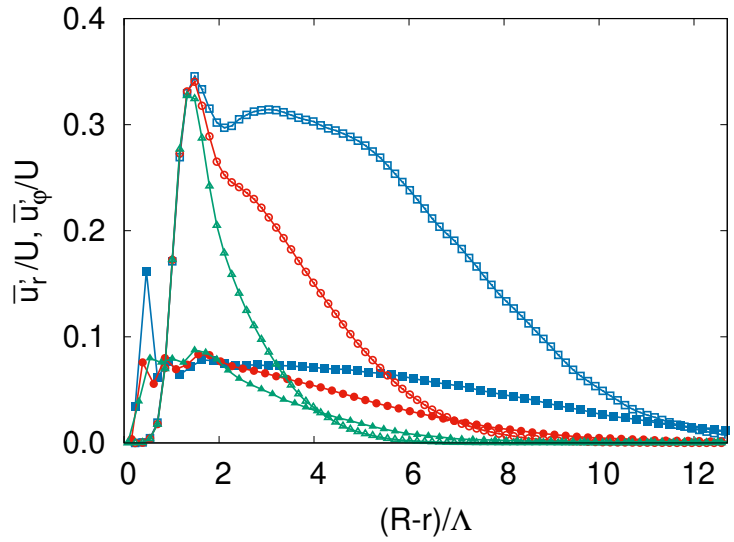


**Figure 11.8:** Radial profiles of the radial and tangential components of the velocity fluctuations, $\overline{u_r'}(r)$ (empty symbols) and $\overline{u_\varphi'}((r)$ (filled symbols), as a function of the distance from the boundary for $\alpha = -1.75$, $R = 31\Lambda$ (blue squares), $\alpha = -1.5$, $R = 23\Lambda$ (red circles) and $\alpha = -1.25$, $R = 16\Lambda$ (green triangles).

## 11.5 Discussions

The formation of the giant vortex surrounded by streaks is strictly related to the phenomenon of flocking turbulence described in [174,195,200] and in the previous chapter. In this regime we have the competition between the Toner-Tu term, composed by Landau potential and the self-propulsion term, and the Swift-Hohenberg operator. While the former promote the development of a flocking state, in which all the bacteria swim in the same direction with a constant speed, [133] the latter destabilize this collective ordered motion, with the formation of vorticity streaks in the transverse direction with respect to the mean flow [177] (see also the linear stability analysis of the global polar state in section 9.1). A possible explanation of our findings is that the confinement in circular domains permits to one of the larger vortices which characterize the flocking turbulence, *i.e.* one of the manifestation of the spontaneous symmetry breaking of the system, to prevail on the others, extending its symmetry breaking from a limited region to all the domain. The vorticity produc-

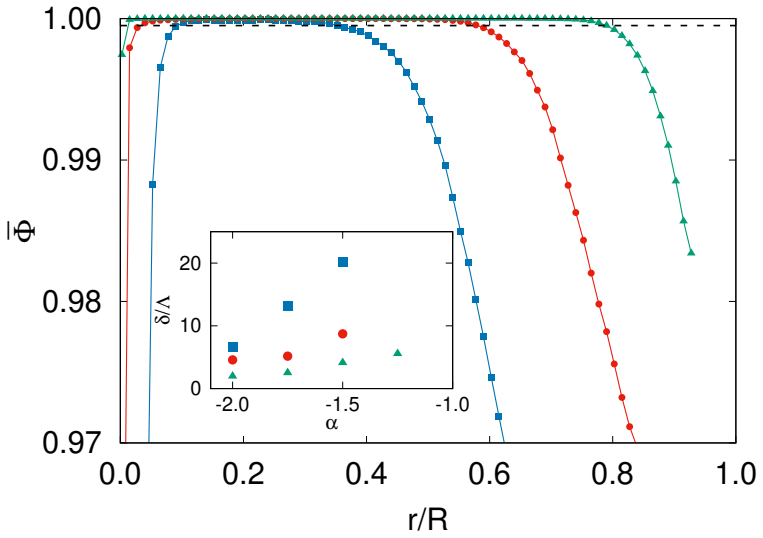


**Figure 11.9:** Radial profiles of the vortex order parameter, $\overline{\Phi}(r)$, for simulations with $R = 31\Lambda$, $\alpha = -1.5$ (blue squares), $\alpha = -1.75$ (red circles) and $\alpha = -2$ (green triangles). The black dashed line is the threshold value $\Phi_{thr} = 0.9995$ used to define the width $\delta$ of the region in which the streaks are present. Inset: Width $\delta$ of the annular regions of the streaks as a function of $\alpha$ for $R = 16\Lambda$ (green triangles), $R = 23\Lambda$ (red circles), $R = 31\Lambda$ (blue squares).

tion due to friction forces near the boundary probably triggers the global symmetry breaking of the angular momentum facilitating the formation of the giant vortex.

Despite this simple interpretation, the formation of the giant vortex, is a highly non-trivial process which is far from being fully understood. As shown in Figure 11.5, the final state with a single vortex is achieved after a long, metastable regime of flocking turbulence in which several large-scale vortices compete with each other to prevail, with a strong variability of the duration of this intermediate regime. This confirms the complexity of this process and suggests that the transition to the giant vortex may have a stochastic nature, with a broad distribution of the transition times, as shown in Figure 11.6.

We remark that the phenomenon presented here differs deeply from those previously reported in experiments [164,210] and numerical simulations [131] of confined bacterial suspensions. The confining scale in these

studies is much smaller than in our case, and the rectified vortex originates directly from the linear instabilities of the steady, no-flow state. Moreover, they found a double vortex with a non-monotonic radial profile of the azimuthal velocity [131], Conversely, the giant vortex observed in our study displays a uniform profile of azimuthal velocity surrounded by an annular region of vorticity streaks, and it is produced by a non-linear mechanism, related to the interaction of the flocking turbulence regime, itself generated by a non-trivial competition between a large scale tendency to flock and a small scale destabilization, with the boundaries. This process requires a domain large enough to allow for the development of the chaotic regime which precedes the transition to the giant vortex. Our simulations show that a domain with radius $R = 16\Lambda$ is sufficient for this purpose.

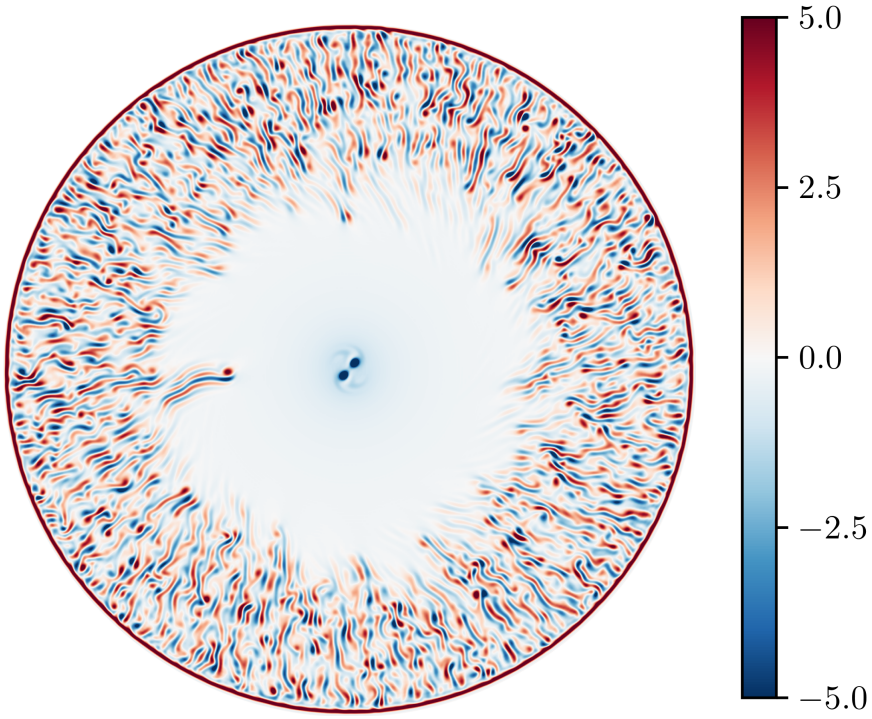


**Figure 11.10:** Vorticity field in late stage of the simulation with $R = 31\Lambda$ and $\alpha = -1.50$, which displays a giant vortex whose core consists of a binary rotating system of two small, equal-sign vortices.

The exact determination of the range of values of $R/\Lambda$ in which the

giant vortex forms remains an open question. At fixed $\alpha$ and $\lambda_0$ we find that there is a maximum size of the domain which allows for the formation of the giant vortex. Nonetheless, it is extremely difficult to determine the precise value of this maximum size, because of the strong variability of the transition times. For values of $R$ close to the maximum size, we observed in same cases the formation a giant vortex whose core consists of a binary rotating system of two small, equal-sign vortices (see Figure 11.10). Increasing further the radius $R$ the system apparently remains in the flocking turbulent state, which none of the large-scale vortices managing to incorporate the other ones and therefore to extend its spontaneous symmetry breaking to all the domain.

# Conclusions

The numerical investigations reported in this thesis constitute an advancement in the study of two different examples of chaotic flows, which are characterized by a "turbulent- like" behavior at low Reynolds numbers.

Regarding the dilute rigid polymer solutions, we confirmed the emergence of a chaotic flow at low Reynolds number, with increased flow resistance and enhanced mixing efficiency, similar to the elastic turbulence observed with flexible polymers. The phenomenology observed is qualitatively independent on the dimensionality, but we found that, for the same values of the parameters, the effects are stronger in the 2D case. This difference is explained in terms of the different rotational degrees of freedom of the rods. Further numerical studies at higher resolution and/or with a different numerical scheme would allow to reach more realistic values of the parameters. Especially an experimental verification is required: a viable experimental realization could be performed with a dilute solution of polymers of length $\ell \approx 2-5\mu m$ (e.g., xantam gum) with concentrations of about 100 wppm in a microchannel of width $L \approx 2mm$, with a setup similar to the one considered in elastic turbulence experiments [26,55,57]. Typical velocities in these experiments are of the order of $U \approx 6mm/s$, which ensures the stability of the laminar flow in absence of polymers.

Apart from this investigation, we also tried to perform an analytic study of the linear stability of the Kolmogorov flow with rod-like polymers, but our result is not compatible with data from numerical simulations, implying that some of the approximations we made, especially

the use of multiple scales method, are not valid. On the contrary, the numerical investigation at high-Reynolds number appears to be compatible with experimental studies. In fact, our observation of drag reduction absence in an unbounded shear flow agrees with the hypothesis that drag reduction in rigid polymer solution is due to the establishment of an effective "lubricating layer" near the walls. [30] Moreover, also the small-scale behaviour we observe appears to be compatible with recent experimental studies. [117] Further investigations, with additional values of Reynolds number and/or polymer concentration, or even in the homogeneous isotropic case, would help to clarify the effect of rodlike polymers on turbulent flows.

In the study of dense bacterial suspensions we considered the case of strong aligning interactions between the swimmers, in confined circular domains. In the first part of our work, we explored the parameter space of the model, and we found that the model displays two different regimes, which are observed respectively at moderate and large intensity of alignment. In the former case, the velocity field consists of an homogeneous dense population of small vortices which move chaotically. This regime is known in the literature as mesoscale turbulence. Increasing the intensity of the aligning force we observe the emergence of the flocking turbulence regime, characterized by an inhomogeneous flow with large-scale vortices surrounded by regions of uniform circular motion, alternated with regions of elongated vortical structures called streaks. The regime of mesoscale turbulence occurs if the alignment interactions are weaker than the destabilization effects. In this case the swimmers cannot develop large flocks. Conversely, when the combined action of alignment interactions and self-advection is dominant, we observe the spontaneous formation of local circular flocks. Since the velocity field represents also the order parameter of the system, we can interpret the formation of these coherent structures with constant speed as a spontaneous breaking of the local rotational symmetry, occurring independently in different regions of the domain. We highlighted the out-of-equilibrium nature of

this transition, and provided a criterium in order to estimate the threshold parameters between the two regimes. Finally, we investigated also the effects of the confinement in the circular domain. Our results show that these effects become relevant when the radius of the domain is of the order of the correlation scale of the flow, which is the case of flocking turbulence, while in the regime of mesoscale turbulence the flow is weakly affected by the confinement. Further investigations about the transition could be carried out using the same techniques from statistical physics adopted for other versions of the Toner-Tu model. [146, 150, 156, 159]

In the second part of our investigation we described the fact that confinement can induce an ulterior transition, from the regime of flocking turbulence to an ordered state of circular flocking, which corresponds to a single giant vortex which extends over the entire domain. In this case, the local spontaneous symmetry breaking of the velocity field becomes a global symmetry breaking of the total angular momentum of the system. We characterized the properties of this regime, in particular of the mean circular flow (which can be analytically predicted) and the radial fluctuations, and we also investigated the statistics of the transition, finding that we have a huge variability for the time required to the emergence of this state. This variability, and the fact that the system usually requires several attempts in order to evolve in this ultimate state, shows the complexity of this transition, and the metastable nature of the flocking turbulence state. Further investigations are required, in order to relate the parameters of the model with the statistics of the transition, the properties of the radial fluctuations and the confinement scale required to induce the emergence of the giant vortex.

Moreover, other informations, both for the flocking turbulence and the giant vortex regimes, could be obtained by experimental studies. A quantitative correspondence between our simulations and a feasible experimental setup can be established by matching the parameters of the TTSH model with the typical values of the characteristic scale $\Lambda$ and velocity $U$ of the collective bacterial motion which are observed in experiments (e.g., in [123, 183, 213]). As an example, by fixing $\Lambda \simeq 25\mu m$ and $U \simeq 50\mu m/s$

the values of the radius $R$ of the circular domain considered in our studies correspond in physical units to the range $R \simeq (400 - 1600)\mu m$, the values of the parameter $\alpha$ are in the range $-\alpha \simeq (0.5 - 1.8)s^{-1}$ and the typical time required to observe the formation of the giant vortex is of the order of minutes. These spatial and temporal scales are easily accessible in experiments of dense bacterial suspensions, such as those of *Bacillus subtilis*.

# Appendix A

# Numerical methods.

The problem of the integration of Navier-Stokes equation (NSE), and other hydrodynamical related equations, has generated over the years a large number of different approaches and methods. A first difference between the possible approaches with the problem is if we want to integrate NSE with the greatest possible precision, or if we accept some approximate model to describe part of the flow (usually, the smaller scales). The first approach is clearly preferable in a scientific work, but can be extremely expensive in terms of computation resources, thus not feasible for many practical applications (especially for complicated domains). The first approach, that we choose, is one of the Direct Numerical Simulations (DNS), where everything that is not explicitly simulated does not exist, while for the second one, depending on the level of approximation, we have for example Large-Eddies-Simulations (LES) and Reynolds-Averaged-Navier-Stokes (RANS). To perform DNS, a large number of methods exist. The choice can depend on the physics of the problem (for example, compressible vs incompressible flows), on the boundary conditions, and on other elements. We adopted a pseudo-spectral method for the spatial integration, and an implicit Runge-Kutta scheme for the time evolution. For the implementation of the boundary conditions in the confined TTSH model, we used a penalization method.

## A.1 The pseudo-spectral algorithm

The idea behind the spectral methods [111] is that, if we have an unknown function $u(x)$ (neglecting for the moment the temporal dependence), obeying to generic integral-differential equation:

$$Au = f(x), \tag{A.1}$$

it can be easy to obtain a good approximation (and, in some particular cases, an exact solution) of $u(x)$ if we express the unknown in terms of a sum of $N+1$ basis function $\phi_n(x)$

$$u\left(x\right) \approx u_N\left(x\right) = \sum_{n=0}^{N} a_n \phi_n\left(x\right). \tag{A.2}$$

The coefficients $a_n$ have to be chosen in order to minimize the residual function (which is zero in the case of exact solution):

$$R(x, a_0, \ldots, a_N) = Au - f(x). \tag{A.3}$$

According [111], pseudospectral methods are the one where the coefficients $a_n$ are found imposing that the residual function is equal to zero for $N$ selected value of $x$, called "collocation" or "interpolation" points. These points are clearly the grid points of our domain, and we expect that $u_N(x)$ converges to $u(x)$ for increasing $N$.

The choice of the basis functions $\phi_n(x)$ is strictly related to the domain and to the boundary conditions. If we have a periodic domain, the natural choice is to adopt an ordinary Fourier series, while if the domain is bounded the Chebyshev polynomials are a better option, and, on a spherical surface, spherical harmonics are the natural answer. In a multi-dimensional domain, it is also possible to expand in a direction with a certain basis and in another direction with a different one: this is commonly adopted in channel flow simulations, where there is periodicity along two directions, so Fourier basis, and walls in the third one, so Chebyshev (see for example [41]). For our code we adopted a Fourier basis.

The principal reason which make spectral method particularly suitable is the fact that the Fourier transform converts differential operator into

algebraic multiplication:

$$\partial_x f(x) \qquad \rightarrow \qquad ik\hat{f}(k), \tag{A.4}$$

which is particularly convenient especially if we need to invert a differential operator (for example, if we want to obtain the velocity field from the vorticity), a task particularly expensive to be done in physical space:

$$f(x) = \nabla^2 g(x) \qquad \Longrightarrow \qquad \hat{g}\,(k) = \frac{\hat{f}\,(k)}{k^2}. \tag{A.5}$$

On the other side, nonlinear operations, such as the advection or the non-Newtonian stress in the Doi-Edwards model, become much more complicated in Fourier space, since products in physical space are associated to convolutions in spectral space. The strategy behind our code is to switch between physical and spectral space, performing differential/integral operations in Fourier space and products in real space. This is a convenient way of working if the computation cost required to perform the Fourier transforms is reduced with respect the computation cost of performing the convolutions in the spectral space (or the integral in the real space). Luckily, the huge number of applications for the Fourier analysis stimulated the ideation of a large number of "Fast Fourier Transform" (FFT) algorithms, [112] allowing us to actually apply this strategy. Anyway, the evaluation of Fourier series remains the most computationally expensive part of our code: this means that optimizing the algorithm consists principally in minimize the number of Fourier transforms.

As an example, this is how we compute the advection term in two dimensions (taking advantage that, for an incompressible flow, we have $(\boldsymbol{u} \cdot \nabla)\omega = \nabla \cdot (\omega \boldsymbol{u})$):

- we start with the vorticity $\hat{\omega}$ in Fourier space;
- we compute the two components of the velocity:

$$\hat{u}_x = \frac{ik_y}{k^2}\hat{\omega}, \qquad \hat{u}_y = \frac{-ik_x}{k^2}\hat{\omega}; \tag{A.6}$$

- we anti-transform $\hat{\omega}$, $\hat{u}_x$ and $\hat{u}_y$ into the real space;
- we compute the two products $\omega u_x$ and $\omega u_y$;

- we transform the two products in the Fourier space

- we finally obtain the advection term in Fourier space applying the divergence operator:

$$\widehat{\nabla \cdot (\omega \boldsymbol{u})} = ik_x \widehat{\omega u_x} + ik_y \widehat{\omega u_y}. \tag{A.7}$$

This procedure has to be done for each one of the $N+1$ Fourier modes: this means that we have converted one PDE into $N+1$ ODEs, with every Fourier mode that is then made to evolve independently in time.

Finally, we have to mention two important issues of the pseudospectral methods. The first one is that, in order to be accurate, they require the field $u(x)$ to be smooth. In our case, this can be addressed simply increasing the spatial resolution, but it makes these methods unsuitable when strong gradients are expected (for example, in compressible flows with shock waves).

The second one, strictly related, is the aliasing problem. If we sample uniformly the function $u(x)$ with $N$ points, in the Fourier space we have wavenumbers $k_n$ with $n \in [-N/2, N/2]$. The nonlinear terms generate modes that should not be contained in the wavenumber grid ($|n| > N/2$), but the FFT spuriously moved them into the range $[-N/2, N/2]$. In the context of computational fluid dynamics, it was observed for the first time by Philips in 1956: his General Circulation Model developed an instability after a certain period of time, independently from the integration step. [214] In 1959 he proposed a solution: since the break-up of the simulation was generated by a quadratic nonlinearity, filtering out all the modes with $|n| > N/4$ would eliminated the instability, at the cost of halving the effective resolution. [215] In 1971 Orszag pointed out that filtering the modes with $|n| > N/3$ was sufficient in order to prevent instability. [216] Since in our code, both in Doi-Edwards and TTSH model, we are dealing with cubic nonlinearities, we have to filter at $|n| > N/4$.

## A.2 Implicit Runge-Kutta

As we already mentioned, the pseudospectral method converts one PDE in the physical space into $N+1$ ODEs in the Fourier space (assuming for simplicity only one spatial dimension). One of the most famous family of numerical scheme for the resolution of initial value first-order ODEs is the one of Runge-Kutta methods. [217, 218] Considering a generic ODE

$$\dot{x} = f(t, x) \tag{A.8}$$

we start from the Euler method, that is simply the discretization of the definition of derivative (where $\Delta t$ is the time step):

$$x_{i+1} = x_i + \Delta t f(t_i, x_i). \tag{A.9}$$

Since this method is not very accurate and quite unstable, the idea of the Runge-Kutta schemes is to take one (or more) trial step to the midpoint of the interval, to eliminate the first-order error term. [112] The most simple Runge-Kutta scheme, the second-order one, is therefore:

$$\begin{aligned} k_1 &= f\left(t_i, x_i\right); \\ k_2 &= f\left(t_i + \frac{\Delta t}{2}, x_i + \frac{\Delta t}{2} k_1\right); \\ x_{i+1} &= x_i + \Delta t k_2. \end{aligned} \tag{A.10}$$

Increasing the number of intermediate steps we further reduce the error: this is a good strategy if it allows us to increase the time step enough to counterbalance the increase of evaluations of the right-hand-side of equation (A.8). In our case, we found that the best choice was the fourth-order version (RK4):

$$
\begin{aligned}
k_1 &= f\left(t_i, x_i\right); \\
k_2 &= f\left(t_i + \frac{\Delta t}{2}, x_i + \frac{\Delta t}{2} k_1\right); \\
k_3 &= f\left(t_i + \frac{\Delta t}{2}, x_i + \frac{\Delta t}{2} k_2\right); \\
k_4 &= f\left(t_i + \Delta t, x_i + \Delta t k_3\right); \\
x_{i+1} &= x_i + \frac{\Delta t}{6}\left(k_1 + 2k_2 + 2k_3 + k_4\right).
\end{aligned} \tag{A.11}
$$

We further modify the algorithm since the RK schemes are required only to solve nonlinear equations, since the solution of a linear ODE $\dot{x} = \mathcal{L}x\left(t\right)$ can be analytically expressed as $x\left(t\right) = x(0)e^{\mathcal{L}t}$. In our case, since our equations include one (or more) linear term, we can integrate exactly this terms, and use RK4 only for the non-linear parts, in order to be more accurate. This is called implicit Runge-Kutta.

In general, hydrodynamics equations can be expressed as:

$$
\partial_t x = F\left(x\right) + \mathcal{L}x, \tag{A.12}
$$

where $F$ is the nonlinear operator (including advection, polymer stress, cubic damping etc.) while $\mathcal{L}$ is the linear one, corresponding to $\nu k^2$ in the Navier-Stokes equation and to $-\alpha - \Gamma_0 k^2 - \Gamma_2 k^4$ in the TTSH model. In order to integrate exactly the linear part, we set:

$$
x = ye^{\mathcal{L}t}, \qquad \Rightarrow \qquad \dot{y} = e^{-\mathcal{L}t} F(e^{\mathcal{L}t} y) \equiv g(t, y). \tag{A.13}
$$

Applying the RK4 scheme to the equation $\dot{y} = g(t, y)$, and re-expressing the $k$ coefficients in terms of $x$ we have:

$$
k_1 = e^{-\mathcal{L}t_i} F(e^{\mathcal{L}t_i} y_i) = e^{-\mathcal{L}t_i} F(x_i),
$$

$$
\begin{aligned}
k_2 &= e^{-\mathcal{L}(t_i + \Delta t/2)} F\left(e^{\mathcal{L}(t_i + \Delta t/2)} y_i + e^{\mathcal{L}(t_i + \Delta t/2)} \frac{k_1}{2} \Delta t\right) = \\
&= e^{-\mathcal{L}(t_i + \Delta t/2)} F\left(e^{\mathcal{L}\Delta t/2} x_i + e^{\mathcal{L}\Delta t/2} \frac{\Delta t}{2} F(x_i)\right),
\end{aligned}
$$

$$k_3 = e^{-\mathcal{L}(t_i+\Delta t/2)} F\left(e^{\mathcal{L}(t_i+\Delta t/2)} y_i + e^{\mathcal{L}(t_i+\Delta t/2)} \frac{k_2}{2}\Delta t\right) =$$
$$= e^{-\mathcal{L}(t_i+\Delta t/2)} F\left(e^{\mathcal{L}\Delta t/2} x_i + \frac{\Delta t}{2} F\left(e^{\mathcal{L}\Delta t/2} x_i + e^{\mathcal{L}\Delta t/2}\frac{\Delta t}{2} F(x_i)\right)\right),$$

$$k_4 = e^{-\mathcal{L}(t_i+\Delta t)} F\left(e^{\mathcal{L}(t_i+\Delta t)} y_i + e^{\mathcal{L}(t_i+\Delta t)} k_3 \Delta t\right) =$$
$$= e^{-\mathcal{L}(t_i+\Delta t)} F\Bigg(e^{\mathcal{L}\Delta t} x_i + e^{\mathcal{L}\Delta t/2}\Delta t F\Bigg(e^{\mathcal{L}\Delta t/2} x_i$$
$$+ \frac{\Delta t}{2} F\left(e^{\mathcal{L}\Delta t/2} x_i + e^{\mathcal{L}\Delta t/2}\frac{\Delta t}{2} F(x_i)\right)\Bigg)\Bigg).$$

In order to obtain a manageable expression, we re-define the arguments of nonlinear operator:

$$b_1^* = x_i, \qquad b_2^* = e^{\mathcal{L}\Delta t/2}\left(x_i + \frac{\Delta t}{2} F\left(b_1^*\right)\right), \qquad b_3^* = e^{\mathcal{L}\Delta t/2} x_i + \frac{\Delta t}{2} F\left(b_2^*\right),$$
$$b_4^* = e^{\mathcal{L}\Delta t/2}\left(e^{\mathcal{L}\Delta t/2} x_i + \Delta t F\left(b_3^*\right)\right).$$

Therefore, $y_{i+1}$ is:

$$y_{i+1} = y_i + \frac{\Delta t}{6} e^{-\mathcal{L}t_i}\left(F(b_1^*) + 2e^{-\mathcal{L}\Delta t/2} F(b_2^*) + 2e^{-\mathcal{L}\Delta t/2} F(b_3^*) + e^{-\mathcal{L}\Delta t} F(b_4^*)\right), \tag{A.14}$$

and, since we know that $x_{i+1} = y_{i+1} e^{\mathcal{L}(t_i+\Delta t)}$, multiplying the previous relationship for $e^{\mathcal{L}(t_i+\Delta t)}$ we finally get:

$$\boxed{x_{i+1} = x_i e^{\mathcal{L}\Delta t} + \frac{\Delta t}{6}\left(e^{\mathcal{L}\Delta t} F\left(b_1^*\right) + 2e^{\mathcal{L}\Delta t/2} F\left(b_2^*\right) + 2e^{\mathcal{L}\Delta t/2} F\left(b_3^*\right) + F\left(b_4^*\right)\right).} \tag{A.15}$$

## A.3 The penalization method

The pseudo-spectral method with Fourier basis is very simple to implement it and very efficient. For this reason, it is natural to ask whether it can also be applied in non-periodic domains, or with obstacles. This can be obtained using the penalization method, proposed originally in 1984 [201]: the idea is to define a function $\mathcal{M}(\boldsymbol{x})$, which is equal to zero

inside the "true" domain, and equal to 1 into the walls/obstacles (in all the solid volume, not only in the boundary surface). In the Navier-Stokes equation a term $-(1/\tau)\mathcal{M}\boldsymbol{u}$ is therefore added: this correspond to a Brinkman model for porous media [219] with a strong permeability difference between the fluid and the solid domain. The validity of this method has been mathematically investigated in [220, 221], where it was demonstrated that the penalized incompressible Navier-Stokes equation converges towards the Navier-Stokes equation with no-slip boundary conditions inside the fluid domain (*i.e* vanishing velocity on the surface of the wall), and towards the Darcy law in the solid domain (velocity proportional to the pressure gradient). This method has been then applied to the study of turbulence in two and three dimensions. [202, 203, 222].

# Appendix B

# Brownian motion

Brownian motion is a typical phenomenon which occurs in microhydrodynamics. It is due to the fact that, if we consider a mesoscale object (*i. e.* micrometric size), although it is correct to describe the surrounding medium as a continuum fluid, it will be subjected to an incessant "bombing" by the molecules composing the fluid, due to their thermal agitation. This fact is obviously true also for macroscopic objects, but in that case the difference in scale between the molecules of the fluid and the macroscopic object is so large that single collisions are completely irrelevant for the larger object (although it is still affected by their cumulative sum, which corresponds to the thermal bath). Instead, if the object is not large enough, it will perform an irregular and incessant motion, even if the system is at thermodynamic equilibrium.

The phenomenon is named after the botanist Robert Brown, who observed it in 1827 studying at microscope particles of pollen suspended in water, and then also in inorganic matter, in order to clarify if it was due to active swimming. [223] The first physical interpretation was provided by Einstein during his *Annus mirabilis*, [224] and it was later extended by Sutherland, [225] Smoluchowski [226] and Langevin, [227] who formulated an alternative (but equivalent) description. [228] These works were a milestone in the history of physics, since they provided one of the first examples of fluctuation-dissipation relationships, an experimental demonstration of atoms existence and an archetype of stochastic process. Here

we are interested on its physical side, since it has a great importance in the rheology of suspensions.

## B.1 Langevin formulation

The Langevin description of the Brownian motion is focused on the single particle motion. In absence of external driving or other effects, the Newton's second law for a spherical particle with mass $m$ suspended in a fluid is (assuming, for simplicity, only one spatial dimension):

$$m\frac{d^2x}{dt^2} = -\zeta\frac{dx}{dt} + f(t), \tag{B.1}$$

where $\zeta$ is the friction coefficient (equal to $6\pi\mu r$ for a spherical no-slip particle, where $r$ is the radius), describing the hydrodynamic drag on the particle, and $f(t)$ is the forcing due to the impacts of the solvent molecules with the sphere. Pretending to know every single impact is impossible and useless, the idea is therefore to modelling $f(t)$ as a stochastic noise, taking in account the unpredictability of molecular motion. The simplest choice is a Gaussian white noise (where $v = \dot{x}$ is the velocity):

$$\langle f(t)\rangle = 0, \qquad \langle f(t)f(t')\rangle = \Gamma\delta(t-t'), \qquad \langle f(t)x(t')\rangle = 0, \qquad \langle f(t)v(t')\rangle = 0. \tag{B.2}$$

The noise strength $\Gamma$ can be obtained imposing the thermal equilibrium, and therefore the energy equipartition theorem. If we rewrite the equation (B.1) in terms of velocity $v$, we have as formal solution: [228]

$$v(t) = v(0)e^{(-\zeta/m)t} + \frac{1}{m}\int_0^t dt' e^{-(\zeta/m)(t-t')}f(t'). \tag{B.3}$$

Taking the square of $v$ and averaging, the cross term is proportional to $\langle v(0)f(t')\rangle$ and therefore equal to 0, while the second order integral can be solved as:

$$\frac{1}{m^2}\int_0^t dt' e^{-(\zeta/m)(t-t')}\int_0^t dt'' e^{-(\zeta/m)(t-t'')}\langle f(t')f(t'')\rangle = \tag{B.4}$$

$$\frac{1}{m^2}\int_0^t dt' e^{-(\zeta/m)(t-t')}\int_0^t dt'' e^{-(\zeta/m)(t-t'')}\Gamma\delta\left(t'-t''\right) = \frac{\Gamma}{2\zeta m}\left(1-e^{-2(\zeta/m)t}\right). \tag{B.5}$$

Hence the mean-squared velocity is:

$$\langle v^2(t)\rangle = \langle v^2(0)\rangle e^{-2(\zeta/m)t} + \frac{\Gamma}{2\zeta m}\left(1 - e^{-2(\zeta/m)t}\right), \tag{B.6}$$

and, since in the limit $t \to \infty$ we expect the equipartition theorem, being at equilibrium, we have:

$$\langle v^2\rangle = \frac{k_B T}{m} \qquad \Longrightarrow \qquad \Gamma = 2\zeta k_B T. \tag{B.7}$$

This fundamental relationship tells us that the thermal fluctuations must be balanced by viscous dissipation in order to be at equilibrium.

Going back to equation (B.1) for the position $x$, since $\langle f(t)\rangle = 0$ we have a null mean displacement: $\langle x(t)\rangle = 0$. Instead, if we consider the mean-squared displacement $\langle x^2(t)\rangle$ the situation is different. Multiplying eq. (B.1) by $x$ we can re-express it as:

$$\frac{m}{2}\frac{d^2x^2}{dt^2} - mv^2 = -\frac{\zeta}{2}\frac{dx^2}{dt} + xf(t). \tag{B.8}$$

Taking the average, and using the equipartition theorem, we have:

$$\frac{m}{2}\frac{d}{dt}\frac{d\langle x^2\rangle}{dt} + \frac{\zeta}{2}\frac{d\langle x^2\rangle}{dt} = k_B T, \tag{B.9}$$

thus, integrating:

$$\frac{d\langle x^2\rangle}{dt} = \frac{2k_B T}{\zeta}\left(1 - e^{-(\zeta/m)t}\right), \tag{B.10}$$

$$\langle x^2(t)\rangle = \frac{2k_B T}{\zeta}\left(t - \frac{m}{\zeta} + \frac{m}{\zeta}e^{-(\zeta/m)t}\right). \tag{B.11}$$

The solution tells us that we have two different regimes, separated by the time scale $\zeta/m$. For $t \to 0$, expanding the exponential as $e^{-t} \simeq 1 - t + t^2/2$, we have the **ballistic** regime:

$$\langle x^2(t)\rangle = \frac{k_B T}{m}t^2, \tag{B.12}$$

while for $t \to \infty$ we have the **diffusive** regime:

$$\langle x^2(t)\rangle = \frac{2k_B T}{m}t \equiv 2Dt, \tag{B.13}$$

where we have defined the diffusion constant $D$, whose importance will be more evident in the Smoluchowski formulation. The factor 2 is related to the dimensionality of the system, it is replaced by a factor 6 in three dimensions.

## B.2 Smoluchowski formulation

The Smoluchowski approach studies the system defining a probability density function $\Psi(x,t)$ for the Brownian particles. In the diffusive regime, $\Psi$ is therefore described by a diffusion equation (in order to describe also the ballistic regime at small times, a further second-order time derivative is needed):

$$\frac{\partial \Psi}{\partial t} = D\frac{\partial^2 \Psi}{\partial x^2} \tag{B.14}$$

At equilibrium the diffusion constant $D$ is the same defined in the Langevin formulation. This is due to the fact that, for non-interacting particles (diluted), the distribution is equivalent, a part from the normalization, to the concentration field. Since at thermodynamic equilibrium we expect a Boltzmann distribution

$$\Psi_{eq} \propto e^{\frac{V}{k_B T}}, \tag{B.15}$$

where $V$ is the a thermodynamic potential representing the osmotic pressure, and since at equilibrium the flux due to the osmotic force must be balanced by a diffusion flux:

$$-D\frac{\partial \Psi}{\partial x} = \frac{1}{\zeta}\Psi\frac{\partial V}{\partial x}, \tag{B.16}$$

we must have $D = k_B T/\zeta$. This is the fundamental Einstein relationship, which connects the mass transport of the particles and the momentum transport of the fluid (since the friction coefficient $\zeta$ depends on the viscosity $\mu$).

The equation (B.14) can be generalized to the case where a generic potential is present $U$ is present:

$$\frac{\partial \Psi}{\partial t} = \frac{\partial}{\partial x}\frac{1}{\zeta}\left(k_B T\frac{\partial \Psi}{\partial x} + \frac{\partial U}{\partial x}\right), \tag{B.17}$$

which lead us to define a free energy density for the system:

$$\mathcal{A}[\Psi] = \int d\{x\}\Psi\left(k_B T \ln \Psi + U\right). \tag{B.18}$$

It can demonstrated that the time derivative of $\mathcal{A}$ is always negative, unless $\Psi = \Psi_{eq}$, when it is equal to zero.

Another generalization it is in case of interacting particles. If $L_{mn}$ is the interaction matrix between the $n$-th and the $m$-th particle, and $x_n$ and $x_m$ are their corresponding positions, we have:

$$\frac{\partial \Psi}{\partial t} = \sum_{m,n} \frac{\partial}{\partial x_n} L_{mn} \left( k_B T \frac{\partial \Psi}{\partial x_m} + \frac{\partial U}{\partial x_m} \right), \tag{B.19}$$

where the friction coefficient $\zeta$ is included in $L_{mn}$. In this way we can also take in account the hydrodynamic interactions between the particles, *i.e.* the fact the motion of a particle modifies the fluid velocity field affecting the other ones. In this case, neglecting finite size effects, $L_{mn}$ is the Oseen tensor $\boldsymbol{H}(\boldsymbol{r}_n - \boldsymbol{r}_m)$. The generic equation for the probability density function is usually denoted also as Fokker-Planck equation.

## B.3 Rotational Brownian motion

Until now we considered only translational Brownian motion, the only one present in the case of spherical particles. In the case particles are anisotropic, thermal fluctuations of the fluid induce also a rotational Brownian motion. If, for example, we consider an ellipsoid with $\boldsymbol{n}$ as orientation axis, this versor can fluctuate on the surface of the sphere defined as $\|\boldsymbol{n}\| = 1$. The mathematical treatment of rotational Brownian motion is analogous to the translational one, with a Langevin and a Smoluchowski formulation. It is important to observe that the rotational diffusivity constant ($\text{time}^{-1}$) is dimensionally different from the translational diffusivity constant ($\text{length}^2/\text{time}$). [24]

# Bibliography


[1] L.D. Landau and E.M. Lifshitz. *Fluid Mechanics: Volume 6*. Number v. 6. Elsevier Science, 2013.

[2] K. Huang. *Statistical Mechanics*. Wiley, 1987.

[3] Sangtae Kim and Seppo J. Karrila. *Microhydrodynamics: Principles and Selected Applications*.

[4] Jens Elgeti, Roland G Winkler, and Gerhard Gompper. Physics of microswimmers—single particle motion and collective behavior: a review. *Reports on progress in physics*, 78(5):056601, 2015.

[5] David Saintillan. Rheology of active fluids. *Annual Review of Fluid Mechanics*, 50:563–592, 2018.

[6] Greg A Voth and Alfredo Soldati. Anisotropic particles in turbulence. *Annu. Rev. Fluid Mech*, 49(1):249–276, 2017.

[7] GG Stokes. On the effect of internal friction of fluids on the motion of pendulums. *Transactions of the Cambridge Philosophical Society.*, 9(8):106, 1850.

[8] George Keith Batchelor. *An introduction to fluid dynamics*. Cambridge university press, 2000.

[9] George Barker Jeffery. The motion of ellipsoidal particles immersed in a viscous fluid. *Proceedings of the Royal Society of London. Series A, Containing papers of a mathematical and physical character*, 102(715):161–179, 1922.

[10] Eric Lauga and Thomas R Powers. The hydrodynamics of swimming microorganisms. *Reports on progress in physics*, 72(9):096601, 2009.

[11] Edward M Purcell. Life at low reynolds number. *American journal of physics*, 45(1):3–11, 1977.

[12] Tian Qiu, Tung-Chun Lee, Andrew G Mark, Konstantin I Morozov, Raphael Münster, Otto Mierka, Stefan Turek, Alexander M Leshansky, and Peer Fischer. Swimming by reciprocal motion at low reynolds number. *Nature communications*, 5(1):1–8, 2014.

[13] Knut Drescher, Jörn Dunkel, Luis H Cisneros, Sujoy Ganguly, and Raymond E Goldstein. Fluid dynamics and noise in bacterial cell–cell and cell–surface scattering. *Proceedings of the National Academy of Sciences*, 108(27):10940–10945, 2011.

[14] Knut Drescher, Raymond E Goldstein, Nicolas Michel, Marco Polin, and Idan Tuval. Direct measurement of the flow field around swimming microorganisms. *Physical Review Letters*, 105(16):168101, 2010.

[15] Amarin G McDonnell, Tilvawala C Gopesh, Jennifer Lo, Moira O'Bryan, Leslie Y Yeo, James R Friend, and Ranganathan Prabhakar. Motility induced changes in viscosity of suspensions of swimming microbes in extensional flows. *Soft Matter*, 11(23):4658–4668, 2015.

[16] Andrey Sokolov and Igor S Aranson. Reduction of viscosity in suspension of swimming bacteria. *Physical review letters*, 103(14):148101, 2009.

[17] Salima Rafaï, Levan Jibuti, and Philippe Peyla. Effective viscosity of microswimmer suspensions. *Physical Review Letters*, 104(9):098102, 2010.

[18] Igor Aranson. Bacterial active matter. *Reports on Progress in Physics*, 2022.

[19] Randy H Ewoldt and Chaimongkol Saengow. Designing complex fluids. *Annual Review of Fluid Mechanics*, 54:413–441, 2022.

[20] Robert Byron Bird, Robert Calvin Armstrong, and Ole Hassager. Dynamics of polymeric liquids. vol. 1: Fluid mechanics. 1987.

[21] Itamar Procaccia, Victor S L'vov, and Roberto Benzi. Colloquium: Theory of drag reduction by polymers in wall-bounded turbulence. *Reviews of Modern Physics*, 80(1):225, 2008.

[22] Roberto Benzi and Emily SC Ching. Polymers in fluid flows. *Annual Review of Condensed Matter Physics*, 9:163–181, 2018.

[23] Robert Byron Bird, Charles F Curtiss, Robert C Armstrong, and Ole Hassager. *Dynamics of polymeric liquids, volume 2: Kinetic theory*. Wiley, 1987.

[24] Masao Doi and Samuel Frederick Edwards. *The theory of polymer dynamics*, volume 73. oxford university press, 1988.

[25] Christopher M White and M Godfrey Mungal. Mechanics and prediction of turbulent drag reduction with polymer additives. *Annu. Rev. Fluid Mech.*, 40:235–256, 2008.

[26] Victor Steinberg. Elastic turbulence: an experimental view on inertialess random flow. *Annual Review of Fluid Mechanics*, 53:27–58, 2021.

[27] Katepalli R Sreenivasan and Christopher M White. The onset of drag reduction by dilute polymer additives, and the maximum drag reduction asymptote. *Journal of Fluid Mechanics*, 409:149–164, 2000.

[28] Be A Toms. Some observations on the flow of linear polymer solutions through straight tubes at large reynolds numbers. *Proc. First Int. Conger. on Rheology*, 2:135–141, 1949.

[29] Farid Souas and Ahmed Salah Eddine Meddour. Drag reduction in single-phase crude oil flow: A mini-review. *Journal of Pipeline Science and Engineering*, page 100088, 2022.

[30] Lucas Warwaruk and Sina Ghaemi. Near-wall lubricating layer in drag-reduced flows of rigid polymers. *Physical Review Fluids*, 7(6):064605, 2022.

[31] John L Lumley. Drag reduction in turbulent flow by polymer additives. *Journal of Polymer Science: Macromolecular Reviews*, 7(1):263–290, 1973.

[32] Pierre-Gilles de Gennes. *Introduction to polymer dynamics*. CUP Archive, 1990.

[33] Lucas Warwaruk and Sina Ghaemi. A direct comparison of turbulence in drag-reduced flows of polymers and surfactants. *Journal of Fluid Mechanics*, 917, 2021.

[34] Preetinder S Virk. Drag reduction fundamentals. *AIChE Journal*, 21(4):625–656, 1975.

[35] Emily SC Ching, TS Lo, and Itamar Procaccia. Turbulent drag reduction by flexible and rodlike polymers: crossover effects at small concentrations. *Physical Review E*, 74(2):026301, 2006.

[36] Yacine Amarouchene, Daniel Bonn, Hamid Kellay, Ting-Shek Lo, Victor S L'vov, and Itamar Procaccia. Reynolds number dependence of drag reduction by rodlike polymers. *Physics of Fluids*, 20(6):065108, 2008.

[37] Victor S L'vov, Anna Pomyalov, Itamar Procaccia, and Vasil Tiberkevich. Drag reduction by polymers in wall bounded turbulence. *Physical review letters*, 92(24):244503, 2004.

[38] Roberto Benzi, Emily SC Ching, Nizan Horesh, and Itamar Procaccia. Theory of concentration dependence in drag reduction by polymers and of the maximum drag reduction asymptote. *Physical review letters*, 92(7):078302, 2004.

[39] Roberto Benzi, Emily SC Ching, TS Lo, Victor S L'vov, and Itamar Procaccia. Additive equivalence in turbulent drag reduction

by flexible and rodlike polymers. *Physical Review E*, 72(1):016305, 2005.

[40] R Benzi, E De Angelis, VS L'vov, Itamar Procaccia, and V Tiberkevich. Maximum drag reduction asymptotes and the cross-over to the newtonian plug. *Journal of Fluid Mechanics*, 551:185–195, 2006.

[41] Roberto Benzi, Emily SC Ching, Elisabetta De Angelis, and Itamar Procaccia. Comparison of theory and direct numerical simulations of drag reduction by rodlike polymers in turbulent channel flows. *Physical Review E*, 77(4):046309, 2008.

[42] JJJ Gillissen, BJ Boersma, PH Mortensen, and HI Andersson. Fibre-induced drag reduction. *Journal of Fluid Mechanics*, 602:209–218, 2008.

[43] Anselmo S Pereira, Rafhael M Andrade, and Edson J Soares. Drag reduction induced by flexible and rigid molecules in a turbulent flow into a rotating cylindrical double gap device: Comparison between poly (ethylene oxide), polyacrylamide, and xanthan gum. *Journal of Non-Newtonian Fluid Mechanics*, 202:72–87, 2013.

[44] Sadek Shaban, Madhar Azad, Japan Trivedi, and Sina Ghaemi. Investigation of near-wall turbulence in relation to polymer rheology. *Physics of Fluids*, 30(12):125111, 2018.

[45] Dilafruz Kulmatova, Ferhat Hadri, Sylvain Guillou, and Daniel Bonn. Turbulent viscosity profile of drag reducing rod-like polymers. *The European Physical Journal E*, 41(12):1–6, 2018.

[46] Guido Boffetta, Antonio Celani, and Andrea Mazzino. Drag reduction in the turbulent kolmogorov flow. *Physical Review E*, 71(3):036307, 2005.

[47] E De Angelis, CM Casciola, R Benzi, and R Piva. Homogeneous isotropic turbulence in dilute polymers. *Journal of Fluid Mechanics*, 531:1–10, 2005.

[48] S Berti, A Bistagnino, Guido Boffetta, A Celani, and S Musacchio. Small-scale statistics of viscoelastic turbulence. *EPL (Europhysics Letters)*, 76(1):63, 2006.

[49] PC Valente, CB Da Silva, and FT Pinho. The effect of viscoelasticity on the turbulent kinetic energy cascade. *Journal of fluid mechanics*, 760:39–62, 2014.

[50] Guido Boffetta, A Mazzino, S Musacchio, and L Vozella. Polymer heat transport enhancement in thermal convection: The case of rayleigh-taylor turbulence. *Physical Review Letters*, 104(18):184501, 2010.

[51] Roberto Benzi, Emily SC Ching, and Elisabetta De Angelis. Effect of polymer additives on heat transport in turbulent thermal convection. *Physical review letters*, 104(2):024502, 2010.

[52] Jeffrey A Byars, Alparslan Öztekin, Robert A Brown, and Gareth H Mckinley. Spiral instabilities in the flow of highly elastic fluids between rotating parallel disks. *Journal of Fluid Mechanics*, 271:173–218, 1994.

[53] Brandon M Baumert and Susan J Muller. Flow visualization of the elastic taylor-couette instability in boger fluids. *Rheologica Acta*, 34(2):147–159, 1995.

[54] Yong Lak Joo and Eric SG Shaqfeh. Observations of purely elastic instabilities in the taylor–dean flow of a boger fluid. *Journal of Fluid Mechanics*, 262:27–73, 1994.

[55] Alexander Groisman and Victor Steinberg. Elastic turbulence in a polymer solution flow. *Nature*, 405(6782):53–55, 2000.

[56] Alexander Groisman and Victor Steinberg. Efficient mixing at low reynolds numbers using polymer additives. *Nature*, 410(6831):905–908, 2001.

[57] Alexander Groisman and Victor Steinberg. Elastic turbulence in curvilinear flows of polymer solutions. *New Journal of Physics*, 6(1):29, 2004.

[58] S Berti, A Bistagnino, Guido Boffetta, A Celani, and S Musacchio. Two-dimensional elastic turbulence. *Physical Review E*, 77(5):055306, 2008.

[59] Anupam Gupta and Rahul Pandit. Melting of a nonequilibrium vortex crystal in a fluid film with polymers: Elastic versus fluid turbulence. *Physical Review E*, 95(3):033119, 2017.

[60] Muzio Grilli, Adolfo Vázquez-Quesada, and Marco Ellero. Transition to turbulence and mixing in a viscoelastic fluid flowing inside a channel with a periodic array of cylindrical obstacles. *Physical review letters*, 110(17):174501, 2013.

[61] Nansheng Liu and Bamin Khomami. Elastically induced turbulence in taylor–couette flow: direct numerical simulation and mechanistic insight. *Journal of Fluid Mechanics*, 737, 2013.

[62] R Van Buel, C Schaaf, and Holger Stark. Elastic turbulence in two-dimensional taylor-couette flows. *EPL (Europhysics Letters)*, 124(1):14001, 2018.

[63] Samriddhi Sankar Ray and Dario Vincenzi. Elastic turbulence in a shell model of polymer solution. *EPL (Europhysics Letters)*, 114(4):44001, 2016.

[64] A Fouxon and V Lebedev. Spectra of turbulence in dilute polymer solutions. *Physics of Fluids*, 15(7):2060–2072, 2003.

[65] E Balkovsky, A Fouxon, and V Lebedev. Turbulence of polymer solutions. *Physical Review E*, 64(5):056301, 2001.

[66] S Berti and Guido Boffetta. Elastic waves and transition to elastic turbulence in a two-dimensional viscoelastic kolmogorov flow. *Physical Review E*, 82(3):036314, 2010.

[67] Atul Varshney and Victor Steinberg. Elastic alfven waves in elastic turbulence. *Nature communications*, 10(1):1–7, 2019.

[68] Devranjan Samanta, Yves Dubief, Markus Holzner, Christof Schäfer, Alexander N Morozov, Christian Wagner, and Björn Hof. Elasto-inertial turbulence. *Proceedings of the National Academy of Sciences*, 110(26):10557–10562, 2013.

[69] Yves Dubief, Vincent E Terrapon, and Björn Hof. Elasto-inertial turbulence. *Annual Review of Fluid Mechanics*, 55:2023, 2022.

[70] Emmanuel LC Vi M Plan, Stefano Musacchio, and Dario Vincenzi. Emergence of chaos in a viscous solution of rods. *Physical Review E*, 96(5):053108, 2017.

[71] Stefano Musacchio, Massimo Cencini, Emmanuel LC Plan, and Dario Vincenzi. Enhancement of mixing by rodlike polymers. *The European Physical Journal E*, 41(7):1–5, 2018.

[72] Howard Brenner. Rheology of a dilute suspension of axisymmetric brownian particles. *International journal of multiphase flow*, 1(2):195–341, 1974.

[73] EJ Hinch and LG Leal. Constitutive equations in suspension mechanics. part 1. general formulation. *Journal of Fluid Mechanics*, 71(3):481–495, 1975.

[74] EJ Hinch and LG Leal. Constitutive equations in suspension mechanics. part 2. approximate forms for a suspension of rigid particles affected by brownian rotations. *Journal of Fluid Mechanics*, 76(1):187–208, 1976.

[75] John G Kirkwood. The statistical mechanical theory of irreversible processes in solutions of flexible macromolecules. visco-elastic behavior. *Recueil des Travaux Chimiques des Pays-Bas*, 68(7):649–660, 1949.

[76] Suresh G Advani and Charles L Tucker III. The use of tensors to describe and predict fiber orientation in short fiber composites. *Journal of rheology*, 31(8):751–784, 1987.

[77] Du Hwan Chung and Tai Hun Kwon. Invariant-based optimal fitting closure approximation for the numerical prediction of flow-induced fiber orientation. *Journal of rheology*, 46(1):169–194, 2002.

[78] JJJ Gillissen, BJ Boersma, PH Mortensen, and HI Andersson. On the performance of the moment approximation for the numerical computation of fiber stress in turbulent channel flow. *Physics of Fluids*, 19(3):035102, 2007.

[79] Stephen Montgomery-Smith, Wei He, David A Jack, and Douglas E Smith. Exact tensor closures for the three-dimensional jeffery's equation. *Journal of Fluid Mechanics*, 680:321–335, 2011.

[80] Albert Einstein. *Eine neue bestimmung der moleküldimensionen*. PhD thesis, ETH Zurich, 1905.

[81] Hanswalter Giesekus. Elasto-viskose flüssigkeiten, für die in stationären schichtströmungen sämtliche normalspannungskomponenten verschieden groß sind. *Rheologica Acta*, 2(1):50–62, 1962.

[82] Emmanouil D Fylladitakis. Kolmogorov flow: Seven decades of history. *Journal of Applied Mathematics and Physics*, 6(11):2227, 2018.

[83] Vladimir Igorevich Arnol'd and Lev Dmitrievich Meshalkin. An kolmogorov's seminar on selected problems of analysis (1958/1959). *Uspekhi Matematicheskikh Nauk*, 15(1):247–250, 1960.

[84] AM Obukhov. Kolmogorov flow and laboratory simulation of it. *Russ. Math. Surv*, 38(4):113–126, 1983.

[85] NF Bondarenko, EZ Gak, and MZ Gak. Application of mhd effects in electrolytes for modeling vortex processes in natural phenomena and in solving engineering-physical problems. *Journal of engineering physics and thermophysics*, 75(5):1234–1247, 2002.

[86] Stefano Musacchio and Guido Boffetta. Turbulent channel without boundaries: The periodic kolmogorov flow. *Physical Review E*, 89(2):023004, 2014.

[87] B Legras, B Villone, and U Frisch. Dispersive stabilization of the inverse cascade for the kolmogorov flow. *Physical review letters*, 82(22):4440, 1999.

[88] AJ Manfroi and WR Young. Slow evolution of zonal jets on the beta plane. *Journal of the atmospheric sciences*, 56(5):784–800, 1999.

[89] LD Meshalkin and Ia G Sinai. Investigation of the stability of a stationary solution of a system of equations for the plane movement of an incompressible viscous liquid. *Journal of Applied Mathematics and Mechanics*, 25(6):1700–1705, 1961.

[90] JSA Green. Two-dimensional turbulence near the viscous limit. *Journal of Fluid Mechanics*, 62(2):273–287, 1974.

[91] Gregory I Sivashinsky. Weak turbulence in periodic flows. *Physica D: Nonlinear Phenomena*, 17(2):243–255, 1985.

[92] Zhen Su She. Metastability and vortex pairing in the kolmogorov flow. *Physics Letters A*, 124(3):161–164, 1987.

[93] Vadim Borue and Steven A Orszag. Numerical study of three-dimensional kolmogorov flow at high reynolds numbers. *Journal of Fluid Mechanics*, 306:293–323, 1996.

[94] Svetlana Vladimirovna Fortova. Numerical simulation of the three-dimensional kolmogorov flow in a shear layer. *Computational Mathematics and Mathematical Physics*, 53(3):311–319, 2013.

[95] Neil J Balmforth and Yuan-Nan Young. Stratified kolmogorov flow. *Journal of Fluid Mechanics*, 450:131–167, 2002.

[96] André Thess. Instabilities in two-dimensional spatially periodic flows. part i: Kolmogorov flow. *Physics of Fluids A: Fluid Dynamics*, 4(7):1385–1395, 1992.

[97] P Beyer and S Benkadda. Advection of passive particles in the kolmogorov flow. *Chaos: An Interdisciplinary Journal of Nonlinear Science*, 11(4):774–779, 2001.

[98] Francesco Santamaria, Filippo De Lillo, Massimo Cencini, and Guido Boffetta. Gyrotactic trapping in laminar and turbulent kolmogorov flow. *Physics of Fluids*, 26(11):111901, 2014.

[99] M. Borgnino, G. Boffetta, M. Cencini, F. De Lillo, and K. Gustavsson. Alignment of elongated swimmers in a laminar and turbulent kolmogorov flow. *Phys. Rev. Fluids*, 7:074603, Jul 2022.

[100] Guido Boffetta, Antonio Celani, Andrea Mazzino, Alberto Puliafito, and Massimo Vergassola. The viscoelastic kolmogorov flow: eddy viscosity and linear stability. *Journal of Fluid Mechanics*, 523:161–170, 2005.

[101] A Bistagnino, Guido Boffetta, A Celani, A Mazzino, A Puliafito, and M Vergassola. Nonlinear dynamics of the viscoelastic kolmogorov flow. *Journal of Fluid Mechanics*, 590:61–80, 2007.

[102] A Sozza, M Cencini, S Musacchio, and G Boffetta. Drag enhancement in a dusty kolmogorov flow. *Physical Review Fluids*, 5(9):094302, 2020.

[103] Alessandro Sozza, Massimo Cencini, Stefano Musacchio, and Guido Boffetta. Instability of a dusty kolmogorov flow. *Journal of Fluid Mechanics*, 931, 2022.

[104] Herbert Brian Squire. On the stability for three-dimensional disturbances of viscous fluid flow between parallel walls. *Proceedings of the Royal Society of London. Series A, Containing Papers of a Mathematical and Physical Character*, 142(847):621–628, 1933.

[105] Uriel Frisch. *Turbulence: the legacy of AN Kolmogorov*. Cambridge university press, 1995.

[106] Kraichnan RH. Inertial ranges in two-dimensional turbulence. *Phys. Fluids*, 10:1417, 1967.

[107] Guido Boffetta and Robert E Ecke. Two-dimensional turbulence. *Annual review of fluid mechanics*, 44(1):427–451, 2012.

[108] G Boffetta, M Borgnino, and S Musacchio. Scaling of rayleigh-taylor mixing in porous media. *Physical Review Fluids*, 5(6):062501, 2020.

[109] M Borgnino, G Boffetta, and S Musacchio. Dimensional transition in darcy-rayleigh-taylor mixing. *Physical Review Fluids*, 6(7):074501, 2021.

[110] JJJ Gillissen, BJ Boersma, PH Mortensen, and HI Andersson. The stress generated by non-brownian fibers in turbulent channel flow simulations. *Physics of Fluids*, 19(11):115107, 2007.

[111] John P Boyd. *Chebyshev and Fourier spectral methods*. Courier Corporation, 2001.

[112] William H Press, Saul A Teukolsky, William T Vetterling, and Brian P Flannery. *Numerical recipes 3rd edition: The art of scientific computing*. Cambridge university press, 2007.

[113] R Sureshkumar and AN Beris. Effect of artificial stress diffusivity on the stability of numerical calculations and the flow dynamics of time-dependent viscoelastic flows. *J. Non-Newtonian Fluid Mech.*, 60(1):53–80, 1995.

[114] C. M. Bender and S. A. Orszag. *Advanced Mathematical Methods for Scientists and Engineers*. McGraw-Hill, 1978.

[115] George Papanicolau, Alain Bensoussan, and J-L Lions. *Asymptotic analysis for periodic structures*. Elsevier, 1978.

[116] Roberto Benzi, Elisabetta De Angelis, Rama Govindarajan, and Itamar Procaccia. Shell model for drag reduction with polymer additives in homogeneous turbulence. *Physical Review E*, 68(1):016308, 2003.

[117] Rodrigo S Mitishita, Gwynn J Elfring, and Ian A Frigaard. Statistics and spectral analysis of turbulent duct flows with flexible and

rigid polymer solutions. *Journal of Non-Newtonian Fluid Mechanics*, page 104952, 2022.

[118] Mark J Bowick, Nikta Fakhri, M Cristina Marchetti, and Sriram Ramaswamy. Symmetry, thermodynamics, and topology in active matter. *Physical Review X*, 12(1):010501, 2022.

[119] Gerhard Gompper, Roland G Winkler, Thomas Speck, Alexandre Solon, Cesare Nardini, Fernando Peruani, Hartmut Löwen, Ramin Golestanian, U Benjamin Kaupp, Luis Alvarez, et al. The 2020 motile active matter roadmap. *Journal of Physics: Condensed Matter*, 32(19):193001, 2020.

[120] Dirk Helbing, Illés Farkas, and Tamas Vicsek. Simulating dynamical features of escape panic. *Nature*, 407(6803):487–490, 2000.

[121] Andrea Cavagna, Alessio Cimarelli, Irene Giardina, Giorgio Parisi, Raffaele Santagati, Fabio Stefanini, and Massimiliano Viale. Scale-free correlations in starling flocks. *Proceedings of the National Academy of Sciences*, 107(26):11865–11870, 2010.

[122] Kolbjørn Tunstrøm, Yael Katz, Christos C Ioannou, Cristián Huepe, Matthew J Lutz, and Iain D Couzin. Collective states, multistability and transitional behavior in schooling fish. *PLoS computational biology*, 9(2):e1002915, 2013.

[123] Henricus H Wensink, Jörn Dunkel, Sebastian Heidenreich, Knut Drescher, Raymond E Goldstein, Hartmut Löwen, and Julia M Yeomans. Meso-scale turbulence in living fluids. *Proceedings of the national academy of sciences*, 109(36):14308–14313, 2012.

[124] Thuan Beng Saw, Amin Doostmohammadi, Vincent Nier, Leyla Kocgozlu, Sumesh Thampi, Yusuke Toyama, Philippe Marcq, Chwee Teck Lim, Julia M Yeomans, and Benoit Ladoux. Topological defects in epithelia govern cell death and extrusion. *Nature*, 544(7649):212–216, 2017.

[125] Amin Doostmohammadi, Jordi Ignés-Mullol, Julia M Yeomans, and Francesc Sagués. Active nematics. *Nature communications*, 9(1):1–13, 2018.

[126] Antoine Bricard, Jean-Baptiste Caussin, Nicolas Desreumaux, Olivier Dauchot, and Denis Bartolo. Emergence of macroscopic directed motion in populations of motile colloids. *Nature*, 503(7474):95–98, 2013.

[127] Benno Liebchen and Hartmut Löwen. Synthetic chemotaxis and collective behavior in active matter. *Accounts of chemical research*, 51(12):2982–2990, 2018.

[128] Nitin Kumar, Harsh Soni, Sriram Ramaswamy, and AK Sood. Flocking at a distance in active granular matter. *Nature communications*, 5(1):1–9, 2014.

[129] Luca Giomi. Geometry and topology of turbulence in active nematics. *Physical Review X*, 5(3):031003, 2015.

[130] Suraj Shankar, Anton Souslov, Mark J Bowick, M Cristina Marchetti, and Vincenzo Vitelli. Topological active matter. *Nature Reviews Physics*, 4(6):380–398, 2022.

[131] Maxime Theillard, Roberto Alonso-Matilla, and David Saintillan. Geometric control of active collective motion. *Soft Matter*, 13(2):363–375, 2017.

[132] Scott Weady, David B Stein, and Michael J Shelley. Thermodynamically consistent coarse-graining of polar active fluids. *Physical Review Fluids*, 7(6):063301, 2022.

[133] John Toner and Yuhai Tu. Long-range order in a two-dimensional dynamical xy model: how birds fly together. *Physical review letters*, 75(23):4326, 1995.

[134] Michele Ballerini, Nicola Cabibbo, Raphael Candelier, Andrea Cavagna, Evaristo Cisbani, Irene Giardina, Vivien Lecomte, Alberto

Orlandi, Giorgio Parisi, Andrea Procaccini, et al. Interaction ruling animal collective behavior depends on topological rather than metric distance: Evidence from a field study. *Proceedings of the national academy of sciences*, 105(4):1232–1237, 2008.

[135] Tim Sanchez, Daniel TN Chen, Stephen J DeCamp, Michael Heymann, and Zvonimir Dogic. Spontaneous motion in hierarchically assembled active matter. *Nature*, 491(7424):431–434, 2012.

[136] D Dell'Arciprete, ML Blow, AT Brown, FDC Farrell, Juho S Lintuvuori, AF McVey, D Marenduzzo, and Wilson CK Poon. A growing bacterial colony in two dimensions as an active nematic. *Nature communications*, 9(1):1–9, 2018.

[137] Ricard Alert, Jaume Casademunt, and Jean-François Joanny. Active turbulence. *Annual Review of Condensed Matter Physics*, 13, 2021.

[138] John Toner, Yuhai Tu, and Sriram Ramaswamy. Hydrodynamics and phases of flocks. *Annals of Physics*, 318(1):170–244, 2005.

[139] Jonasz Słomka and Jörn Dunkel. Generalized navier-stokes equations for active suspensions. *The European Physical Journal Special Topics*, 224(7):1349–1358, 2015.

[140] Karsten Kruse, Jean-Francois Joanny, Frank Jülicher, Jacques Prost, and Ken Sekimoto. Generic theory of active polar gels: a paradigm for cytoskeletal dynamics. *The European Physical Journal E*, 16(1):5–16, 2005.

[141] Tamás Vicsek, András Czirók, Eshel Ben-Jacob, Inon Cohen, and Ofer Shochet. Novel type of phase transition in a system of self-driven particles. *Physical review letters*, 75(6):1226, 1995.

[142] N David Mermin and Herbert Wagner. Absence of ferromagnetism or antiferromagnetism in one-or two-dimensional isotropic heisenberg models. *Physical Review Letters*, 17(22):1133, 1966.

[143] Pierre C Hohenberg. Existence of long-range order in one and two dimensions. *Physical Review*, 158(2):383, 1967.

[144] John Toner and Yuhai Tu. Flocks, herds, and schools: A quantitative theory of flocking. *Physical review E*, 58(4):4828, 1998.

[145] L.D. Landau and E.M. Lifshitz. *Statistical Physics: Volume 5*, volume 5. Elsevier, 2013.

[146] John Toner. Reanalysis of the hydrodynamic theory of fluid, polar-ordered flocks. *Physical Review E*, 86(3):031918, 2012.

[147] John Toner. Birth, death, and flight: A theory of malthusian flocks. *Physical review letters*, 108(8):088102, 2012.

[148] Leiming Chen, Chiu Fan Lee, John Toner, et al. Moving, reproducing, and dying beyond flatland: Malthusian flocks in dimensions d $> 2$. *Physical Review Letters*, 125(9):098003, 2020.

[149] Leiming Chen, Chiu Fan Lee, and John Toner. Universality class for a nonequilibrium state of matter: A d= 4- $\varepsilon$ expansion study of malthusian flocks. *Physical Review E*, 102(2):022610, 2020.

[150] Leiming Chen, John Toner, and Chiu Fan Lee. Critical phenomenon of the order–disorder transition in incompressible active fluids. *New Journal of Physics*, 17(4):042002, 2015.

[151] Leiming Chen, Chiu Fan Lee, and John Toner. Mapping two-dimensional polar active fluids to two-dimensional soap and one-dimensional sandblasting. *Nature communications*, 7(1):1–10, 2016.

[152] Leiming Chen, Chiu Fan Lee, and John Toner. Incompressible polar active fluids in the moving phase in dimensions d $> 2$. *New Journal of Physics*, 20(11):113035, 2018.

[153] Navdeep Rana and Prasad Perlekar. Coarsening in the two-dimensional incompressible toner-tu equation: Signatures of turbulence. *Physical Review E*, 102(3):032617, 2020.

[154] Navdeep Rana and Prasad Perlekar. Phase ordering, topological defects, and turbulence in the three-dimensional incompressible toner-tu equation. *Physical Review E*, 105(3):L032603, 2022.

[155] John D Gibbon, Kolluru Venkata Kiran, Nadia Bihari Padhan, and Rahul Pandit. An analytical and computational study of the incompressible toner-tu equations. *Physica D: Nonlinear Phenomena*, page 133594, 2022.

[156] John Toner, Nicholas Guttenberg, and Yuhai Tu. Hydrodynamic theory of flocking in the presence of quenched disorder. *Physical Review E*, 98(6):062604, 2018.

[157] John Toner, Nicholas Guttenberg, and Yuhai Tu. Swarming in the dirt: Ordered flocks with quenched disorder. *Physical review letters*, 121(24):248002, 2018.

[158] Leiming Chen, Chiu Fan Lee, Ananyo Maitra, and John Toner. Hydrodynamic theory of two-dimensional incompressible polar active fluids with quenched and annealed disorder. *Phys. Rev. E*, 106:044608, Oct 2022.

[159] Leiming Chen, Chiu Fan Lee, Ananyo Maitra, and John Toner. Packed swarms on dirt: Two-dimensional incompressible flocks with quenched and annealed disorder. *Phys. Rev. Lett.*, 129:188004, Oct 2022.

[160] Leiming Chen, Chiu Fan Lee, Ananyo Maitra, and John Toner. Incompressible polar active fluids with quenched random field disorder in dimensions d $> 2$. *Phys. Rev. Lett.*, 129:198001, Oct 2022.

[161] Suraj Shankar, Mark J Bowick, and M Cristina Marchetti. Topological sound and flocking on curved surfaces. *Physical Review X*, 7(3):031039, 2017.

[162] Andrea Cavagna, Lorenzo Del Castello, Irene Giardina, Tomas Grigera, Asja Jelic, Stefania Melillo, Thierry Mora, Leonardo Parisi,

Edmondo Silvestri, Massimiliano Viale, et al. Flocking and turning: a new model for self-organized collective motion. *Journal of Statistical Physics*, 158(3):601–627, 2015.

[163] Christopher Dombrowski, Luis Cisneros, Sunita Chatkaew, Raymond E Goldstein, and John O Kessler. Self-concentration and large-scale coherence in bacterial dynamics. *Physical review letters*, 93(9):098103, 2004.

[164] Hugo Wioland, Francis G Woodhouse, Jörn Dunkel, John O Kessler, and Raymond E Goldstein. Confinement stabilizes a bacterial suspension into a spiral vortex. *Physical review letters*, 110(26):268102, 2013.

[165] Héctor Matías López, Jérémie Gachelin, Carine Douarche, Harold Auradou, and Eric Clément. Turning bacteria suspensions into superfluids. *Physical review letters*, 115(2):028301, 2015.

[166] Ju Swift and Pierre C Hohenberg. Hydrodynamic fluctuations at the convective instability. *Physical Review A*, 15(1):319, 1977.

[167] Sebastian Heidenreich, Jörn Dunkel, Sabine HL Klapp, and Markus Bär. Hydrodynamic length-scale selection in microswimmer suspensions. *Physical Review E*, 94(2):020601, 2016.

[168] Henning Reinken, Sabine HL Klapp, Markus Bär, and Sebastian Heidenreich. Derivation of a hydrodynamic theory for mesoscale dynamics in microswimmer suspensions. *Physical Review E*, 97(2):022613, 2018.

[169] Martin James, Wouter JT Bos, and Michael Wilczek. Turbulence and turbulent pattern formation in a minimal model for active fluids. *Physical Review Fluids*, 3(6):061101, 2018.

[170] Henning Reinken, Daiki Nishiguchi, Sebastian Heidenreich, Andrey Sokolov, Markus Bär, Sabine HL Klapp, and Igor S Aranson. Organizing bacterial vortex lattices by periodic obstacle arrays. *Communications Physics*, 3(1):1–9, 2020.

[171] Henning Reinken, Sebastian Heidenreich, Markus Bär, and Sabine HL Klapp. Ising-like critical behavior of vortex lattices in an active fluid. *Physical Review Letters*, 128(4):048004, 2022.

[172] Vasil Bratanov, Frank Jenko, and Erwin Frey. New class of turbulence in active fluids. *Proceedings of the National Academy of Sciences*, 112(49):15048–15053, 2015.

[173] Martin James and Michael Wilczek. Vortex dynamics and lagrangian statistics in a model for active turbulence. *The European Physical Journal E*, 41(2):1–6, 2018.

[174] Siddhartha Mukherjee, Rahul K Singh, Martin James, and Samriddhi Sankar Ray. Anomalous diffusion and lévy walks distinguish active from inertial turbulence. *Physical Review Letters*, 127(11):118001, 2021.

[175] Vasco M Worlitzer, Gil Ariel, Avraham Be'er, Holger Stark, Markus Bär, and Sebastian Heidenreich. Motility-induced clustering and meso-scale turbulence in active polar fluids. *New Journal of Physics*, 23(3):033012, 2021.

[176] Vasco M Worlitzer, Gil Ariel, Avraham Be'er, Holger Stark, Markus Bär, and Sebastian Heidenreich. Turbulence-induced clustering in compressible active fluids. *Soft Matter*, 17(46):10447–10457, 2021.

[177] Jörn Dunkel, Sebastian Heidenreich, Markus Bär, and Raymond E Goldstein. Minimal continuum theories of structure formation in dense active fluids. *New Journal of Physics*, 15(4):045016, 2013.

[178] Florian Zanger, Hartmut Löwen, and Jürgen Saal. Analysis of a living fluid continuum model. In *Mathematics for Nonlinear Phenomena: Analysis and Computation: International Conference in Honor of Professor Yoshikazu Giga on his 60th Birthday*, pages 285–303. Springer, 2015.

[179] Christiane Bui, Hartmut Löwen, and Jürgen Saal. Turbulence in active fluids caused by self-propulsion. *Asymptotic Analysis*, 113(4):195–209, 2019.

[180] Christiane Bui, Christian Gesse, and Jürgen Saal. Stable and unstable flow regimes for active fluids in the periodic setting. *Nonlinear Analysis: Real World Applications*, 69:103707, 2023.

[181] Aparna Baskaran and M Cristina Marchetti. Hydrodynamics of self-propelled hard rods. *Physical Review E*, 77(1):011920, 2008.

[182] TJ Pedley. Collective behaviour of swimming micro-organisms. *Experimental mechanics*, 50(9):1293–1301, 2010.

[183] Jörn Dunkel, Sebastian Heidenreich, Knut Drescher, Henricus H Wensink, Markus Bär, and Raymond E Goldstein. Fluid dynamics of bacterial turbulence. *Physical review letters*, 110(22):228102, 2013.

[184] GK Batchelor and JT Green. The determination of the bulk stress in a suspension of spherical particles to order c2. *Journal of Fluid Mechanics*, 56(3):401–427, 1972.

[185] Pierre-Gilles De Gennes and Jacques Prost. *The physics of liquid crystals*. Number 83. Oxford university press, 1993.

[186] George L Hand. A theory of anisotropic fluids. *Journal of Fluid Mechanics*, 13(1):33–46, 1962.

[187] Henning Reinken, Sebastian Heidenreich, Markus Bär, and Sabine HL Klapp. Anisotropic mesoscale turbulence and pattern formation in microswimmer suspensions induced by orienting external fields. *New Journal of Physics*, 21(1):013037, 2019.

[188] Gil Ariel, Marina Sidortsov, Shawn D Ryan, Sebastian Heidenreich, Markus Bär, and Avraham Be'Er. Collective dynamics of two-dimensional swimming bacteria: Experiments and models. *Physical Review E*, 98(3):032415, 2018.

[189] Etienne Emmrich and Lukas Geuter. Analysis of a model for the dynamics of microswimmer suspensions. *Mathematical Methods in the Applied Sciences*, 44(18):14041–14058, 2021.

[190] Sanjay C. P. and Ashwin Joy. Friction scaling laws for transport in active turbulence. *Physical Review Fluids*, 5(2):024302, 2020.

[191] Javier Urzay, Amin Doostmohammadi, and Julia M Yeomans. Multi-scale statistics of turbulence motorized by active matter. *Journal of Fluid Mechanics*, 822:762–773, 2017.

[192] Livio Nicola Carenza, Luca Biferale, and Giuseppe Gonnella. Cascade or not cascade? energy transfer and elastic effects in active nematics. *Europhysics Letters*, 132(4):44003, 2020.

[193] Livio Nicola Carenza, Luca Biferale, and Giuseppe Gonnella. Multiscale control of active emulsion dynamics. *Physical Review Fluids*, 5(1):011302, 2020.

[194] Ricard Alert, Jean-François Joanny, and Jaume Casademunt. Universal scaling of active nematic turbulence. *Nature Physics*, 16(6):682–688, 2020.

[195] Rahul K Singh, Siddhartha Mukherjee, and Samriddhi Sankar Ray. Lagrangian manifestation of anomalies in active turbulence. *Physical Review Fluids*, 7(3):033101, 2022.

[196] Kolluru Venkata Kiran, Anupam Gupta, Akhilesh Kumar Verma, and Rahul Pandit. Irreversiblity in bacterial turbulence: Insights from the mean-bacterial-velocity model. *arXiv preprint arXiv:2201.12722*, 2022.

[197] Henning Reinken, Sabine HL Klapp, and Michael Wilczek. Optimal turbulent transport in microswimmer suspensions. *Physical Review Fluids*, 7(8):084501, 2022.

[198] Martin James, Dominik Anton Suchla, Jörn Dunkel, and Michael Wilczek. Emergence and melting of active vortex crystals. *Nature communications*, 12(1):1–11, 2021.

[199] Ingmar H Riedel, Karsten Kruse, and Jonathon Howard. A self-organized vortex array of hydrodynamically entrained sperm cells. *Science*, 309(5732):300–303, 2005.

[200] Siddhartha Mukherjee, Rahul K Singh, Martin James, and Samriddhi Sankar Ray. Intermittency, fluctuations and maximal chaos in an emergent universal state of active turbulence. *arXiv preprint arXiv:2207.12227*, 2022.

[201] E Arquis, JP Caltagirone, et al. Sur les conditions hydrodynamiques au voisinage d'une interface milieu fluide-milieu poreux: applicationa la convection naturelle. *CR Acad. Sci. Paris II*, 299:1–4, 1984.

[202] Kai Schneider and Marie Farge. Decaying two-dimensional turbulence in a circular container. *Physical review letters*, 95(24):244502, 2005.

[203] Kai Schneider, Mickaël Paget-Goy, Alberto Verga, and Marie Farge. Numerical simulation of flows past flat plates using volume penalization. *Computational and Applied Mathematics*, 33(2):481–495, 2014.

[204] Akira Okubo. Horizontal dispersion of floatable particles in the vicinity of velocity singularities such as convergences. In *Deep sea research and oceanographic abstracts*, volume 17, pages 445–454. Elsevier, 1970.

[205] John Weiss. The dynamics of enstrophy transfer in two-dimensional hydrodynamics. *Physica D: Nonlinear Phenomena*, 48(2-3):273–294, 1991.

[206] Andrea Cavagna, Irene Giardina, and Tomás S Grigera. The physics of flocking: Correlation as a compass from experiments to theory. *Physics Reports*, 728:1–62, 2018.

[207] Hugo Wioland, Enkeleida Lushi, and Raymond E Goldstein. Directed collective motion of bacteria under channel confinement. *New Journal of Physics*, 18(7):075002, 2016.

[208] Kun-Ta Wu, Jean Bernard Hishamunda, Daniel TN Chen, Stephen J DeCamp, Ya-Wen Chang, Alberto Fernández-Nieves, Seth Fraden, and Zvonimir Dogic. Transition from turbulent to coherent flows in confined three-dimensional active fluids. *Science*, 355(6331):eaal1979, 2017.

[209] Amin Doostmohammadi and Julia M Yeomans. Coherent motion of dense active matter. *The European Physical Journal Special Topics*, 227(17):2401–2411, 2019.

[210] Enkeleida Lushi, Hugo Wioland, and Raymond E Goldstein. Fluid flows created by swimming bacteria drive self-organization in confined suspensions. *Proceedings of the National Academy of Sciences*, 111(27):9733–9738, 2014.

[211] Kazusa Beppu, Ziane Izri, Jun Gohya, Kanta Eto, Masatoshi Ichikawa, and Yusuke T Maeda. Geometry-driven collective ordering of bacterial vortices. *Soft Matter*, 13(29):5038–5043, 2017.

[212] Song Liu, Suraj Shankar, M Cristina Marchetti, and Yilin Wu. Viscoelastic control of spatiotemporal order in bacterial active matter. *Nature*, 590(7844):80–84, 2021.

[213] Andrey Sokolov and Igor S Aranson. Physical properties of collective motion in suspensions of bacteria. *Physical review letters*, 109(24):248109, 2012.

[214] Norman A Phillips. The general circulation of the atmosphere: A numerical experiment. *Quarterly Journal of the Royal Meteorological Society*, 82(352):123–164, 1956.

[215] Norman A Phillips. An example of non-linear computational instability. *The atmosphere and the sea in motion*, 501:504, 1959.

[216] Steven A Orszag. On the elimination of aliasing in finite-difference schemes by filtering high-wavenumber components. *Journal of Atmospheric Sciences*, 28(6):1074–1074, 1971.

[217] Carl Runge. Über die numerische auflösung von differentialgleichungen. *Mathematische Annalen*, 46(2):167–178, 1895.

[218] Wilhelm Kutta. Beitrag zur naherungsweisen integration totaler differentialgleichungen. *Zeitschrift für Mathematik und Physik*, 46:435–453, 1901.

[219] Hendrik C Brinkman. A calculation of the viscous force exerted by a flowing fluid on a dense swarm of particles. *Flow, Turbulence and Combustion*, 1(1):27–34, 1949.

[220] Philippe Angot, Charles-Henri Bruneau, and Pierre Fabrie. A penalization method to take into account obstacles in incompressible viscous flows. *Numerische Mathematik*, 81(4):497–520, 1999.

[221] Gilles Carbou and Pierre Fabrie. Boundary layer for a penalization method for viscous incompressible flow. *Advances in Differential equations*, 8(12):1453–1480, 2003.

[222] Nicholas K-R Kevlahan and Jean-Michel Ghidaglia. Computation of turbulent flow past an array of cylinders using a spectral method with brinkman penalization. *European Journal of Mechanics-B/Fluids*, 20(3):333–350, 2001.

[223] Robert Brown. *The miscellaneous botanical works: containing I, geographico-botanical and II, structural and physiological memoirs*, volume 21. Hardwicke, 1866.

[224] Albert Einstein. Über die von der molekularkinetischen theorie der wärme geforderte bewegung von in ruhenden flüssigkeiten suspendierten teilchen. *Annalen der physik*, 4, 1905.

[225] William Sutherland. Lxxv. a dynamical theory of diffusion for non-electrolytes and the molecular mass of albumin. *The London, Edinburgh, and Dublin Philosophical Magazine and Journal of Science*, 9(54):781–785, 1905.

[226] Marian Von Smoluchowski. Zur kinetischen theorie der brownschen molekularbewegung und der suspensionen. *Annalen der physik*, 326(14):756–780, 1906.

[227] Paul Langevin. Sur la théorie du mouvement brownien. *Compt. Rendus*, 146:530–533, 1908.

[228] Xin Bian, Changho Kim, and George Em Karniadakis. 111 years of brownian motion. *Soft Matter*, 12(30):6331–6346, 2016.

# Ringraziamenti

Svolgere il dottorato durante una pandemia globale non è certo l'ideale, ma posso dirmi fortunato nell'aver completato questo percorso anche grazie alle persone che ne hanno preso parte.

In primo luogo è per me fondamentale ringraziare Stefano, che non si è solamente limitato a svolgere il normale ruolo del supervisor, ma ha sempre dimostrato di avere a cuore la buona riuscita del mio dottorato, sia da un punto di vista strettamente scientifico, che dal punto di vista umano nel suo complesso.

Un altro contributo di grande importanza è quello di Guido, non solo per il suo apporto scientifico diretto, ma anche per la fiducia che mi ha sempre dimostrato e, soprattutto, per aver sempre incoraggiato un'atmosfera familiare nel gruppo, che ha reso indimenticabile l'esperienza di questi anni.

Il prezioso supporto di Filippo è stato anch'esso cruciale nel gestire i capricci di Turbo (e la confusione del sottoscritto...), e portare avanti il lavoro.

Come già accennato, l'atmosfera in un ambiente di ricerca è fondamentale non solo per essere produttivi, ma specialmente per costruire un ricordo positivo dell'esperienza. Vorrei quindi ringraziare tutti quelli che in questi anni ne hanno fatto parte, sia prestando il loro aiuto, che quando richiesto non è mai stato negato, o anche solo per il tempo trascorso insieme: Alessandro, Davide, Elisa, Enrico, Francesco D. V., Francesco T., Francesco V., Marco, Marta, Matteo B., Matteo L., Miguel e Stefano B.